



---

**Forschungszentrum Karlsruhe**  
in der Helmholtz-Gemeinschaft

**Wissenschaftliche Berichte**  
FZKA 7269

**Modification of the  
Electronic Properties of  
Carbon Nanotubes by  
Bundling, Temperature,  
B- and N-doping:  
a Resonance Raman Study**

**T. Skipa**

Institut für Festkörperphysik

Dezember 2006



Forschungszentrum Karlsruhe

in der Helmholtz-Gemeinschaft

Wissenschaftliche Berichte

FZKA 7269

**Modification of the Electronic Properties of Carbon  
Nanotubes by Bundling, Temperature, B- and N-doping:  
a Resonance Raman Study**

Tetyana Skipa

Institut für Festkörperphysik

von der Fakultät für Physik der Universität Karlsruhe (TH)  
genehmigte Dissertation

Forschungszentrum Karlsruhe GmbH, Karlsruhe  
2006

Für diesen Bericht behalten wir uns alle Rechte vor

**Forschungszentrum Karlsruhe GmbH**  
Postfach 3640, 76021 Karlsruhe

Mitglied der Hermann von Helmholtz-Gemeinschaft  
Deutscher Forschungszentren (HGF)

ISSN 0947-8620

urn:nbn:de:0005-072694

MODIFICATION OF THE ELECTRONIC PROPERTIES OF CARBON  
NANOTUBES BY BUNDLING, TEMPERATURE, B- AND N-DOPING:  
A RESONANCE RAMAN STUDY

Zur Erlangung des akademischen Grades eines  
DOKTORS DER NATURWISSENSCHAFTEN  
von der Fakultät für Physik der Universität (TH)  
Karlsruhe

genehmigte  
DISSERTATION

von

Tetyana Skipa, Dipl.-Phys.  
aus Kiew (Ukraine)

Tag der mündlichen Prüfung: 09.06.2006

Referent: Prof. Dr. Hilbert von Löhneysen

Korreferent: Prof. Dr. Manfred Kappes



# Abstract

This work focuses on the study of the electronic properties of carbon nanotubes (CNTs) and their composites. Most attention is paid to influences related to the application of CNTs that can change their electronic properties, i.e. the tube-tube interaction (by bundling), temperature effects, and doping with Boron and Nitrogen. These effects were studied with Resonance Raman Scattering (RRS).

The tube-tube interaction was investigated by combining the methods of RRS and High Resolution Transmission Electron Microscopy. With this study it was possible to establish a functional dependence between the relative Raman intensities and the nanotube bundle sizes.

For the description of the tube-tube interaction a phenomenological model was developed that can be used for the characterization of samples with unknown tube distribution. This model allows also revealing the electronic energy changes induced by temperature.

A large part of this work was devoted to the synthesis of new nano-materials. BNC-nanotubes with various element compositions were synthesized and studied using Energy Dispersive X-ray Analysis giving the B and N content.

# Zusammenfassung

## Modifikation der elektronischen Eigenschaften von Kohlenstoff-Nanoröhren durch Bündelung, Temperatur und Dotierung mit Bor und Stickstoff:

### Eine Untersuchung mit resonanter Ramanstreuung

In dieser Arbeit werden die elektronischen Eigenschaften von Kohlenstoffnanoröhren (CNTs) und von den hieraus abgeleiteten Materialien untersucht. Von besonderem Interesse waren dabei anwendungsrelevante Einflüsse, die die elektronischen Zustände von Nanoröhren verändern, wie die Wechselwirkung von CNTs bei Bündelung, thermische Effekte sowie der Einfluss von Dotierung mit Bor und Stickstoff. Diese Effekte wurden mittels resonanter Ramanstreuung (RRS) untersucht.

Zur Untersuchung von Bündelungseffekten wurde die RRS mit der hochauflösenden Transmissionselektronenmikroskopie kombiniert. Mit Hilfe dieser Untersuchungen gelang es erstmals, einen funktionalen Zusammenhang zwischen Raman-Intensität und Bündelgröße zu finden.

Zur Beschreibung von Wechselwirkungseffekten zwischen CNTs in Bündeln wurde ein phänomenologisches Modell entwickelt, das zur Charakterisierung von Proben mit unbekanntem CNT-Bündelungen eingesetzt werden kann. Das Modell beschreibt auch die durch thermische Effekte hervorgerufenen Änderungen der elektronischen Übergangsenergien.

Ein weiterer Teil der Arbeit war der Herstellung dotierter Nanomaterialien gewidmet. Insbesondere wurden BNC-Nanoröhren mit verschiedener elementarer Zusammensetzung synthetisiert und untersucht. Die Zusammensetzung konnte mittels der Methode der energiedispersiven Röntgenspektroskopie bestimmt werden.

## List of publications related to this thesis

S. Lebedkin, F. Hennrich, T. Skipa, M. Kappes. Near-infrared photoluminescence of single-walled carbon nanotubes prepared by the laser vaporization method. *J. Phys. Chem. B* **107**, 1949 (2003).

T. Skipa, P. Schweiss, F. Hennrich, S. Lebedkin. Modification of the electronic properties of carbon nanotubes: bundling and B- and N- doping. *AIP Conf. Proceedings: Electronic Properties of Novel Nanostructures* **786**, 198 (2005).

T. Skipa, P. Schweiss, K.-P. Bohnen, S. Lebedkin, B. Renker. Raman spectra of  $B_xN_yC_z$  – nanotubes: Correlation between B, N – content and frequency shifts of the G-band. *AIP Conf. Proceedings: Electronic Properties of Synthetic Nanostructures* **723**, 289 (2004).

S. Lebedkin, F. Hennrich, T. Skipa, R. Krupke, M. Kappes. Near-Infrared photoluminescence of single-walled carbon nanotubes obtained by the pulsed laser vaporization method. *AIP Conf. Proceedings: Molecular Nanostructures* **685**, 148 (2003).



# Contents

<b>Chapter 1 Introduction.....</b>	<b>1</b>
<b>Chapter 2 Geometry and Structure .....</b>	<b>5</b>
<b>Chapter 3 Electronic Properties .....</b>	<b>9</b>
3.1 Zone-folding approximation and electronic structure of CNTs.....	9
3.2 Electronic density of states for carbon nanotubes.....	15
3.3 Models for carbon nanotube assignment .....	18
3.4 Boron-carbonitride nanotubes ( $B_xN_yC_z$ -NTs).....	22
3.5 Summary .....	24
<b>Chapter 4 Experimental Techniques .....</b>	<b>25</b>
4.1 Resonance Raman Scattering (RRS) .....	26
4.2 Resonance Raman scattering and electronic DOS.....	30
4.3 Raman spectra of carbon nanotubes .....	32
4.4 Experimental Raman set-up.....	39
4.5 Summary .....	40
<b>Chapter 5 Bundling Effects.....</b>	<b>41</b>
5.1 Motivation.....	41
5.2 Sample preparation .....	46
5.3 Experimental results.....	49
5.4 Data analysis .....	52
5.4.1 Raman intensities and electronic energy shift .....	53
5.4.2 Correlation between the Raman intensity, electronic energy shift and bundle size .....	57
5.5 Summary .....	62
<b>Chapter 6 Temperature Effects .....</b>	<b>65</b>
6.1 Motivation.....	65
6.2 Theoretical model for temperature behaviour of the band gap of semiconducting CNTs .....	67
6.3 Experimental results.....	71
6.3.1 Samples and experimental details .....	71
6.3.2 Temperature changes in Raman spectra of semiconducting nanotubes.....	71
6.3.3 Temperature changes in Raman spectra of metallic nanotubes .....	73
6.4 Summary .....	75
<b>Chapter 7 B- and N- Doping .....</b>	<b>77</b>
7.1 Motivation.....	77
7.2 Material preparation.....	79
7.3 Experimental results.....	81
7.3.1 Morphology of the $B_xN_yC_z$ nanostructures: HRTEM study .....	81

7.3.2 Element composition: EDX study .....	86
7.3.3 Non-resonant Raman spectroscopy on $B_xN_yC_z$ -NTs.....	86
7.3.4 Photoluminescent and NIR-vis-UV absorption spectroscopy on $B_xN_yC_z$ - NTs.....	90
7.4 Summary .....	93
<b>Chapter 8 Conclusions.....</b>	<b>95</b>
<b>Appendix A.....</b>	<b>99</b>
<b>A.1 Tight-binding model for graphite.....</b>	<b>99</b>
<b>A.2 Tight-binding approximation for carbon nanotubes.....</b>	<b>103</b>
<b>Bibliography .....</b>	<b>109</b>

# Chapter 1

## Introduction

The fascinating era of carbon nanomaterials science started in 1991 when carbon nanotubes (CNTs) were first reported by Iijima [1] in their multi-walled form. These newly discovered objects were expected to have unique physical properties caused by their one-dimensional structure.

With a shape of hollow cylinders made of one or more graphite sheets, carbon nanotubes are typically several  $\mu\text{m}$  in length and about 1 nm in diameter. Along the cylinder axis they can therefore be regarded as infinitely long ( $\approx 10^4$  atoms per 1  $\mu\text{m}$ ) whereas their circumference contains only very few atoms ( $\approx 20$ ). Such a unique one-dimensional nature makes the electronic properties of carbon nanotubes very specific.

Moreover, two carbon nanotubes with equal diameters can have completely different electronic properties: either metallic or semiconducting depending only on the individual geometric structure. In particular, taking into account all possible ways to roll up the graphite sheet into a closed cylinder, one finds that in general, 2/3 of all nanotube structures will be semiconducting and 1/3 will be metallic.

Shortly after the discovery, carbon nanotubes were found to exhibit remarkable physical properties such as the ability to conduct huge electrical current densities up to  $10^9$  A/cm<sup>2</sup> [2, 3], or their extraordinary mechanical strength. The elastic modulus of the nanotube rope is  $\approx 1$  TPa and its shear modulus is approximately 1 GPa [4, 5]. Strong band gap photoluminescence of individual semiconducting CNTs [6], electron transport properties [7] and field-emission characteristics [8] made them very promising objects from the application point of view. Some electronic devices based on single nanotubes such as field-effect transistors [9] have been recently developed. Due to the large aspect ratio the nanotubes can be used as tips for scanning electron microscopy and magnetic force microscopy [10, 11]. Some of the application ideas such as nanotube-based displays, X-ray sources, lamps, amplifiers, and electrochemical composites, have been already realized on an industrial scale.

A comprehensive study of these nano-objects is important not only because of their possible applications but also because many intriguing fundamental phenomena appear in low-dimensional physics, for instance one-dimensional singularities in the density of states [12, 13], Luttinger liquid behaviour [13], and the zero-dimensional effect of Coulomb blockade [14].

The application of carbon nanotubes defines its own distinct research challenges, e.g. in order to achieve the cheap production of high-quality material with given electronic properties in large amounts. A major difficulty in the nanotube synthesis up to now is the variety of nanotube structures obtained in one production batch.

In the last few years great success was achieved in the preparation and treatment of carbon nanotubes. A multitude of novel methods was discovered that allow handling and studying the nanotubes more precisely and conveniently. These are for example the method of separation of metallic tubes from the semiconducting ones by

electrophoresis [15], the controlled growth of tubes with desired properties [16], and the separation of the tubes from bundles inside organic micelles in solutions [6, 17].

The study of the effects which are important for application of nanotubes is the subject of this thesis. The application requirements, in particular, those of nanoelectronics, stimulated a strong interest to factors which can influence the electronic properties of carbon nanotubes. The present work, therefore, concentrates on studying several of those factors: the tube-tube interaction (bundling effects), temperature effects, and the effects of B- and N-doping.

Since the nanotubes produced by most of the preparation methods are always joined in large or small bundles, the *tube-tube interaction* is an important factor to study. In general the interaction with the environment is known to modify the electronic properties of carbon nanotubes. In particular, it decreases the band gap values of the semiconducting tubes [18]. However, the correlation between the nanotube bundle size and the electronic energy shifts had not been studied in detail up to now. The knowledge of such a functional relationship would help to estimate, for example, the change in the emission characteristics of a semiconducting nanotube bundle of a certain size compared to the emission of a single nanotube.

*Temperature* is another factor which plays an important role in the nanoelectronic: the nanotubes are expected to work in a wide temperature range. Despite the theoretically predicted effect of how temperature affects the electronic properties of semiconducting CNTs [19] it is not yet well established experimentally.

*Doping* CNTs with B and N atoms was theoretically predicted to modify the nanotube electronic band structure very specifically. Variation of the element composition of a carbon nanotube will result in “tuning” of its electronic properties [20 – 22]. In this way, materials with metallic, semiconducting or insulating characteristics can be produced.

Focusing on these important effects, the thesis is organized as follows: An introduction to the structure and geometry of carbon nanotubes and their electronic properties is given in *Chapter 2* and *Chapter 3*. Here, the tight-binding model and zone folding approximation are considered. *Chapter 4* presents the basics of the resonance Raman scattering in carbon nanotubes, and discusses its advantages for the nanotube characterization. The experimental results are presented in *Chapters 5, 6, and 7*.

*Chapter 5* is devoted to the resonance Raman study of the influence of the tube-tube interaction on the electronic band structure of both semiconducting and metallic CNTs. A phenomenological model is developed that allows describing the Raman intensities observed in terms of tube-tube interaction.

*Chapter 6* presents a study of the temperature effects in CNTs using the resonance Raman technique. For the analysis of the results the model of *Chapter 5* is modified and used. *Chapters 5* and *6* are thus interconnected by the phenomenological model which can be applied to the description of both the tube-tube interaction and the temperature effects.

*Chapter 7* is devoted to the synthesis and the characterization of new exotic nanomaterials. Here the experience in production of boron-carbo-nitride nanostructures such as  $B_xN_yC_z$ -NTs with different  $x$ ,  $y$ , and  $z$  element compositions, single and multi-walled BN-NTs, BN-nanorods, BN-nanococoons, and some others is summarized. Despite the common interest in all those structures and methods of their preparation,

most attention is paid to the influence of B- and N-doping on the electronic properties of CNTs, which have been used as templates in the synthesis. The electronic properties of  $B_xN_yC_z$ -NTs were investigated using Raman scattering and Near-Infrared-Visual-Ultraviolet absorption spectroscopy.

Finally, *Chapter 8* recollects the most important advances gained in the course of this work, and closes with some concluding remarks.



## Chapter 2

### Geometry and Structure

Carbon nanotubes can be described as planar sheets of graphite (graphene) rolled up into hollow cylinders with a large aspect ratio (i.e. the ratio length/diameter  $\approx 10^4 - 10^5$ ). Therefore carbon nanotubes can be considered as one-dimensional objects, usually having diameters of about 0.7 – 10 nm and length of several  $\mu\text{m}$ .

There are many possible ways to roll up a graphene “honeycomb” sheet into a cylinder with the hexagons to be completed. Fig. 2.1 shows such an example of tube construction.  $C_h$  is the chiral vector starting at a carbon atom and pointing to another atom in the lattice so, that the beginning of the vector coincides with its end. By rolling up the hexagonal sheet along the chiral vector one would obtain the tube with the circumference equal to the length of the chiral vector  $C_h$ .

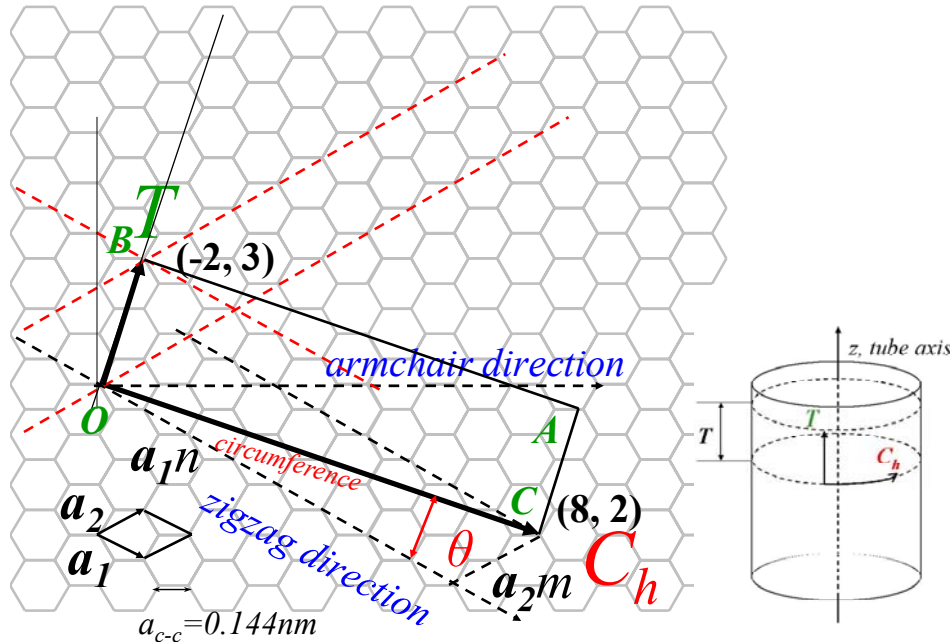


**Figure 2.1** The graphene “honeycomb” sheet and the schematically presented nanotube which can be obtained by rolling up the sheet along the direction of the chiral vector  $C_h$ ; the cylinder built on the chiral vector  $C_h$  (equal to the nanotube circumference) and the translation vector  $T$  represents the unit cell of a carbon nanotube.

With the sketch of Fig. 2.1 it is easy to specify the main geometric parameters of a carbon nanotube: the nanotube axis, i.e. the axis going through the centre of the nanotube cylinder parallel to its walls, and the chiral vector  $C_h$ , which can be expressed as the superposition of  $n$  vectors  $a_1$  and  $m$  vectors  $a_2$ :

$$C_h = na_1 + ma_2. \quad (2.1)$$

Vectors  $a_1$ , and  $a_2$  are called the basis vectors the graphene lattice ([12], [13] and [16]).

The pair of integers  $(n, m)$  gives thus the length of the chiral vector  $\mathbf{C}_h$  i.e. the circumference of the tube:

$$L = |\mathbf{C}_h| = \sqrt{\mathbf{C}_h \cdot \mathbf{C}_h} = a\sqrt{n^2 + nm + m^2}, \quad (2.2)$$

where  $a = 3^{1/2}a_{c-c} = 0.246$  nm is the length of the graphene basis vectors  $\mathbf{a}_1$  and  $\mathbf{a}_2$ , and  $a_{c-c}$  is the nearest-neighbor distance between two carbon atoms in the graphene lattice (see Fig. 2.1). The diameter  $d$  of a tube can be derived from the tube circumference as follows:

$$d = \frac{L}{\pi} = \frac{a\sqrt{n^2 + nm + m^2}}{\pi}. \quad (2.3)$$

The chiral angle  $\theta$  is defined as the angle between the vectors  $\mathbf{C}_h$  and  $\mathbf{a}_1$  (Fig. 2.1). The chiral angle denotes the tilt angle of the hexagons with respect to the direction of the nanotube axis. Due to the hexagonal symmetry of the graphite honeycomb lattice, the chiral angle is restricted to the range of  $0 \leq |\theta| \leq 30^\circ$ . It can also be defined by the  $(n, m)$  indices as follows:

$$\cos\theta = \frac{\mathbf{C}_h \cdot \mathbf{a}_1}{|\mathbf{C}_h| |\mathbf{a}_1|} = \frac{2n + m}{2\sqrt{n^2 + nm + m^2}}, \quad (2.4)$$

where  $\mathbf{a}_1 \cdot \mathbf{a}_1 = \mathbf{a}_2 \cdot \mathbf{a}_2 = a^2$ , and  $\mathbf{a}_1 \cdot \mathbf{a}_2 = a^2/2$ . (2.4')

All possible nanotube structures can be divided into three classes with respect to their chiral angles  $\theta$ : tubes with  $\theta=0^\circ$  (so-called zigzag tubes), with  $\theta= \pm 30^\circ$  (armchair tubes), and the rest of the tubes with all intermediate chiral angles  $0 < |\theta| < 30^\circ$  (chiral tubes). Figure 2.2 schematically shows the structure of the zigzag and the armchair tubes.

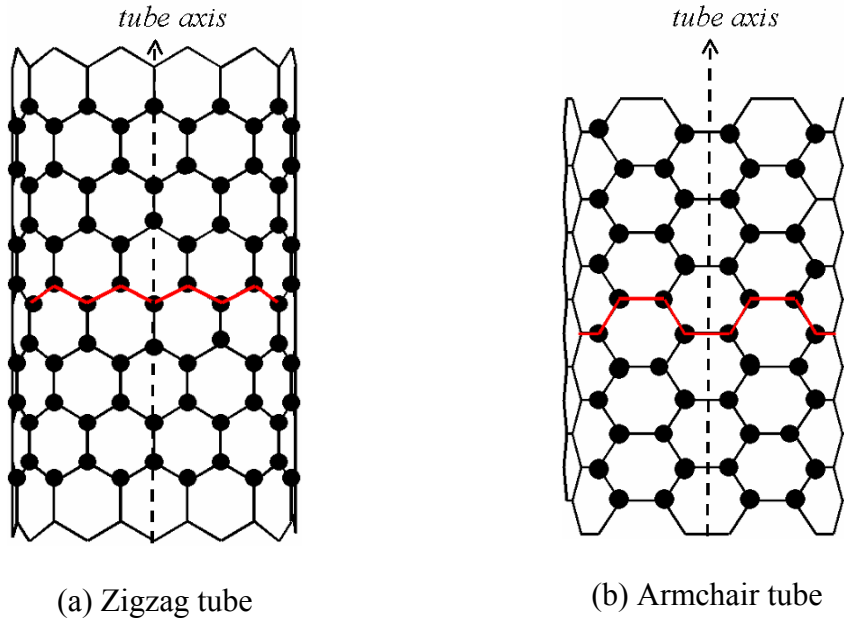


**Figure 2.2** Schematic structure of the zigzag (a) and the armchair (b) tubes.

Furthermore, it is important to specify the unit cell of a carbon nanotube. As far as the unit cell is a part of a nanotube containing *non-equivalent* atoms, it can be naturally defined as a cylinder built on two vectors  $\mathbf{C}_h$  and  $\mathbf{T}$  normal to each other, where  $\mathbf{T}$  is the translation vector parallel to the nanotube axis and corresponding to the first point of the graphite lattice through which the vector  $\mathbf{OB}$  (normal to  $\mathbf{C}_h$ ) passes (Fig. 2.1). The translation vector  $\mathbf{T}$  can be expressed in term of the basis vectors  $\mathbf{a}_1$  and  $\mathbf{a}_2$  as

$$\mathbf{T} = t_1\mathbf{a}_1 + t_2\mathbf{a}_2 \equiv (t_1, t_2) \quad (2.5)$$

Here  $(t_1, t_2)$  are integers which do not have a common divisor except for unity. Using  $\mathbf{C}_h \cdot \mathbf{T} = 0$  and (2.1, 2.4', and 2.5) one obtains the expressions for the components  $t_1$  and  $t_2$ :

$$t_1 = -\frac{2m+n}{d_R}, \quad \text{and} \quad t_2 = \frac{2n+m}{d_R}, \quad (2.6)$$

where  $d_R$  is the greatest common divisor of  $(2m+n)$  and  $(2n+m)$ . Or, introducing  $g$  as the greatest common divisor of  $n$  and  $m$ , one can express  $d_R$  [12] as follows:

$$d_R = \begin{cases} g, & \text{if } (n-m) \text{ is not a multiple of } 3g, \\ 3g, & \text{if } (n-m) \text{ is a multiple of } 3g^*. \end{cases} \quad (2.7)$$

The length of the translation vector is given by

$$T = |\mathbf{T}| = \sqrt{3}L/d_R, \quad (2.8)$$

where  $L$  is the circumference of the nanotube given by (2.2).

In Figure 2.1 the unit cell of the graphite is the rhombus specified by the vectors  $\mathbf{a}_1$  and  $\mathbf{a}_2$  and containing two carbon atoms. The nanotube unit cell is the rectangle OBAC defined by the vectors  $\mathbf{C}_h$  and  $\mathbf{T}$ . The number of hexagons per unit cell of a carbon nanotube can be obtained dividing the area of the nanotube unit cell by the area of the graphite unit cell (the area of the rhombus is equal to the area of the hexagon):

$$N = \frac{|\mathbf{C}_h \times \mathbf{T}|}{|\mathbf{a}_1 \times \mathbf{a}_2|} = \frac{2(n^2 + nm + m^2)}{d_R} = \frac{2L^2}{a^2 d_R}. \quad (2.9)$$

It should be noted that each hexagon contains two carbon atoms, therefore the unit cell of the carbon nanotube contains  $2N$  carbon atoms. Geometric parameters of the zigzag, armchair and chiral tubes are summarized in the Table 2.1.

\*Euclid's law about greatest common divisor properties

**Table 2.1** Geometric parameters of carbon nanotubes.

Tube	Diameter $d$ , nm	Chiral angle, $\theta$	Number of atoms/unit cell, $2N$	Translation period, $T$
zigzag ( $n, 0$ )	$an/\pi$	$0^\circ$	$\frac{4n^2}{d_R} = 4n$	$\sqrt{3}a$
armchair ( $n, n$ )	$\sqrt{3}an/\pi$	$30^\circ$	$\frac{12n^2}{d_R} = 4n$	$a$
chiral ( $n, m$ )	$\frac{\sqrt{n^2 + nm + m^2}a}{\pi}$	$\arccos \frac{2n + m}{2\sqrt{n^2 + nm + m^2}}$	$\frac{4(n^2 + nm + m^2)}{d_R}$	$\frac{a\sqrt{3(n^2 + nm + m^2)}}{d_R}$

# Chapter 3

## Electronic Properties

### 3.1 Zone-folding approximation and electronic structure of CNTs

The detailed calculations of the electronic properties of graphene developed within the tight-binding model are given in the Appendix. The following section considers what happens to the electronic properties of a graphene sheet rolled up along a certain direction creating a carbon nanotube. The main parameters of a carbon nanotube were determined in *Chapter 2*. These are the pair of indices  $(n, m)$ , the chiral vector  $C_h$ , the chiral angle  $\theta$ , the tube diameter  $d$ , the translation period  $T$ , and the unit cell; the wavevectors  $k_1$  and  $k_2$  and the first Brillouin zone of the graphene are also specified in the Appendix.

Figure 3.1 shows the two-dimensional electronic energy dispersion of graphene calculated within the tight-binding model in the first Brillouin zone (see the Appendix for details). The wavevectors  $k_1$  and  $k_2$  of graphene take values  $(-2\pi q/l\sqrt{3}; 2\pi q/l\sqrt{3}]$ , where  $l = qa$  is the size of the crystalline lattice,  $a$  is the lattice constant, and  $q$  is the number of unit cells in the whole crystal (Born-v. Karman boundary conditions) [12, 13].

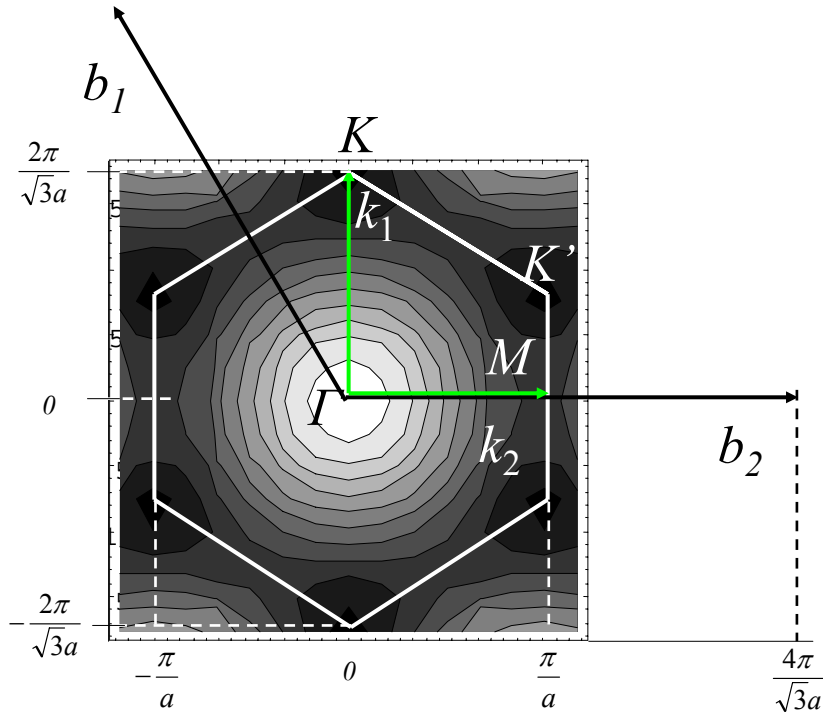


**Figure 3.1** The two-dimensional electronic energy dispersion of graphene (presented as contour plot) calculated within the tight-binding model in the first Brillouin zone (BZ) of graphite (white hexagon); the graphite wavevectors  $k_1$  and  $k_2$  in the first BZ, the reciprocal vectors  $b_1$  and  $b_2$ , and the points of high symmetry  $\Gamma$ ,  $K$ ,  $K'$  and  $M$  are also shown.

If the size of a crystal  $l$  is large, the difference between the values of two neighbouring wavevectors  $2\pi/l$  becomes small, and the wavevectors  $\mathbf{k}_1$  and  $\mathbf{k}_2$  can be considered as taking continuous values. The unit cell of a carbon nanotube gives rise to the wavevectors  $\mathbf{k}_z$  and  $\mathbf{k}_\perp$  defined by the conditions:

$$\begin{aligned} \mathbf{C}_h \cdot \mathbf{k}_z &= 0, & \mathbf{T} \cdot \mathbf{k}_z &= 2\pi, \\ \mathbf{C}_h \cdot \mathbf{k}_\perp &= 2\pi, & \mathbf{T} \cdot \mathbf{k}_\perp &= 0, \end{aligned} \quad (3.1)$$

where  $\mathbf{k}_z$  is parallel to the tube axis  $z$ , and  $\mathbf{k}_\perp$  is directed along the tube circumference. In carbon nanotubes the wavevector  $\mathbf{k}_z$  along the tube axis is continuous since the tube is considered as infinitely long. The absolute value of the wavevector  $\mathbf{k}_z$  is given by:

$$|\mathbf{k}_z| = \frac{2\pi}{|\mathbf{T}|} = \frac{2\pi}{T}, \quad (3.2)$$

where  $T$  is the translation period.

In Fig. 3.2 the unit cell of a carbon nanotube defined by the cylinder built on the chiral vector  $\mathbf{C}_h$  and the translation vector  $\mathbf{T}$  is presented.

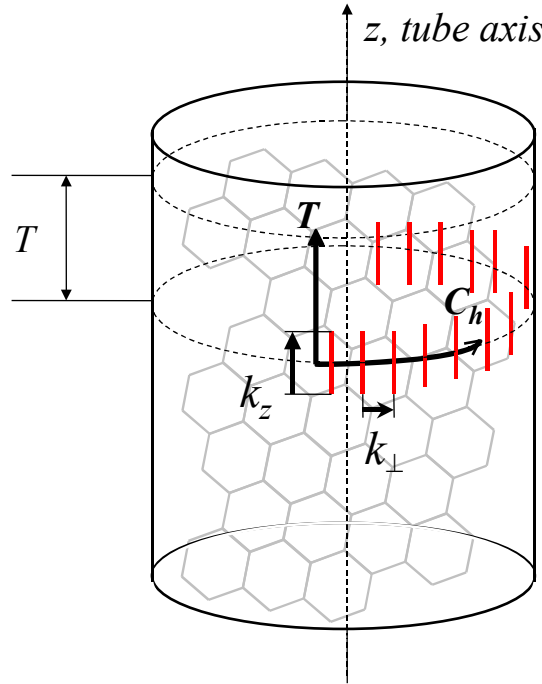


**Figure 3.2** Carbon nanotube unit cell defined by the cylinder built on the chiral vector  $\mathbf{C}_h$  and the translation vector  $\mathbf{T}$ . The wavevector  $\mathbf{k}_z$  along the tube axis  $z$  takes continuous values, the wavevector  $\mathbf{k}_\perp$  along the tube circumference takes discrete values.

The first Brillouin zone of a carbon nanotube extends within the interval  $(-\pi/T; \pi/T]$  in the  $z$  - direction. The wavevector  $\mathbf{k}_z$ , therefore, takes continuous values in this interval. At the same time, the wavevector along the circumference is quantized, according to the boundary condition:

$$|C_h| = m\lambda = \pi d \quad \Leftrightarrow \quad k_{\perp, \mu} = \frac{2\pi}{\lambda} = \frac{2\pi}{|C_h|} \mu = \frac{2}{d} \mu. \quad (3.3)$$

Here  $\lambda$  is the wave length,  $m = N$  is an integer, and  $\mu$  takes values:  $-N/2 + 1, \dots, 0, N/2$ , where  $N$  is the number of hexagons in the unit cell.

The reason for the discreteness of the wavevector along the circumference is the following: since the electron (or phonon) states are described with plane waves, the circumference of a tube must contain an integer number of those wavelengths (all other wavelengths will vanish due to interference). There must be exactly  $N$  wavevectors whose number is equal to the number of hexagons (not the number of atoms!).

Analysing the confinement of the quasi-continuous graphene wavevectors  $\mathbf{k}_1$  and  $\mathbf{k}_2$  inside the nanotube unit cell (the rolled up piece of the graphene sheet with the size  $C_h \times T$ ), one should use the number of the hexagonal graphite unit cell (with the size  $\mathbf{a}_1 \times \mathbf{a}_2$  equal to the area of a hexagon), as far as this number determines the

discreteness of the graphite wavevectors. The value  $N = \frac{|C_h \times T|}{|\mathbf{a}_1 \times \mathbf{a}_2|}$  (see eq. 2.9) is

equal to the number of hexagons in the unit cell of a carbon nanotube, and characterizes the discreteness of the nanotube wavevector along the nanotube circumference. This results in  $N$  discrete values of the wavevector  $\mathbf{k}_\perp$  in the direction of the circumference. The nanotube wavevectors  $\mathbf{k}_\perp$  and  $\mathbf{k}_z$  can be derived from the graphene reciprocal vectors  $\mathbf{b}_1$  and  $\mathbf{b}_2$  combining eqs. (2.1), (2.6), (3.1), and also (A8) from the Appendix:

$$\mathbf{k}_\perp = \frac{2n+m}{Nd_R} \mathbf{b}_1 + \frac{2m+n}{Nd_R} \mathbf{b}_2, \quad (3.4)$$

$$\mathbf{k}_z = -\frac{m}{N} \mathbf{b}_1 + \frac{n}{N} \mathbf{b}_2. \quad (3.4')$$

The construction of the first Brillouin zone of a zigzag (13, 0) tube is shown in Fig. 3.3 as an example. The energy dispersion of graphite in the first Brillouin zone (white hexagon) is shown as contour plot; letters  $\Gamma$ ,  $M$ , and  $K$  ( $K'$ ) denote the high symmetry points in the first hexagonal Brillouin zone of the graphite.

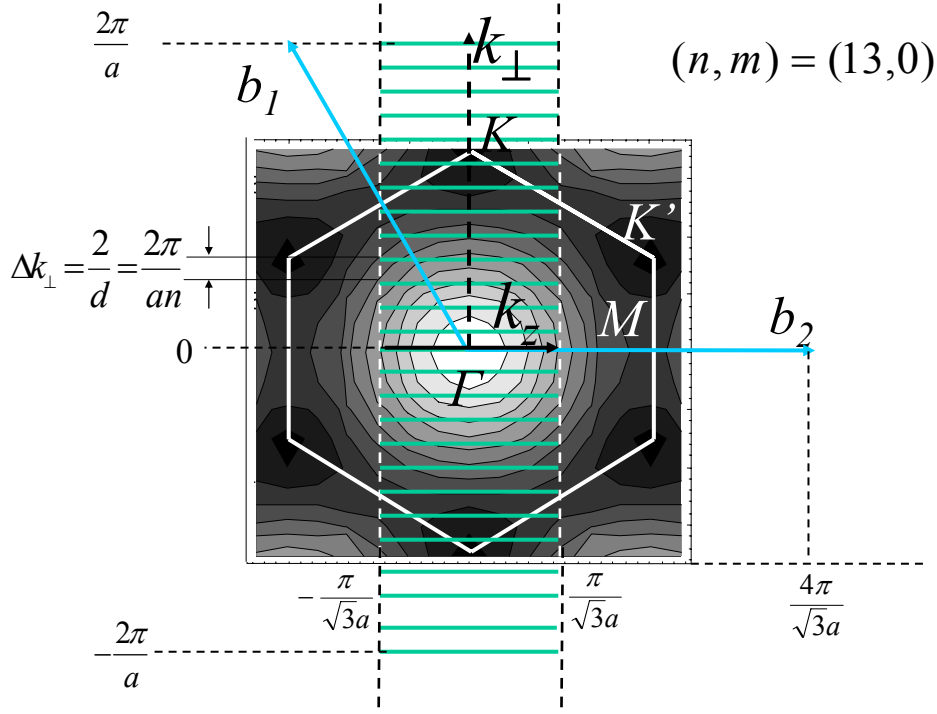


**Figure 3.3** The first Brillouin zone of the zigzag (13, 0) nanotube consists of  $N = 2n = 26$  parallel lines (inside the reciprocal unit cell of the graphite  $\mathbf{b}_1 \times \mathbf{b}_2$ ) separated by  $\Delta \mathbf{k}_\perp = 2\pi/an$ ; the values  $\mathbf{k}_z$  vary in the range  $(-\pi/\sqrt{3}a; \pi/\sqrt{3}a]$ .

The wavevectors  $\mathbf{k}_\perp$  and  $\mathbf{k}_z$  in the first Brillouin zone of a tube (13, 0) vary in the range:

$\mathbf{k}_\perp = (-2\mu/d; 2\mu/d]$  and  $\mathbf{k}_z = (-\pi/\sqrt{3}a; \pi/\sqrt{3}a]$ , where,  $\mu$  takes values  $-N/2 + 1, \dots, 0, N/2$ , and  $N$  is the number of hexagons in the nanotube unit cell. The vector  $\mathbf{k}_\perp$  is discrete with the step  $\Delta k_\perp = 2/d$ . Therefore, the first Brillouin zone of (13, 0) nanotube consists of  $N = 26$  lines parallel to the  $z$ -axis, separated by  $\Delta k_\perp = 2/d$ , and having the length of  $|\mathbf{k}_z| = 2\pi/\sqrt{3}a$ .

This consideration is true for any tube, i.e. the Brillouin zone of a tube is a set of  $N$  parallel lines in the circumferential direction. The length, the number, and the orientation of these lines with respect to the hexagonal graphene Brillouin zone depend on the chiral indices  $(n, m)$  of a tube.

The electronic structure of a nanotube can be defined now in its first Brillouin zone. The electronic states along the  $\mathbf{k}_z$ -direction are the Bloch functions similar to those of three-dimensional crystals. In the  $\mathbf{k}_\perp$ -direction, however, they are discrete.

The main idea of the Zone-folding approximation is that the electronic band structure of a nanotube is given by the electronic energies  $E^\pm(k_x, k_y)$  of graphene (eqs. (A26) and (A27) from the Appendix), but only along the allowed  $\mathbf{k}_\perp$  lines.

Therefore, the energy dispersion of a tube corresponds to a set of the cross sections of a 3D graphene dispersion  $E^\pm(k_x, k_y)$  appearing due to cutting the plot with the  $N$  parallel planes related to different values of the wavevector  $\mathbf{k}_\perp$  (Fig. 3.4).

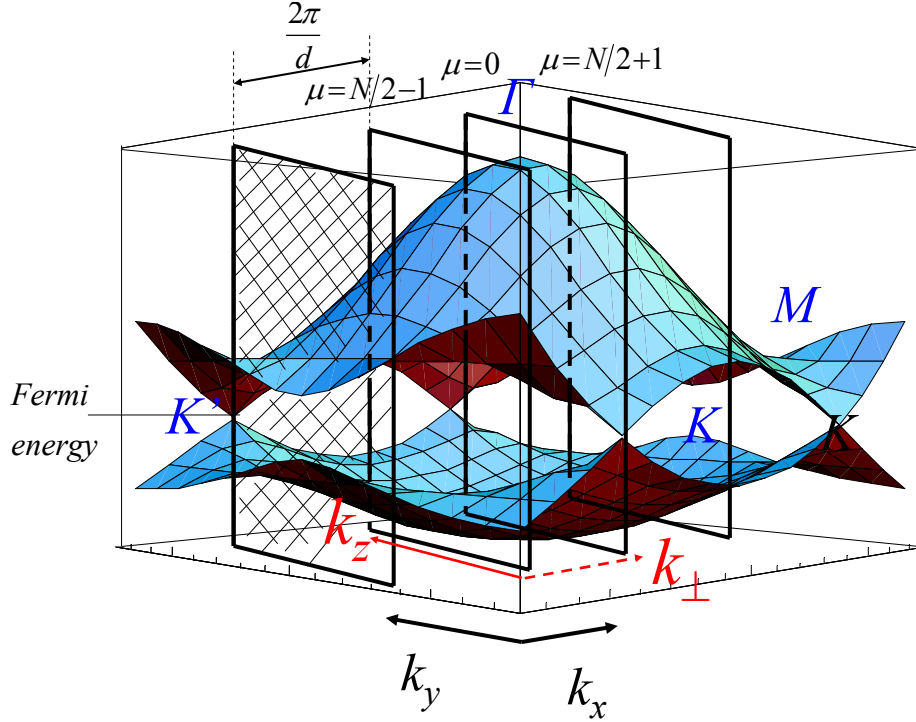


**Figure 3.4** The 3D energy dispersion surface  $E^+(k_x, k_y)$  of the graphene cut by  $N$  parallel planes; the nanotube wavevector  $k_z$  within the plane takes values  $(-\pi/\sqrt{3}a; \pi/\sqrt{3}a)$ ; each plane corresponds to a certain value of the wavevector  $k_\perp = 2\mu/d$  depending on  $\mu$ ;  $k_x$  and  $k_y$  are the graphene wavevectors in Cartesian coordinates (in general, not parallel to  $k_z$  and  $k_\perp$ ).

The graphite is a semi-metallic material with the electronic bands crossing the Fermi energy at the  $K$ -points. In a nanotube the distances between the parallel lines (or planes in Fig. 3.4) corresponding to different values of the  $k_\perp$ -wavevectors and the orientation of planes are determined by the chiral indices  $(n, m)$ . For different tubes the allowed  $k_\perp$ -lines either cross or do not cross the  $K$ -point depending on  $(n, m)$ . Tubes with the wavevectors crossing the  $K$ -point are metallic. The tubes whose allowed wavevectors do not cross the  $K$ -point are semiconducting with a moderate band gap of about 0.5 eV.

The geometric condition for the wavevector  $k_\perp$  to cross the  $K$ -points (metallic properties) is fulfilled when the projection of the vector  $\Gamma K$  on vector  $C_h$  in Fig. 3.5 contains an integer number  $\mu$  of the  $k_\perp$  wavevectors. The distance  $\Gamma K$  defined by the vector  $k$  equals to  $(b_1 - b_2)/3$ . Therefore:

$$k \cdot C_h = 2\pi\mu = \frac{1}{3}(b_1 - b_2) \cdot (na_1 + ma_2). \quad (3.5)$$

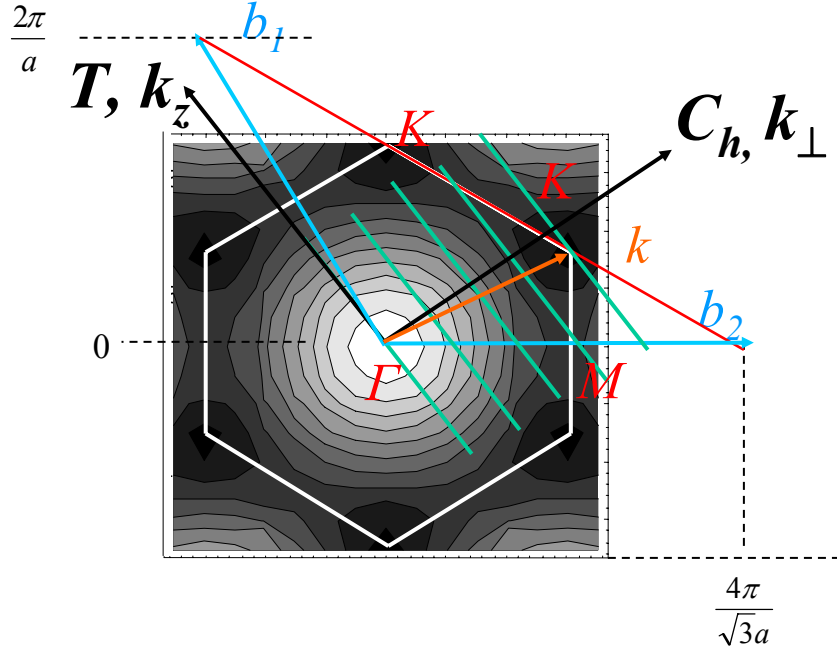


**Figure 3.5** The construction of the Brillouin zone of a nanotube with metallic properties (the parallel  $\mathbf{k}_\perp$  - lines cross the  $K$ -point) (see text for details).

Taking into account eq. (A.8) from the Appendix, one obtains an important relation between the numbers  $\mu$ ,  $n$  and  $m$ :

$$\mu = \frac{1}{3}(n - m). \quad (3.6)$$

This equation gives the condition for a tube with indices  $(n, m)$  to have metallic properties: the difference  $(n - m)$  must be a multiple of 3, then  $\mu$  is an integer. In the case of a semiconducting tube, the wavevector  $\mathbf{k}_\perp$  can approach the  $K$ -point by a distance of  $1/3d$  or  $2/3d$ . It follows from possible remainders of  $(n - m)/3$ . This means that  $1/3$  of all possible tubes are metallic and  $2/3$  are semiconducting.

Finally, the band structure of any nanotube can be evaluated using the energy dispersions of graphene (eqs. (A26) and (A27) from the Appendix) together with expressions for the nanotube wavevectors  $\mathbf{k}_\perp$  (3.4) and  $\mathbf{k}_z$  (3.4'). As an example, the band structure for the metallic tube  $(5, 5)$  is shown in Fig. 3.6.

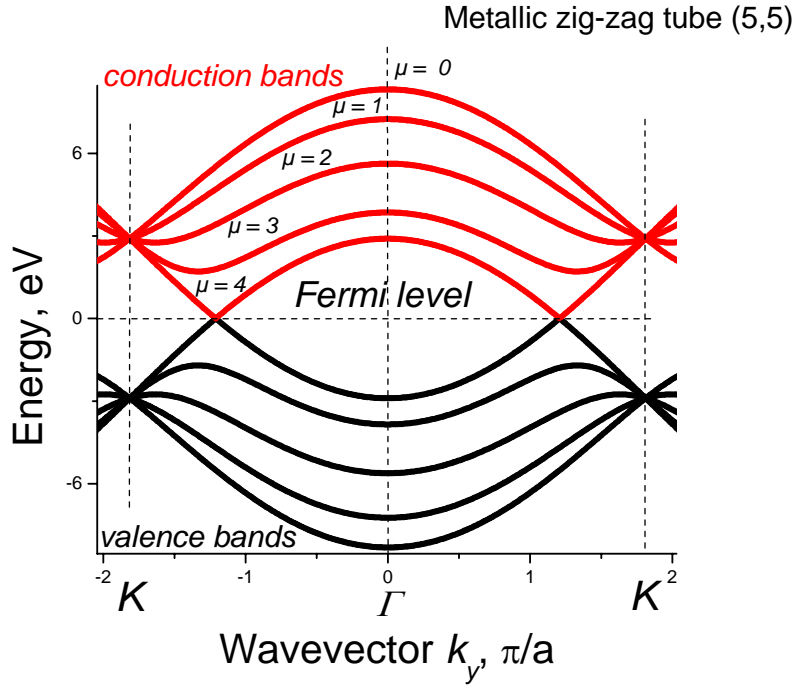


**Figure 3.6** Electronic energy dispersion (conduction and valence bands) of the metallic zigzag nanotube (5, 5) calculated within the tight-binding model (see text for details).

The set of curves is obtained by cutting the 3D-dispersion surface (Fig. 3.4) with  $N = 5$  parallel planes in the  $k_x$ -direction.

Here  $k_x = 2\mu/d$  and  $k_y = (-2\pi/\sqrt{3}; 2\pi/\sqrt{3}]$ ,  $\mu$  takes values  $-N/2+1, \dots, 0, N/2$ . The electronic transitions occur between the points of the minimum energy in the dispersion curves, i.e., near the  $K$ -points. These points are important for those physical phenomena where the electronic transitions occur, i.e. the photoluminescence or the resonance Raman scattering process (see *Chapter 4*). It is convenient to consider only the linear term of the energy dispersion expression (eqs. (A26) and (A27) from the Appendix) expanded near the  $K$ -point:

$$E^\pm(\vec{k}) = \varepsilon_{2p} \pm (\gamma_0 - s_0 \varepsilon_{2p}) f(\vec{k}) + \dots = \pm \frac{\sqrt{3}}{2} \gamma_0 k a. \quad (3.7)$$

This simplification makes the bands symmetric near the  $K$ -point and reduces the volume of calculation of the electronic band structure in a first approximation.

### 3.2 Electronic density of states for carbon nanotubes

The electronic density of states (DOS) is defined as the number of available electron states for a given energy interval. The DOS is of great importance for many physical phenomena like conductivity, optical emission, etc. In carbon nanotubes the one-dimensional DOS gives rise to the resonant Raman scattering as well as intensive interband transitions in the spectra of the optical absorption and emission. The DOS is

known to depend strongly on the dimension of the system. Figure 3.7 shows schematically the DOS for a three- (3D), two- (2D), one- (1D), and zero- (0D)-dimensional electronic system. In 3D crystals the DOS function above the band gap usually rises as the inverse square root of the energy. A two-dimensional DOS exhibits a step-like function; in a 1D case it diverges as an inverse square root of the energy. Finally, in the zero-dimensional system like an atom the DOS has a delta-function form [109].

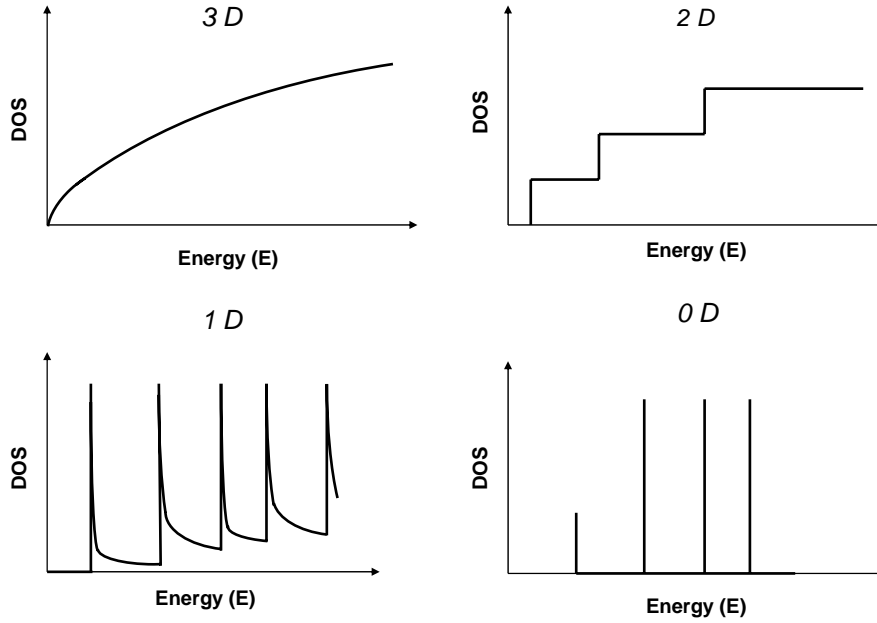


**Figure 3.7** Electronic DOS plotted versus energy for three-dimensional (bulk), two-dimensional (quantum well), one-dimensional (quantum wire, nanotube) and zero-dimensional (quantum dot) systems (see [109]).

In the general case, the electronic DOS for a 1D object can be written as [23]:

$$n(E) = \frac{2}{q|k_z|} \sum_i \int dk_z \delta(k_z - k_i) \left| \frac{\partial E^\pm(k_\perp, k_z)}{\partial k_z} \right|. \quad (3.8)$$

Here  $k_i$  is given by  $E - E^\pm(k_\perp, k_z) = 0$ , and  $q|k_z| = 4\pi^2 d / (3^{1/2} a_0^2)$  is the total area of the nanotube Brillouin zone and  $E^\pm(k_\perp, k_z)$  is the linear electronic energy dispersion near the  $K$ -point given by eq. (3.7). After some calculations [13] the DOS function of the nanotubes can be expressed as:

$$n(E) = \frac{4a_0}{\pi^2 d \gamma_0} \sum_{m=-\infty}^{\infty} g(E, E_\mu), \quad (3.9)$$

where  $a_0$  is the graphite lattice constant,  $d$  is a nanotube diameter,  $\gamma_0$  is the tight-binding integral (see the Appendix),  $\mu$  is a discrete number, characterizing the

quantized component of the wavevector  $k_{\perp}$ ,  $E_{\mu}$  is the minimum value of the  $\mu$ -th energy dispersion. The function  $g(E, E_{\mu})$  is given by:

$$g(E, E_{\mu}) = \begin{cases} |E|/\sqrt{E^2 - E_{\mu}^2}, & \text{if } |E| > |E_{\mu}|, \\ 0, & \text{if } |E| < |E_{\mu}|. \end{cases} \quad (3.10)$$

Expression (3.10) leads to the divergence of  $g(E, E_{\mu})$  at  $E = E_{\mu}$ , implying that the electronic DOS function must have  $\mu$  critical points with a high amplitude. These divergences are called the van Hove singularities (vHs) [24] and play an important role in many physical phenomena. In Figure 3.8 the electronic band structure and the DOS for two kinds of carbon nanotubes – the metallic and the semiconducting are schematically presented.

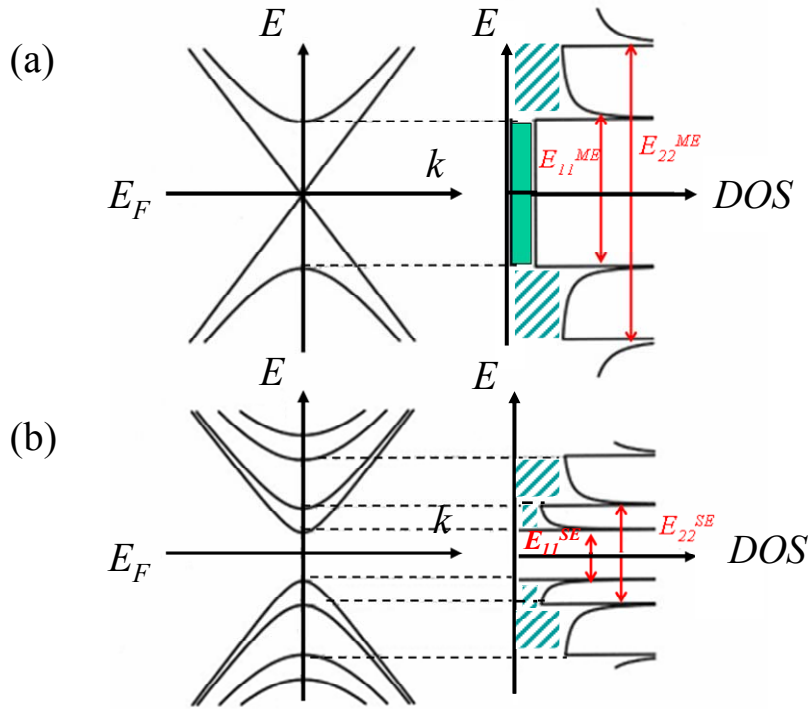


**Figure 3.8** Electronic band structure and the DOS function schematically shown for metallic nanotubes (a) and semiconducting nanotubes (b);  $E_{\mu} \equiv E_{11}^{SE}, E_{22}^{SE}$  and  $E_{\mu} \equiv E_{11}^{ME}, E_{22}^{ME}$ .

Fig. 3.8 (a) shows the energy dispersion of a metallic tube whose bands cross at the Fermi energy  $E_F$  ( $E_F$  is set as zero energy). These crossing bands result in a non-zero DOS at  $E = 0$  (area marked grey in Fig 3.8 (a)).

The electronic bands of a semiconducting nanotube (Figure 3.8 (b)) do not cross the Fermi level. The corresponding DOS has zero value for  $E < E_{\mu}$  (see eq. (3.10)).

Each carbon nanotube has a unique DOS function with a set of individual van Hove singularity peaks separated by the energies  $E_{\mu} = E_{ii}$  ( $ii \equiv \mu$ ). DOS as well as the separation energies  $E_{ii}$  are thus the “identity characteristics” of a tube.

In order to illustrate the manifestation of DOS in CNTs a *Kataura plot* is presented in Figure 3.9. The energy separations  $E_{ii}$  between the vHs of all the tubes with all possible geometries ( $n, m$ ) are plotted versus the tube diameter  $d$ , in the range of

energies [0 – 3eV] and diameters [0 – 3nm]. The separation energy defines the energy gap between the minima of the conduction bands and maxima of the valence bands.

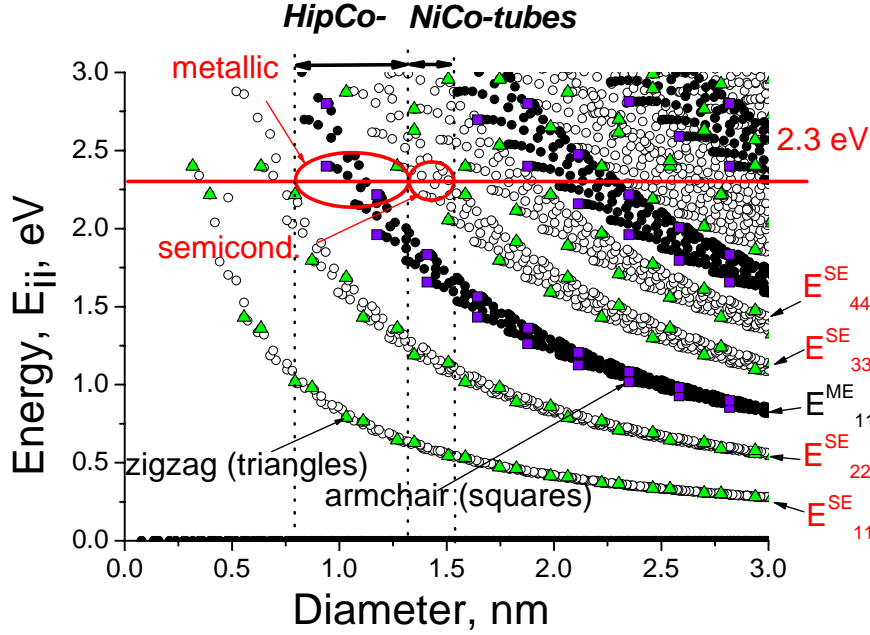


**Figure 3.9** The *Kataura plot* of the energy separations  $E_{ii}$  in DOS as a function of the tube diameter  $d$  for all the possible tubes in the diameter range [0 – 3 nm] and the energy range [0 – 3 eV]; the tight-binding model calculation done with the eq. (A29) from the Appendix. For the abbreviation of *HipCo* and *NiCo*-tubes see Section 5.1.

The dots in the *Kataura plot* (energies  $E_{ii}$ ) form the branches with constant  $\mu$ , i.e. the semiconducting tube branch with  $\mu = 1$  (first interband transition energies  $E_{11}^{SE}$ ), with  $\mu = 2$  (second interband transition energies  $E_{22}^{SE}$ ), the metallic tube branch with  $\mu = 1$  (first interband transition energies  $E_{11}^{ME}$ ), the semiconducting with  $\mu = 3 \dots$ , etc.

### 3.3 Models for carbon nanotube assignment

One of the most important questions in CNT science is how to determine the  $(n, m)$  structural indices of a tube. It can be done *directly* from the experiment or with the help of a good theoretical model which can transform the experimental data into  $(n, m)$  indices.

Several attempts were made to extract the  $(n, m)$  – indices from scanning tunnelling microscopy (STM) experiments [25, 26] and from Raman scattering experiments [18, 30, 31], plenty of works are devoted to different assignment models which transform the experimental values  $\{E_{ii}, \omega_{RBM}\}$  obtained from the Raman experiment [18] or the values  $\{E_{11}, E_{22}\}$  obtained from the photoluminescence (PL) experiment [6, 34, 62] into  $(n, m)$ .

The simplest Tight-Binding (TB) model combined with a Zone-folding (ZF) approximation which connects the energies of the electronic transitions  $E_{ii}$  of individual tubes with their structural indices  $(n, m)$  are considered in the Appendix. As an example of how the TB model works for the tube assignment, the energy separations between the vHs were plotted as a function of the radial breathing mode

(RBM) frequency  $\omega_{\text{RBM}}$  (Fig. 3.10). The RBM frequencies were calculated using the following semi-empirical relation [13]:

$$\omega_{\text{RBM}} [\text{cm}^{-1}] = 223.5/d [\text{nm}] + 12.5. \quad (3.11)$$

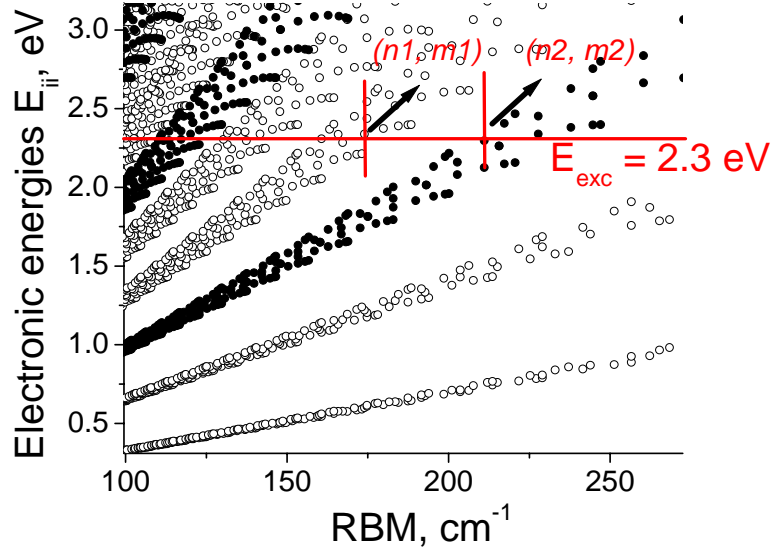


**Figure 3.10** Energy separations  $E_{ii}$  between the vHs calculated within the TB model as a function of the RBM frequency  $\omega_{\text{RBM}}$ .

From this plot one can obtain the electronic energy  $E_{ii}$  (close to the  $E_{\text{exc}}$ ) corresponding to the experimental RBM frequency of a certain tube and determine its diameter  $d$  using eq. (3.11). Then a pair of indices  $(n, m)$  can be extracted from an appropriate theoretical model.

The simplest TB model satisfies only the qualitative description of the nanotube band structure. It does not need large computational resources, but it fails in the precise assignment of the experimental results. The first principles calculation, however, is not able to give a similar *Kataura plot* (Fig. 3.9) due to a huge volume of computation.

More advanced assignment models were developed recently. These are, for example, a *modified TB model*, where the effect of curvature of the graphene sheet is taken into account [33, 34] as well as a TB model extended to the *third nearest-neighbour* carbon atoms [13]. Finally, a great success was achieved with introducing the *semi-empirical formulae* for the first and second interband transitions of the semiconducting tubes (eq. (3.12) and (3.12')). These data were derived from photoluminescence experiments on individual CNTs in aqueous dispersions [6]. The first and second interband transition frequencies (wavenumbers) are given as follows [6]:

$$\nu_{11} [\text{cm}^{-1}] = \frac{10^7 \text{ cm}^{-1}}{157.5 + 1066.9 \cdot d} + \frac{A_1 \cos(3\theta)}{d^2}, \quad (3.12)$$

$$\nu_{22} [\text{cm}^{-1}] = \frac{10^7 \text{ cm}^{-1}}{145.6 + 575.7 \cdot d} + \frac{A_2 \cos(3\theta)}{d^2}, \quad (3.12')$$

where  $\nu_{ii} [\text{cm}^{-1}] = (E_{ii} [\text{eV}] \cdot 10^7)/1240$ ;  $A_1 = -710 \text{ cm}^{-1}$  for  $(n - m) \bmod 3 = 1$ , or  $A_1 = 369 \text{ cm}^{-1}$  for  $(n - m) \bmod 3 = 2$ , and  $A_2 = 1375 \text{ cm}^{-1}$  for  $(n - m) \bmod 3 = 1$  or  $A_2 = 1475 \text{ cm}^{-1}$  for  $(n - m) \bmod 3 = 2$ ;  $d$  is the tube diameter in nm and  $\theta$  is the chiral angle.

The semi-empirical expressions (3.12) and (3.12') for the electronic energies provide a perfect agreement between theoretical and experimental results [34, 39]. In Fig. 3.11 three models are compared:

- (a) a simple tight-binding model;
- (b) a semi-empirical model [6];
- (c) a model with the curvature effect of the graphite sheet (with scenarios I and II, see [34] for details).

The calculated electronic energies are shown with filled symbols in plots a, b, cI and cII). The experimental electronic energies  $E_{11}^{\text{SE}}$  and  $E_{22}^{\text{SE}}$  obtained from the PL spectra [39] are shown as crosses in plots a, b, and c).

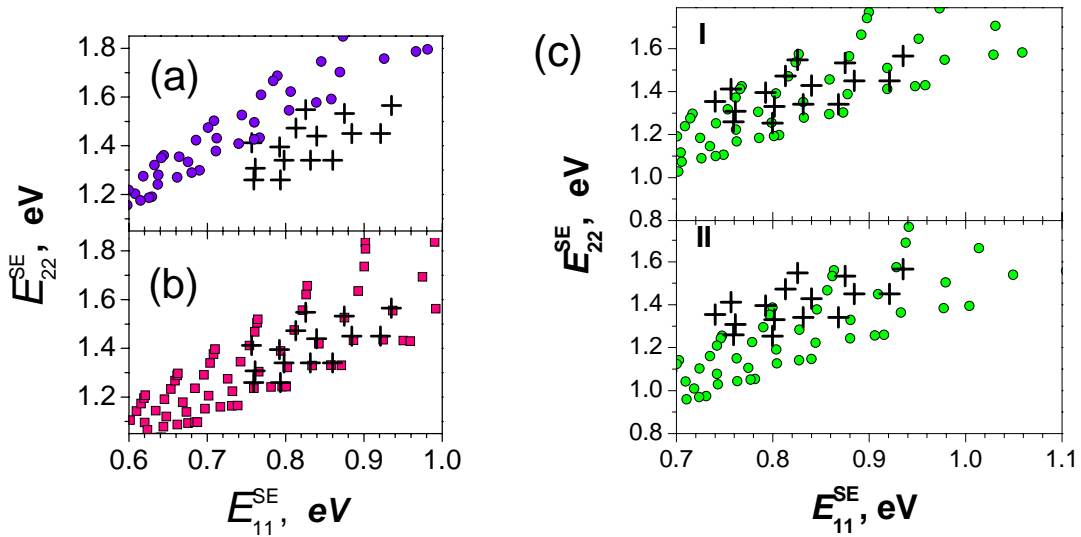


**Figure 3.11** Comparison between the theoretical electronic energies (filled symbols in plots a, b, and c) calculated within three different models (see text for details), and the experimental electronic energies  $E_{11}^{\text{SE}}$  and  $E_{22}^{\text{SE}}$  (crosses in plots a, b, and c) obtained from the photoluminescence spectra [39].

In order to test the consistency of a theoretical model one should compare its electronic energies with the photoluminescence data on individual CNTs dispersed in aqueous solutions. Thus, the experimental transition energies presented in Fig. 3.11 (crosses) were obtained from the PL spectra of the dispersions [39] containing mostly micelle-isolated tubes and having practically unperturbed electronic transitions. In the PL experiment a direct evaluation of the set of transition energies  $\{E_{22}^{\text{SE}}, E_{11}^{\text{SE}}\}$  of semiconducting nanotubes is possible due to the resonance excitation of the second electronic band with  $E_{22}^{\text{SE}} = E_{\text{exc}}$  and the following emission of an energy quantum  $E_{11}^{\text{SE}}$  through the band gap.

Comparing these four plots one can easily conclude that the plot in Fig. 3.11(b) based on the semi-empirical formulae [6] describes the experimental data better than the

other models. These semi-empirical relations are commonly used for assignment of the  $E_{22}^{\text{SE}}$ ,  $E_{11}^{\text{SE}}$  transition energies.

Among the disadvantages of the semi-empirical model are its limitation for higher transition energies of semiconducting tubes  $E_{ii}^{\text{SE}} > E_{22}^{\text{SE}}$ , and the absence of similar expressions for metallic nanotubes, as far as metallic tubes do not show any interband PL.

The calculation introduced by Reich *et al.* [13] based on the TB model with three nearest-neighbors gives both semiconducting and metallic interband transitions. The band structure of carbon nanotubes within this model is in a good agreement with the *ab-initio* result. However, the energy values do not coincide with the interband transitions from the semi-empirical formulae.

Since the experimentally available laser energy  $E_{\text{exc}} = 2.3$  eV excites the high energy electronic bands  $E_{11}^{\text{ME}}$  and  $E_{33}^{\text{SE}}$  in the investigated *HipCo*- and *NiCo*-nanotube\* samples (Fig. 3.9), neither a simple inaccurate TB model nor the semi-empirical formulae with their restriction for higher electronic transitions can be used in the present work. On the other hand, the *empirical* electronic transition energies obtained from the resonance Raman spectroscopy [18] will be applied in *Chapter 5* for the analysis of the experimental results.

\*For the abbreviation of *HipCo* and *NiCo*-tubes see Section 5.1.

### 3.4 Boron-carbonitride nanotubes ( $B_xN_yC_z$ -NTs)

The electronic band structure of carbon nanotubes is unique, reflecting the 1D nature of these molecular nanocrystals. Sharp van Hove singularities in the electronic DOS make physical properties of carbon nanotubes very specific and highly resonant (section 3.2). It is reasonable to assume that the other one-dimensional objects, at least, the nano-objects which are very close structurally to CNTs also have a similar electronic band structure. Boron-carbonitride nanotubes ( $B_xN_yC_z$ -NTs) produced from carbon nanotubes are the structural analogue of CNTs, where the carbon atoms in the graphite hexagonal sheet are partially substituted by B and N atoms. However, the electronic structure of  $B_xN_yC_z$ -NTs appears to be different. Moreover, it strongly depends on the concentration of B and N atoms inside the carbon nanotube framework. In the following section, the electronic properties of  $B_xN_yC_z$ -NTs will be considered from the theoretical point of view within a tight-binding (TB) model.

Compared to CNTs, there are not so many theoretical publications on the electronic structure of boron-carbonitride nanotubes. So far, the calculations on the stable structures of  $BC_2N$ ,  $BC_3$ ,  $CN$  and  $BC_2N$  [20, 21, 79, 81] have predicted some interesting properties of those objects such as either metallic or semiconducting behavior. At the same time, a  $B_xN_yC_z$  nanotube with all possible varieties of its element compositions  $x$ ,  $y$ ,  $z$  is a very complicated system for a detailed theoretical study.

In a first approximation, however, the band structure of  $B_xN_yC_z$ -NTs as a function of the concentration of boron and nitrogen ( $x + y$ ) has already been evaluated within a TB model [22]. This relatively simple model gave essential qualitative features of the electronic properties of boron-carbonitride NTs.

In this approach  $B_xN_yC_z$ -NTs are composed of randomly distributed B, N and C atoms (so called  $B_xN_yC_z$ -alloys). The concentration of boron and nitrogen is considered to be the same for simplicity ( $x = y$ ). The configuration where the equal amount of B and N is replaced by the carbon atoms is expected to describe actual systems obtained by doping of the BN-NTs with C. The calculation is performed for two types of zigzag nanotubes of different diameters: (metallic (9, 0) and semiconducting (10, 0).

The TB model for  $B_xN_yC_z$ -NTs implies some simplifications such as a uniform transfer integral  $\gamma_0$  regardless of the atomic configurations. Additionally, the local energies of boron and nitrogen is considered to be symmetric around that of carbon ( $U_{\text{Boron}} = \gamma_0 = 3\text{eV}$ ,  $U_{\text{Carbon}} = 0$ , and  $U_{\text{Nitrogen}} = -\gamma_0 = -3\text{eV}$ ). The band gap of a BN sheet is given by  $2\gamma_0$ . The calculation starts from a pure BN nanotube with further replacement of ( $x + y$ ) amount of B and N atoms by carbon at random.

Fig. 3.13 shows the DOS as a function of the ( $x + y$ ) concentration (bottom-up increasing) for the metallic (9, 0) nanotube calculated within a TB model described above [22].

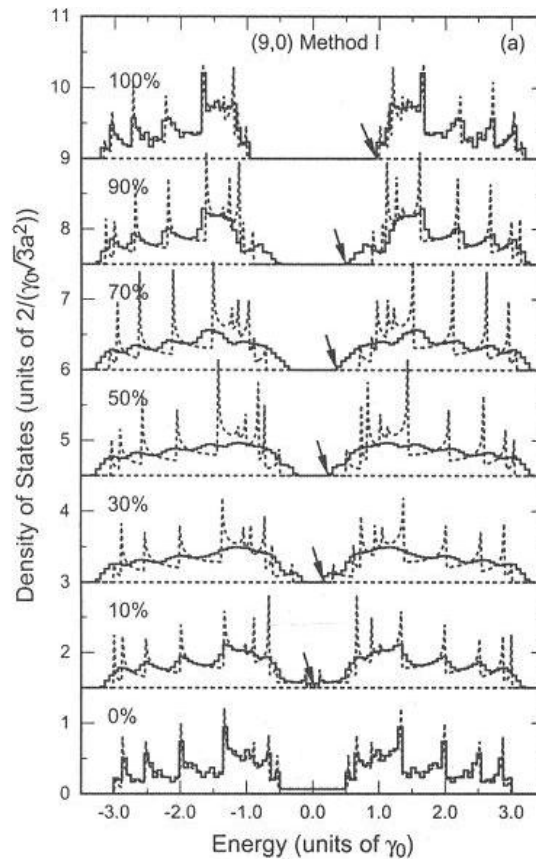


**Figure 3.13** Electronic DOS as a function of boron and nitrogen concentration ( $x + y$ ) (bottom-up increasing from 0 to 100%) for the metallic (9, 0) nanotube calculated within a TB model [22];  $\gamma_0 = 3\text{eV}$ .

For two starting CNTs (9, 0) and (10, 0) the result of the evaluation of the electronic DOS as a function of the concentration ( $x + y$ ) inside the cage of  $B_xN_yC_z$ -NT can be summarized as follows:

- broadening of the vHs peak in the DOS with increasing of the ( $x + y$ ) concentration in both metallic and semiconducting CNTs up to ( $x + y$ )  $\approx 0.6$ ; further increasing of ( $x + y$ ) results in more and more structured vHs peaks due to the transformation of a  $B_xN_yC_z$ -nanotube into a BN-nanotube;
- appearance of the band gap for the metallic (9, 0) CNT, which grows with increasing of the ( $x + y$ ) concentration (up to  $\approx 6$  eV for a BN-NT);
- increasing of the band gap value for the semiconducting (10, 0) CNT with increasing of the ( $x + y$ ) concentration (up to  $\approx 6$  eV for a BN-NT);
- difference between the energy gap in the DOS and the optical gap at high concentrations of ( $x + y$ ) due to the special overlap of the wavefunctions with other states.

The TB model gives the electronic band structure as a function of the concentration ( $x + y$ ) in a first approximation. However, this result can be very useful in the analysis of the concentration limits ( $x + y$ ) in  $B_xN_yC_z$ -NTs at which some physical effects, similar for those in CNTs can still be observed. For example, the concentration limit ( $x + y$ ) for the resonance Raman scattering in  $B_xN_yC_z$ -NTs at  $E_{\text{exc}} = 2.3$  eV is about 0.74 (Fig. 3.14). This concentration corresponds to the band gap value  $\approx 2.3$  eV.  $B_xN_yC_z$ -NTs with ( $x + y$ )  $> 0.74$  cannot contribute to the Raman signal since their band gap values become larger than 2.3 eV (see *Chapters 4 and 7*).

Fig. 3.14 presents the band gap values of the nanotubes (10, 0) and (9, 0) vs.  $(x + y)$  concentration calculated within the TB model described above [22].

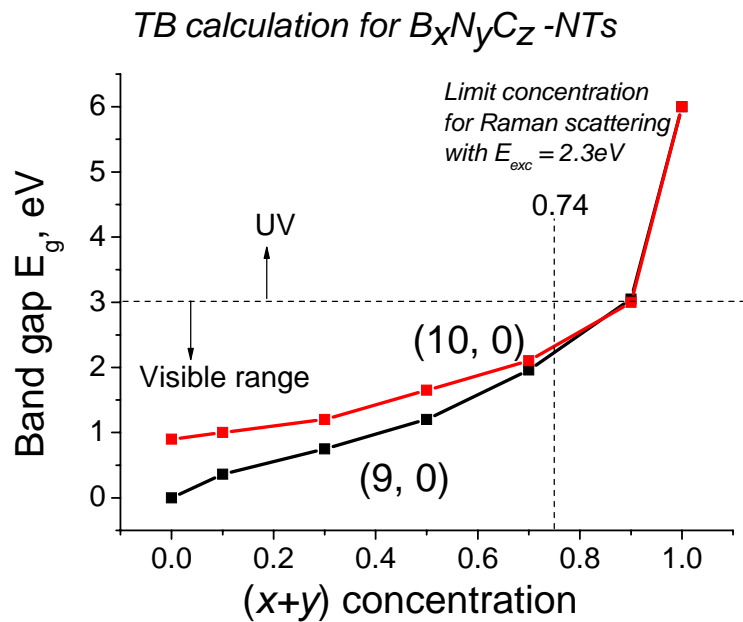


**Figure 3.14.** Band gap values as a function of B and N concentration  $(x + y)$  calculated within the TB model [22] for the semiconducting (10, 0) and metallic (9, 0) nanotubes.

This plot reflects the general tendency of the band gap increasing for the semiconducting nanotubes and also opening of the band gap and its increasing for the metallic nanotubes with increasing of the  $(x + y)$  concentration. The band gap values of both semiconducting and metallic nanotubes become similar ( $\approx 2$  eV) for the concentration of  $(x + y) \approx 0.7$ . For higher boron and nitrogen concentrations the tube chirality and diameter do not define the electronic properties (as for pure CNTs) since  $B_xN_yC_z$ -NT transforms into BN-NT. For the concentration  $(x + y) \approx 0.9$  the band gap value reaches a visible range of  $\approx 3$  eV. At higher doping concentrations  $B_xN_yC_z$ -NTs acquire insulating properties.

### 3.5 Summary

In this chapter the electronic band structure of carbon and  $B_xN_yC_z$ -nanotubes was considered within the Tight-Binding (TB) model combined with Zone-Folding approximation. Despite the approximate character of the results some of the most prominent characteristics of the nanotube band structure such as DOS, the electronic interband transition energies  $E_{ii}$  of CNTs and the band gap of  $B_xN_yC_z$ -NTs as a function of B and N concentration could be obtained within this model. These results will be very helpful in the following analysis of the experimental data.

# Chapter 4

## Experimental Techniques

In the following sections the resonance Raman scattering will be explained in relation to the electronic properties of carbon nanotubes. Usually the inelastic scattering of light in the visible range (Raman scattering) probes vibrational properties of the material in the center of the Brillouin zone so far as phonon excitations are the only energy loss mechanism. Figure 4.1(a) schematically presents the process of an inelastic scattering of light.

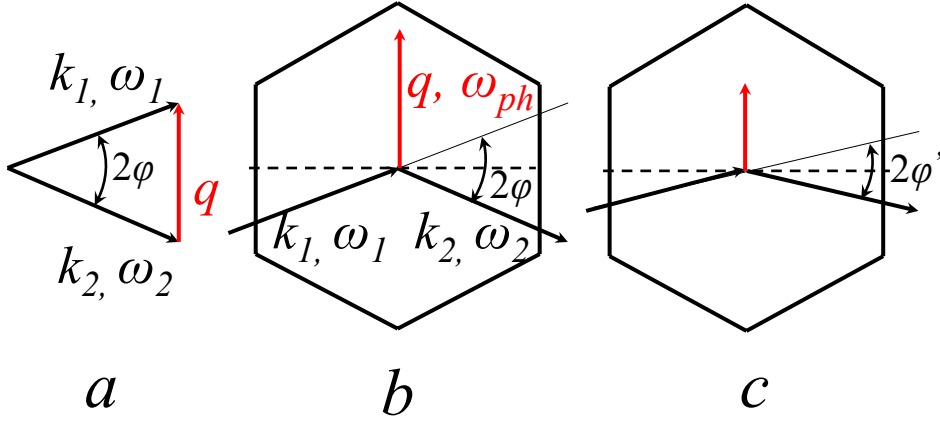


**Figure 4.1** Process of inelastic scattering of light is presented by the incoming wavevector  $\mathbf{k}_1$  and scattered wavevector  $\mathbf{k}_2$  and the wavevector transfer  $\mathbf{q}$ ;  $\omega_1$ ,  $\omega_2$  and  $\omega_{ph}$  denote the incoming, scattered and phonon circular frequencies, respectively.

Here  $\mathbf{k}_1$  and  $\mathbf{k}_2$  denote the wavevectors of the incoming and scattered photons, respectively, and  $\mathbf{q}$  is the scattering wavevector (or wavevector transfer);  $\omega_1$ ,  $\omega_2$  and  $\omega_{ph}$  are the incoming, scattered and phonon circular frequencies, respectively. The conservation of energy and quasi-momenta gives:

$$\begin{aligned} \hbar\omega_1 &= \hbar\omega_2 \pm \hbar\omega_{ph}, \\ \mathbf{k}_1 &= \mathbf{k}_2 \pm \mathbf{q}, \end{aligned} \quad (4.1)$$

where the plus and the minus signs indicate the creation and annihilation of a phonon. The wavevector transfer  $\mathbf{q}$  is

$$\mathbf{q}^2 = \mathbf{k}_1^2 + \mathbf{k}_2^2 - 2\mathbf{k}_1\mathbf{k}_2\cos(2\varphi), \quad (4.2)$$

where  $2\varphi$  is the angle between  $\mathbf{k}_1$  and  $\mathbf{k}_2$ . If  $|\mathbf{k}_1| \approx |\mathbf{k}_2|$ , then  $\mathbf{q}$  can be written as:

$$\mathbf{q} \approx 2\mathbf{k}_1 \sin \varphi. \quad (4.3)$$

This approximation can be always applied to inelastic scattering of light by phonons, because the phonon energy is typically of 1 or 2 orders of magnitude smaller than the photon energy in the visible range. Thus, incoming and scattered light have almost the same energy and therefore, the same absolute value of the momentum. With variation of the angle  $2\varphi$  the magnitude of the  $\mathbf{q}$ -vector changes (Fig. 4.1, b and c). The maximum value of  $\mathbf{q} = 2\mathbf{k}_i$  is fulfilled for  $2\varphi = 180^\circ$  (backscattering geometry).

The value of the wavevector of visible light  $k_i = 2\pi n/\lambda = 0.5 \cdot 10^{-2} \text{ \AA}^{-1}$  for  $\lambda = 500 \text{ nm}$  and a material with refractive index  $n = 4$ . In contrast, the extension of the Brillouin zone (BZ) is  $\pi/a$ , i.e. the range of the phonon wave vectors is  $\approx 1 \text{ \AA}^{-1}$ . Therefore, the maximum momentum transfer  $\mathbf{q} = 2\mathbf{k}_i$  is by about two orders of magnitude smaller than the BZ space. As a result, only the  $\Gamma$ -point phonons with  $\mathbf{q} \approx 0$  can be probed with Raman scattering. Phonons with larger  $\mathbf{q}$  can be measured by higher-order Raman scattering, where two or more phonons with opposite wave vectors are involved ( $\mathbf{q}_1 + \mathbf{q}_2 \approx 0$ ), or in a process of scattering by a defect.

There are some other techniques for measuring phonon dispersions through the whole Brillouin zone such as the inelastic neutron scattering and inelastic X-ray scattering. For the neutron scattering, de Broglie wavelength of the neutron depends on neutron energy as

$$\lambda = \frac{2\pi\hbar}{\sqrt{2mE}}. \quad (4.4)$$

Here  $E$  is the kinetic energy of the neutron. Usually  $k_{\text{neutron}} \sim 1 \text{ \AA}^{-1}$  (two orders of magnitude larger than for visible light), therefore the  $K$ -phonons at the edge of the Brillouin Zone can be also probed.

The neutron scattering experiment, however, requires a single crystal of the order of  $cm$  in size, which does not exist for CNTs. Inelastic X-ray scattering has several advantages such as small sample sizes and amount and is used for measuring phonon dispersions in CNTs [103].

## 4.1 Resonance Raman Scattering (RRS)

Ordinary Raman scattering (RS) studies yield information on low-energy excitations of molecules, liquids, and solids. The phonon energy in such experiments is restricted to states which are typically up to  $5 \times 10^{-2} \text{ eV}$  from the ground state of the system under study. The incoming and scattered frequencies do not carry any information about the system, but only their difference is important as well as the  $\mathbf{q}$ -vector, and the polarization of the scattered photon.

In contrast, Resonance Raman Scattering (RRS) allows exploring the spectrum of the material in the energy range of the photon energy itself, typically  $1 - 3 \text{ eV}$  for the experiments in visible range. For the RRS process the material under investigation needs electronic properties (the band gap or higher interband transition energies) to be in resonance with the excitation radiation, or, in other words, the laser excitation energy must be chosen equal to the electronic resonances of the material. In this respect RRS is similar to absorption and emission experiments.

In such a resonant process the incoming photon induces not only molecular vibrations like for ordinary RS, but also excites electron-hole pairs, which recombine radiatively,

i.e., with emitting photons. Figure 4.2 shows schematically the Feynman diagram of a first-order resonant Raman process [35].

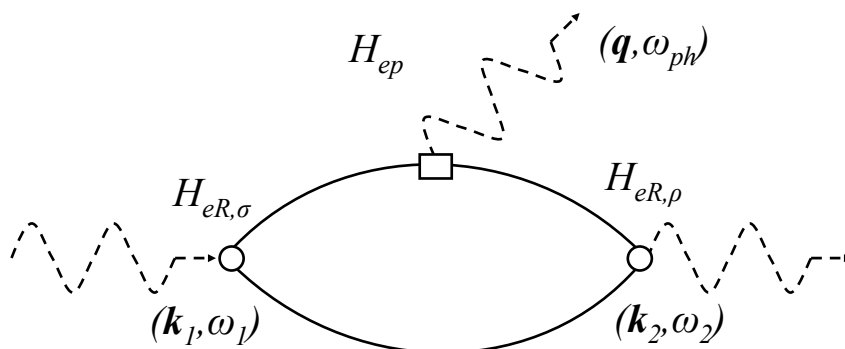


**Figure 4.2** Feynman diagram of a first-order resonant Raman process.

The process of RRS can be described to proceed in three steps:

- (i) a photon with the wavevector  $\mathbf{k}_1$ , circular frequency  $\omega_1$  and polarization  $\sigma$  interacts with electrons of matter exciting an electron-hole pair. The Hamiltonian for the interaction of radiation with electrons is  $H_{eR,\sigma}$ ;
- (ii) an electron-hole pair in a process of inelastic electron-phonon scattering emits a phonon with frequency  $\omega_{ph}$  (electron-phonon coupling Hamiltonian  $H_{ep}$ );
- (iii) Finally, an electron-hole pair recombines emitting the scattered photon  $\omega_2$  with polarization  $\rho$  (electron-radiation interaction Hamiltonian  $H_{eR,\rho}$ ).

Energy and momentum are conserved in this process according to Eq. (4.1). The  $\pm$  signs in Eq. (4.1) refer to Stokes and anti-Stokes scattering. The matrix element of the process presented in Fig. 4.2 is given by:

$$K_{2f,10} = \sum_{a,b} \frac{\langle \omega_2, f, i | H_{eR,\rho} | 0, f, b \rangle \langle 0, f, b | H_{ep} | 0, 0, a \rangle \langle 0, 0, a | H_{eR,\sigma} | \omega_1, 0, i \rangle}{(E_1 - E_{ai}^e - i\Gamma)(E_1 - \hbar\omega - E_{bi}^e - i\Gamma)}, \quad (4.5)$$

where  $|x, y, z\rangle$  and  $\langle x, y, z|$  are the incoming and outgoing energy states respectively, of photon ( $x$ ), phonon ( $y$ ), and electron ( $z$ ) for each step of the RRS. For example,  $|\omega_1, 0, i\rangle$  denotes the state with an incoming photon of energy  $E_1 = \hbar\omega_1$ , the ground state 0 of the phonon (no phonon excited), and the ground electronic state  $i$ ;  $\langle 0, 0, a|$  denotes the ground 0 photon energy (absorbed), the ground 0 state of phonon, and the electronic excited state  $a$ . The initial and the final electronic states are assumed to be the same; the sum is performed over all possible intermediate electronic states  $a$  and  $b$ . The final state of a phonon is denoted by  $f$ , the  $E_{ai}^e$  is the energy difference between the electronic states  $a$  and  $i$ ; the lifetime of the excited states  $\Gamma$  was assumed to be the same [35, 36].

Stokes and Anti-Stokes scattering processes are shown schematically in Fig. 4.3.

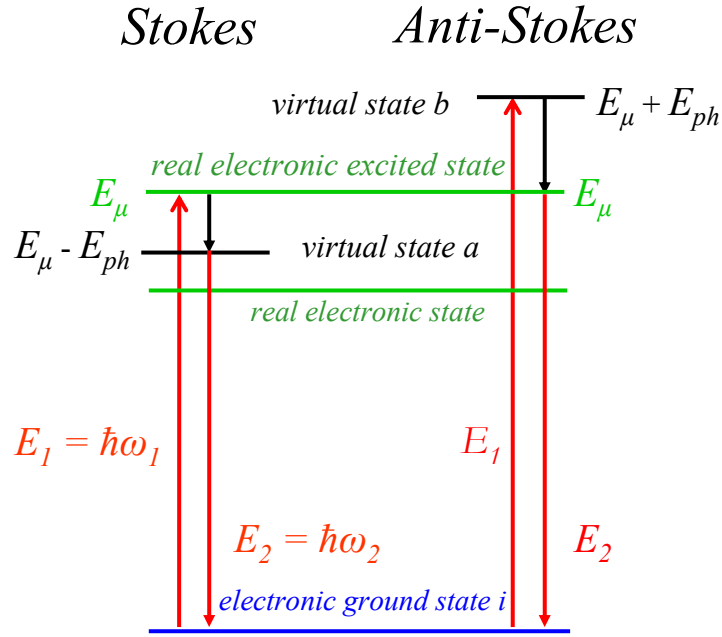


**Figure 4.3** Single-resonant Raman scattering with both Stokes and Anti-Stokes processes. In a Stokes process a real electronic state  $E_\mu$  is excited by the incident laser energy  $E_1 = E_\mu$ . Then, a transition to a virtual electronic state  $i$  is possible with emission of  $E_{ph}$  and a following recombination of the electron-hole pair with emission of  $E_2 = E_\mu - E_{ph}$ . An Anti-Stokes process corresponds to the excitation of a virtual electronic state  $ii$  with  $E_1$  and further transition to a real electronic state  $E_\mu$  with emission of  $E_{ph}$  and final recombination to a ground state with emission  $E_2 = E_\mu = E_1 - E_{ph}$ .

For a Stokes process the incident laser energy  $E_1$  plus the energy of a molecular vibration  $E_{ph}$  must be equal to the electronic transition energy  $E_\mu$ . If this condition is satisfied the Raman signal becomes very high. For an Anti-Stokes process the electronic transition energy must be equal to  $E_1 - E_{ph} = E_\mu$ . The intensity of the Anti-Stokes signal is much lower because the vibration energy is taken from the system. Thus, an Anti-Stokes process can only take place if the material system is originally in a state excited above the ground state, i.e. in a thermally or otherwise activated state. The probability to be in thermally activated state at room temperature is proportional to the Bose-Einstein thermal factor. For this reason the Anti-Stokes line has much lower intensity.

### Selection rules

The selection rules originate from symmetry considerations which determine whether the matrix element in eq. (4.5) is zero or not. The easiest way to solve this question is to consider conservation of the quasi-angular momentum  $\mu$  and the parity  $\sigma_h$  (applied only for achiral tubes) [13] because of the difficulty of a direct evaluation of  $K_{2f, 10}$ .

Both  $\mathbf{k}$  and  $\mu$  vectors form Brillouin zone of a carbon nanotube, where  $\mathbf{k}$  is the quasi-linear momentum, and  $\mu$  is considered to be a quasi-angular momentum, the scalar  $\mu$  is a quantum number and a projection of the quasi-angular momentum on the  $\mathbf{k}_\perp$  direction.

There are some restrictions for  $\mu$  to be a conserved quantum number. These restrictions imply considering only the first-order Raman scattering process with the

phonon vectors  $\mathbf{q} \approx 0$  (close to the  $\Gamma$ -point) and optical transitions in visible with  $\Delta\mathbf{k} \approx 0$  (vertical electronic transitions).

Since the initial and final electronic states for optical transitions have the same  $\mu$  and  $\sigma_h$ , the selection rules for the electronic part will be

$$\begin{cases} \Delta\mu = 0, \\ \sigma_h = +1. \end{cases} \quad (4.6)$$

A  $z$ -polarized optical transition ( $\mathbf{E} \parallel z$ ) conserves angular momentum  $\mu$  and changes the mirror parity  $\sigma_h$ . Therefore, the selection rules are:

$$\begin{cases} \Delta\mu = 0, \\ \sigma_h = -1. \end{cases} \quad (4.7)$$

For the transitions *polarized perpendicular to the tube axis* ( $\mathbf{E} \perp z$ ) the selection rules are:

$$\begin{cases} \Delta\mu = \pm 1, \\ \sigma_h = +1. \end{cases} \quad (4.8)$$

The change in angular momentum and parity induced by the absorption and emission of a photon must be compensated by a phonon. For the  $z$ -polarized incoming and outgoing light ( $zz$  - configuration) angular momentum  $\mu$  and parity  $\sigma_h$  are fully conserved by photons. As a result, only  $A_{1g}$  phonons are allowed in this scattering configuration [13]. In ( $xz$ ) or ( $zy$ ) scattering geometry  $\Delta\mu_{\text{phonon}} = \pm 1$ , and  $\sigma_{h,\text{phonon}} = -1$  giving rise to the  $E_{1g}$  phonon scattering. The intensity of the Raman signal is proportional to the square of the absolute value of the matrix element in eq. (4.5) [36]:

$$I_{\text{Raman}} \sim |K_{2f,10}|^2 \sim \left| \sum_{a,b} \frac{M}{(E_1 - E_{ai}^e - i\Gamma)(E_1 - \hbar\omega - E_{bi}^e - i\Gamma)} \right|^2, \quad (4.9)$$

where the summation is over all possible direct vertical transitions, which we can be converted into an integral over energy (see [36] for details):

$$I(E_{\text{laser}}) = \left| \int \frac{M}{[E_{\text{laser}} - E_{\mu} - i\Gamma][E_{\text{laser}} - E_{\mu} \pm E_{\text{ph}} - i\Gamma]} dE_{\text{laser}} \right|^2, \quad (4.10)$$

where  $M = M^i M^{\text{ep}} M^{\text{s}}$  and  $M^i$ ,  $M^{\text{ep}}$ ,  $M^{\text{s}}$  are the matrix elements for the electron-radiation absorption, electron-radiation emission, and for the electron-phonon interaction, respectively,  $E_{\text{laser}}$  is the laser excitation energy (re-named from  $E_1$  in eq. (4.9)),  $E_{\mu}$  is the energy of the real electronic transition, and  $E_{\text{ph}}$  is the phonon energy, and  $\Gamma$  is the inverse lifetime for the resonant scattering process and/or a broadening factor determined by environment condition (tube-tube interaction or interaction with other surroundings). Signs “+” and “-” are for Stokes and Anti-Stokes processes respectively.

## 4.2 Resonance Raman scattering and electronic DOS

The electronic DOS of carbon nanotubes close to  $1/\sqrt{E}$  - dependence can be directly observed in scanning tunnelling spectroscopy (STS) experiments, since the differential conductance  $dI/dV$  registered in the STS measurement is proportional to DOS [25, 26]. The Raman scattering experiment does not provide DOS directly. The RRS process, however, is highly resonant for carbon nanotubes. The intensity of the Raman signal rises by orders of magnitude if the excitation energy coincides with the energy separations between vHs. The variation of the Raman intensity with the excitation energy can be used for the characterisation of the van Hove singularities in the electronic DOS.

The Raman intensity for the first-order modes for carbon nanotubes as a function of laser excitation energy  $E_{\text{laser}}$  can be calculated using eq. (4.10) where the sum over electronic transitions is substituted by the integral over the *joint* density of states (JDOS)  $g(E_{\text{laser}}, E_{\mu})$ :

$$I(E_{\text{laser}}) = \left| \int M \frac{g(E_{\mu}, E_{\text{laser}})}{[E_{\text{laser}} - E_{\mu} - i\Gamma][E_{\text{laser}} - E_{\mu} \pm E_{\text{ph}} - i\Gamma]} dE_{\text{laser}} \right|^2. \quad (4.11)$$

This is because the Raman intensity for carbon nanotubes rather depends on the joint density of states (JDOS) than on DOS given by eq. (3.11). It means that in eq. (3.11) the values  $E^-(k_{\perp}, k_z)$  and  $E^+(k_{\perp}, k_z)$  in  $\partial E^{\pm} = \partial(E^- - E^+)$  must be evaluated for the same  $k_z$  (vertical transitions).

The Raman scattering experiment on single tubes for the set of excitation laser energies reproduces a profile of the van Hove singularity. In Figure 4.4 the intensity of the Raman signals (both Stokes and Anti-stokes) plotted versus the laser excitation energy for a certain single carbon nanotube is presented [30]. Raman intensity measured versus the laser excitation energy is called the *Raman resonance window*. With these resonance Raman windows measured for Stokes and Anti-Stokes processes an individual electronic transition of a certain tube can be found as a cross-point of two normalized resonance window profiles. For instance, the nanotube from Fig. 4.4 has the electronic transition energy of about 1.67 eV (see upper inset).

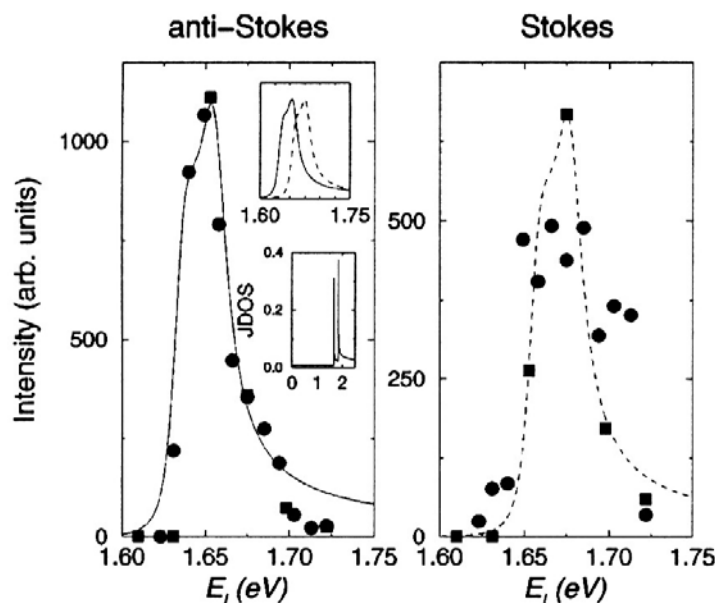


**Figure 4.4** Intensities of the Raman signals (normalized Stokes and Anti-stokes) plotted versus the laser excitation energy for a certain single carbon nanotube having the electronic transition energy of about 1.67 eV [30].

In this way, the electronic transition energy can be found as the mean energy between the Stokes and Anti-Stokes peaks:  $E_{\mu} = (E_S + E_{AS})/2$ . The experimental Stokes and Anti-Stokes profiles, however, have different intensities and must be normalized according to the ratio:

$$\frac{I_{AS}}{I_S} = \frac{n(E_{ph})}{n(E_{ph}) + 1}, \quad (4.12)$$

where  $n(E_{ph})$  is the Bose-Einstein thermal factor given by:

$$n(E_{ph}) = \frac{1}{e^{E_{ph}/k_B T} - 1}. \quad (4.13)$$

The next question to be discussed is the position of the maxima of the Stokes and Anti-Stokes peaks. According to last theoretical calculations of the Raman intensities *via* the evaluation of the electron-phonon matrix elements for the radial breathing mode [32] the position of the Raman peak in the case of large  $\Gamma$  parameter in eq. (4.11) (the case of interacting tubes) is rather  $E_{\mu} + E_{ph}/2$  than  $E_{\mu} + E_{ph}$ .

In the general case, the intensity of a resonant Raman signal depends on the chiral angle, tube diameter and so-called *family effect* for semiconducting CNTs, i.e. whether  $(3n + m) \bmod 3 = 1$  (S1-type) or  $(3n + m) \bmod 3 = 2$  (S2-type). For these two S1 and S2-types of semiconducting tubes different values of the matrix elements were predicted [31, 31]. Such a family-behavior was also confirmed experimentally [18].

In summary, the main factors influencing the resonant Raman intensity are:

- (i) nanotube diameter  $d$  and chiral angle;
- (ii) family effect (S1, S2-types) for semiconducting CNTs;
- (iii) nanotube orientation;

- (iv) diameter distribution in a sample;
- (v) interaction between nanotubes.

For the precise theoretical calculation of the Raman intensity one has to take into account all these factors. In a first approximation the matrix elements  $M$  for optical absorption, emission and electron-phonon interaction in eq. (4.11) are assumed to be constant. This is certainly a good approximation for the semiconducting tubes belonging to the same S1 or S2-type, and in the case of similar diameters and chiral angles. For the bulk materials with a distribution in tube diameters  $d$  and chiral angles  $\theta$ , the square-root singularities in joint density of states  $g(E_{\text{laser}}, E_{\mu})$  (eq. (3.13)) is usually approximated by a delta function at the maximum value of the van Hove singularity [27 – 29]. Using the property of a delta-function

$$\int_{-\infty}^{\infty} f(x)\delta(x) = f(0), \quad (4.14)$$

one can finally write the Raman intensity as:

$$I(E_{\text{laser}}) = A \left| \frac{1}{(E_{\text{laser}} - E_{\mu} - i\Gamma)(E_{\text{laser}} \pm E_{\text{ph}} - E_{\mu} - i\Gamma)} \right|^2, \quad (4.15)$$

where  $A$  lumps up parameters like tube distribution in a sample, their orientation and interaction, i.e. the external factors which have no connection to the tube structure  $(n, m)$ .

In the following consideration the modified expression (4.15) in the form of Ref. [30] will be used:

$$I(E_{\text{laser}}) = A \frac{1}{\left\{ (E_{\mu} - E_{\text{laser}})^2 + \left(\frac{\Gamma}{2}\right)^2 \right\} \left\{ (E_{\mu} - E_{\text{laser}} \pm E_{\text{ph}})^2 + \left(\frac{\Gamma}{2}\right)^2 \right\}}. \quad (4.16)$$

With this important equation the Raman intensities of carbon nanotubes will be calculated and the experimental results will be described in *Chapters 5, 6 and 7*.

### 4.3 Raman spectra of carbon nanotubes

As discussed in the previous sections, the RRS process yields information not only on the vibrational properties but also on the electronic states of carbon nanotubes. Raman spectroscopy can provide nanotube diameters,  $(n, m)$  indices and chiral angles, defect concentration, and influence of an environment and temperature on the band gap value. Different spectral parts of a typical Raman spectrum of single-walled CNTs are shown in Fig. 4.5 (a - d).

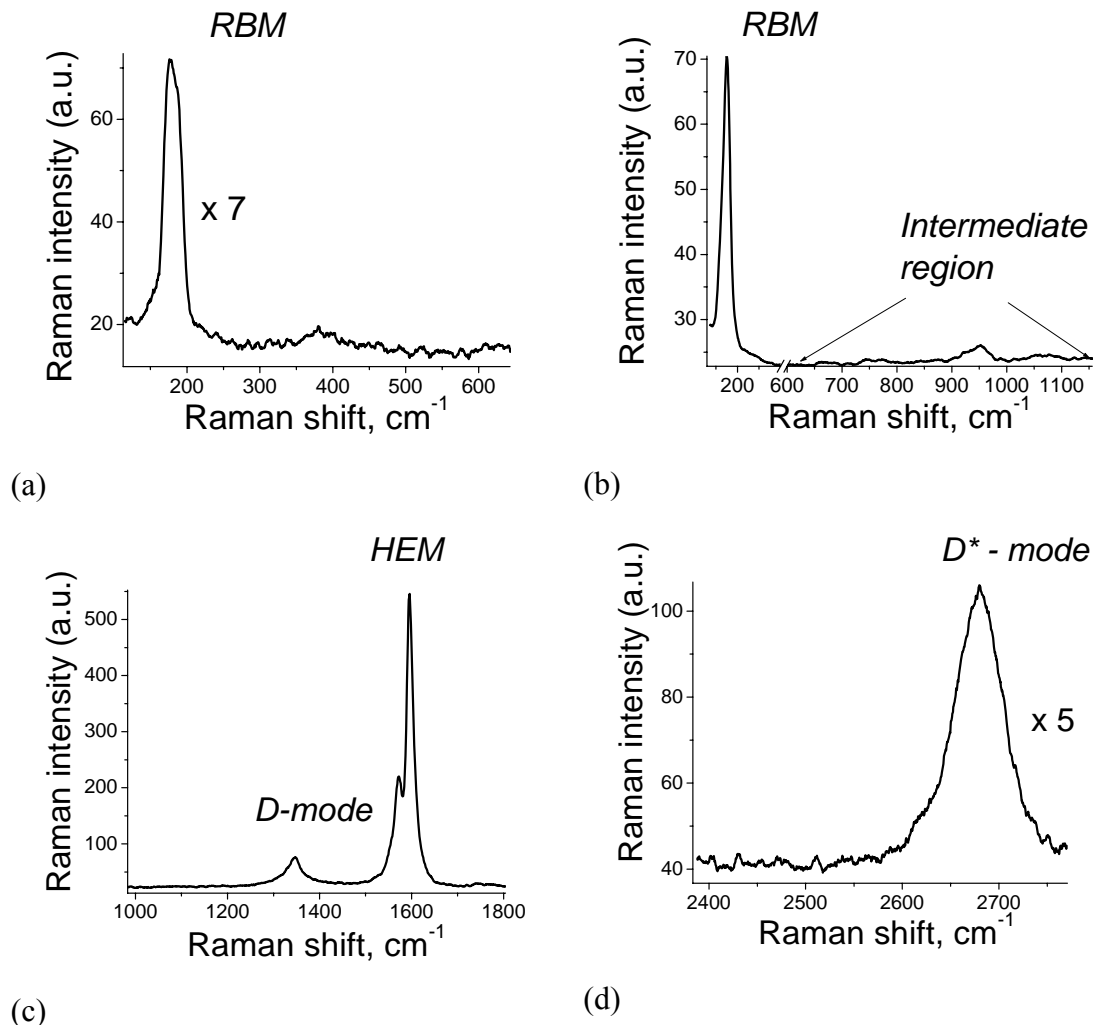


**Figure 4.5** Parts of a typical Raman spectrum of the sample of NiCo-nanotubes obtained at  $E_{\text{exc}} = 2.3$  eV: (a) the radial breathing mode (RBM); (b) RBM and the intermediate frequencies; (c) the high energy mode (HEM) and the D-mode; (d) the second-order D\* -mode.

The first-order spectrum is usually divided into a low-energy ( $0 - 500$  cm<sup>-1</sup>) and a high-energy ( $1000 - 3000$  cm<sup>-1</sup>) region reflecting different properties of carbon nanotubes. All the first-order Raman modes originate from the  $\Gamma$ -point active Raman vibration with  $q = 0$ . The D-mode and D\* -mode both are related to the second-order processes involving two phonons or a phonon and a defect with  $q_1 + q_2 = 0$ .

### RBM

The strongest low-energy mode (around  $100 - 300$  cm<sup>-1</sup>) is the fully symmetric radial breathing mode (RBM) (Fig. 4.5, a). The RBM mode corresponds to the radial expansion of the tube when all carbon atoms move in phase in a radial direction creating a breathing-like vibration of an entire tube. The RBM frequency is widely applied to determine the diameter of a tube. The analytical expression for the RBM was derived in terms of the force constants employed in a description of the phonon modes in the two-dimensional graphite [12, 37]. The Lagrangian for the tube unit cell with  $2N$  vibrating atoms can be expressed as

$$L = Nm\dot{r}^2 + N\left(\frac{a_{c-c}(r-r_0)}{r_0}\sqrt{\Phi}\right)^2, \quad (4.17)$$

where  $m$  is the mass of a carbon atom,  $r_0$  is the equilibrium radius of the tube,  $a_{c-c}(r-r_0)/r_0$  is the change in the bond length along the circumference,  $a_{c-c} = 0.114$  nm is the carbon nearest-neighbour distance, and

$$\sqrt{\Phi} = \sqrt{\frac{9}{16}\phi_r^1 + \frac{27}{8}\phi_r^2 + \frac{9}{4}\phi_r^3 + \frac{63}{8}\phi_r^4},$$

where  $\phi_r^1 = 36.5 \cdot 10^4$ ,  $\phi_r^2 = 8.8 \cdot 10^4$ ,  $\phi_r^3 = 3 \cdot 10^4$ ,  $\phi_r^4 = -1.92 \cdot 10^4$  dyn/cm are the experimental bond-stretching force constants. After solving the eq. (4.17) for  $r$ , the RBM frequency can be expressed as follows:

$$r = e^{a_{c-c}\sqrt{\frac{\Phi}{m}} \cdot \frac{1}{r_0}},$$

or

$$\omega_{\text{RBM}} = \frac{a_{c-c}}{r_0} \sqrt{\frac{\Phi}{m}} = \frac{13a_{c-c}}{\sqrt{md}} \cong \frac{224}{d}, \quad (4.18)$$

where  $d = 2r_0$  is the tube diameter.

This expression shows the general  $1/d$ -dependence of the RBM frequency on the diameter but is never used for the quantitative diameter estimations because of its approximate character. The more advanced empirical expression for the RBM frequency was introduced later on in a form of:

$$\omega_{\text{RBM}} = \frac{C_1}{d^k} + C_2(d). \quad (4.19)$$

The parameter  $C_1$  is constant and  $C_2$  probably depends on the diameter. These two values vary from paper to paper (summarized in [13] and [38]) depending on the model used for the estimation of the transition energies  $E_\mu$  versus diameters (see section 3.4) and the tube environment (*Chapter 5*).

For the experimental determination of  $C_1$  and  $C_2$  it is necessary to measure the electronic transition energies and the RBM frequencies  $\{E_\mu, \omega_{\text{RBM}}\}$  using resonance Raman windows (section 4.1.2). Then the experimental values  $\{E_\mu, \omega_{\text{RBM}}\}$  must be combined with the values  $\{E_\mu, d\}$  from a reliable theoretical model for at least two tubes. In this way one can obtain the equations for the coefficients  $C_1$  and  $C_2$ :

$$\omega_{\text{RBM1}}^{\text{exp}} = \frac{C_1}{d_1^{\text{theor}}} + C_2, \quad (4.20)$$

$$\omega_{\text{RBM2}}^{\text{exp}} = \frac{C_1}{d_2^{\text{theor}}} + C_2.$$

The RBM frequency reflects not only vibrational but also electronic properties of carbon nanotubes due to the strong coupling between electronic transitions and vibrational modes in one-dimensional systems. In Raman spectra  $\omega_{\text{RBM}}$  only from the

tubes having the electronic transition energies close to the laser excitation energy can be observed.

The resonance nature of Raman scattering in CNTs is illustrated in Fig. 4.6 (a). Here, the RBM frequencies of micelle-isolated carbon *HipCo*-nanotubes dispersed in aqueous solution are shown. Fig. 4.6 (b) explains the appearance of these peaks using the *Kataura plot* (section 3.2) for the electronic transition energies plotted versus tube diameters. The horizontal line denotes the laser excitation energy  $E_{\text{exc}} = 1.58$  eV. All the tubes with energies (circles in Fig. 4.6, b) close to this line give the RBM frequencies in the Raman spectra presented in Fig. 4.6 (a).

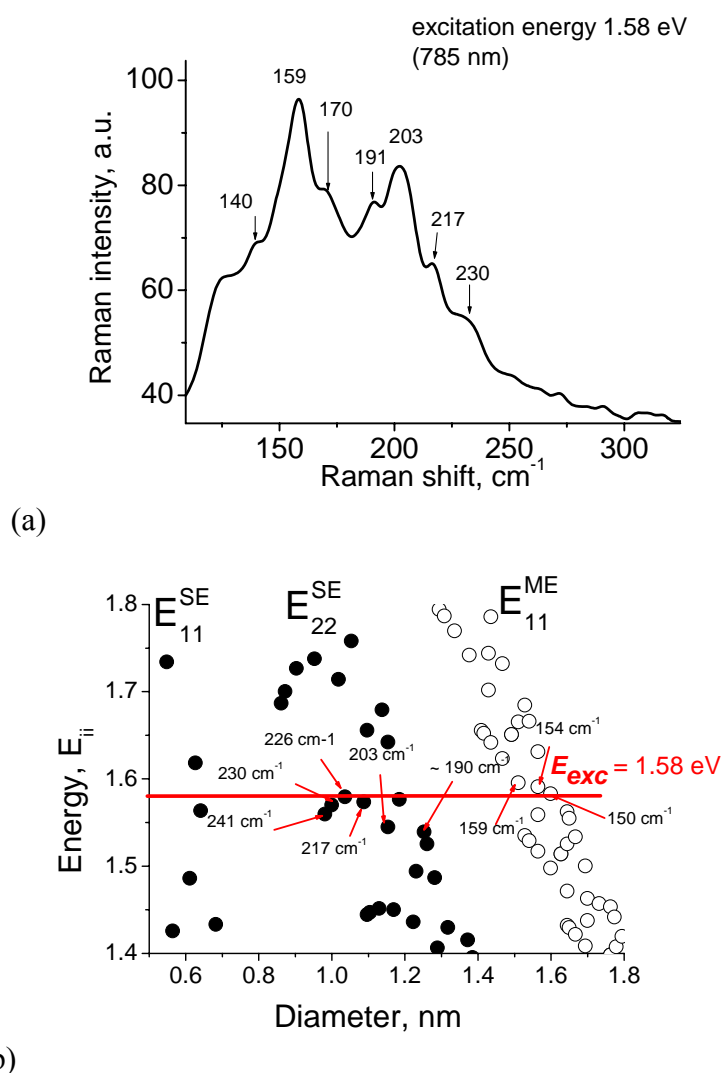


**Figure 4.6** (a) Raman spectra obtained from the dispersions of *HipCo*-NTs in  $\text{D}_2\text{O}/\text{SDS}$  (for detail of the dispersion preparation see Section 5.2) at  $E_{\text{exc}} = 1.58$  eV; (b) the electronic transition energies vs. nanotube diameters calculated with semiempirical formulae (3.12) and (3.12') for the semiconducting CNTs (black dots) [6] and using the tight-binding model for the metallic CNTs (open dots); the horizontal line denotes the excitation energy  $E_{\text{exc}} = 1.58$  eV, the RBM frequencies of the tubes with energies close to  $E_{\text{exc}}$  are shown with arrows.

The data in Fig. 4.6 (b) are generated in two ways: using the semiempirical formulae (3.12) and (3.12') for the semiconducting nanotubes (black dots) [6] and the tight-binding model for the metallic nanotubes (open dots).

In conclusion, RBM is one of the most interesting features of Raman spectra of CNTs reflecting the resonant nature of Raman scattering and the effects of the electron-phonon coupling. RBM contains information about the nanotube intrinsic structure, as well as the influence of the external factors (such as temperature and interaction) on the electronic and vibrational properties of CNTs.

### D-mode

The D-mode at  $\approx 1350 \text{ cm}^{-1}$  (see Fig. 4.5, c) does not originate from the  $\Gamma$ -point Raman-active vibration. It was found first for the graphite and after a while for carbon nanotubes that the D-peak is induced by disorder [13]. Its position depends on the defect concentration, as well as on crystallite size and, what is most intriguing, on the excitation energy. That was an unexpected effect since the D-mode does not correspond to a cage vibration of carbon nanotube like, for example, RBM.

In the last few years a great breakthrough occurred in understanding of the D-mode origin. Reich *et al.* [13, 41, 42] proposed the double-resonance scenario caused by the defect-induced scattering process. In this scattering process the particular excitation energy selects a strictly particular phonon wavevector. Figure 4.7 schematically shows the double-resonance Raman scattering process.

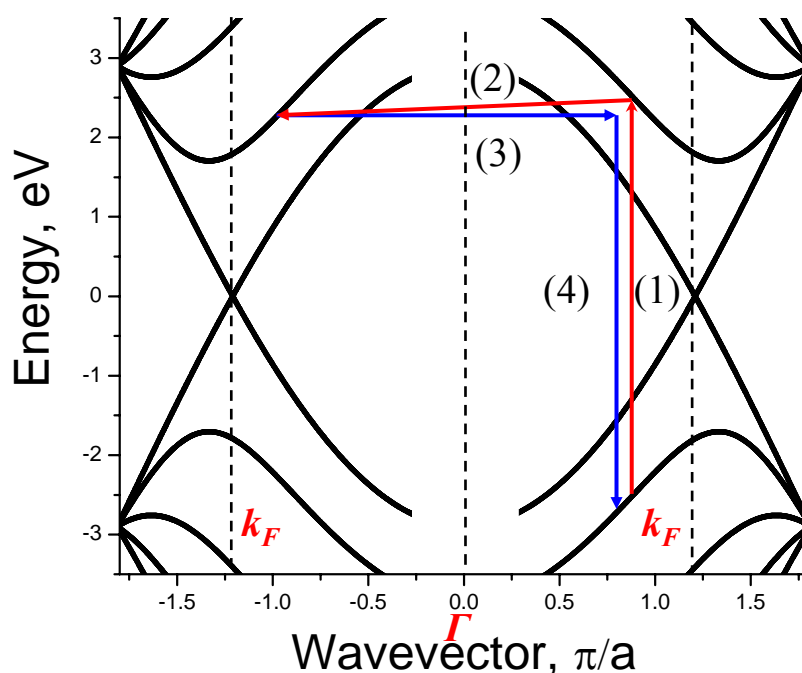


**Figure 4.7** Double-resonance Raman scattering process shown in four steps: (1) resonance excitation of an electron, (2) resonance scattering by a phonon across the  $\Gamma$ -point, (3) elastic scattering back by a defect, (4) an electron-hole recombination.

Here, the electronic band structure of the zig-zag (5, 5) tube is symmetric with respect to the  $\Gamma$ -point. The double-resonant Raman process occurs in four steps marked in Fig. 4.7 with numbers:

- (1) electron is excited resonantly (to the real electronic state) by a quantum of light;
- (2) electron is scattered resonantly by a phonon across the  $\Gamma$ -point;
- (3) electron is elastically (with no momentum change) scattered back by a defect (non-resonant process);

(4) electron recombines with a hole (non-resonant process).

A defect does not change the quasi-linear momentum  $\mu$ . The electronic resonance transition occurs close to the  $K$ -point ( $k_F = 2\pi/3a$ ), where the bands cross or have minima. A double-resonance condition is fulfilled only for the case of scattering across the  $\Gamma$ -point to the same band. The double-resonance wave vector is then  $q_0 \approx 4\pi/3a$  (twice of the  $k_F$  distance). But the positions of the band minima are not exactly at the  $K$ -points, and the higher dispersion the bigger distance from its minimum to the  $k_F = 2\pi/3a$  (see Fig. 4.7).

Now if the incoming laser energy increases, the resonant optical transition between the dispersion minima occurs at larger distance from  $k_F$  and with larger value  $q_0 > 4\pi/3a$ . Therefore, the higher the excitation laser energy, the larger the phonon wavevector, and the larger the D-mode frequency in the Raman spectrum.

In summary, the most prominent properties of the D-mode are the following:

- D-mode is caused by the scattering by defects, and its intensity in general is proportional to the number of defects, but also depends on the excitation energy;
- D-mode is theoretically predicted to exist only for the metallic tubes [13], however, it is also observed for both metallic and semiconducting tubes in mixed samples;
- D-mode is not symmetrical and consists of two non-resolved peaks [13];
- shift of these two peaks with  $E_{\text{exc}}$  is measured to be  $\approx 42$  and  $76 \text{ cm}^{-1}/\text{eV}$ .
- number of defects can be estimated from the intensity ratio  $I(D)/I(D^*)$ , where  $I(D)$  and  $I(D^*)$  are the intensities of the peaks D and  $D^*$  because the intensity of the  $D^*$  does not depend on the excitation energy.

### **HEM (G-mode)**

The High Energy Mode (HEM) is the most intense and prominent peak in the Raman spectra of CNTs (Fig. 4.5, c). It corresponds to the graphite optical mode appearing at  $1580 \text{ cm}^{-1}$  (sometimes it is called Graphite-like G-mode) where carbon atoms vibrate tangentially to the nanotube wall. The curvature of the tube's walls introduces a small softening of the in-plane force constants compared to the graphene sheet and leads a slight diameter-dependence of the phonon frequencies [37].

The HEM consists of two optical modes with  $E_{2g}$ -symmetries: the longitudinal LO (at about  $1570 \text{ cm}^{-1}$ , with  $\text{FWHM} \approx 30 \text{ cm}^{-1}$ ) and the transverse TO ( $\approx 1592 \text{ cm}^{-1}$ ,  $\text{FWHM} \approx 16 \text{ cm}^{-1}$ ) vibrations of a tube. In contrast to the graphite peak at about  $1580 \text{ cm}^{-1}$  which does not depend on the excitation, the LO and TO modes of carbon nanotubes both slightly vary with the excitation energy [38]. This effect is usually attributed to a weak diameter dependence of the optical Raman-active modes [44].

The general dependence of the Raman intensities on the laser excitation energy is discussed in Section 4.2. The Raman intensity and the peak position are both determined by the phonon energy  $E_{\text{ph}}$  as well as the energy of the electronic transition  $E_{\mu}$ . Since the electronic transition energies  $E_{\mu}$  are individual for each kind of tubes, the form of the HEM peak in the Raman spectrum must depend on the excitation energy.

In Fig. 4.8 the RBM and the HEM of two samples with different sets of tubes are presented: the *HipCo* - tubes with the diameter distribution [0.8 – 1.3 nm] (Figs. 4.8 a,b), and the *NiCo* - tubes with the diameter distribution [1.3 – 2 nm] (Figs. 4.8 c,d). The spectra were obtained for the same laser excitation energy  $E_{\text{exc}} = 2.3 \text{ eV}$ .

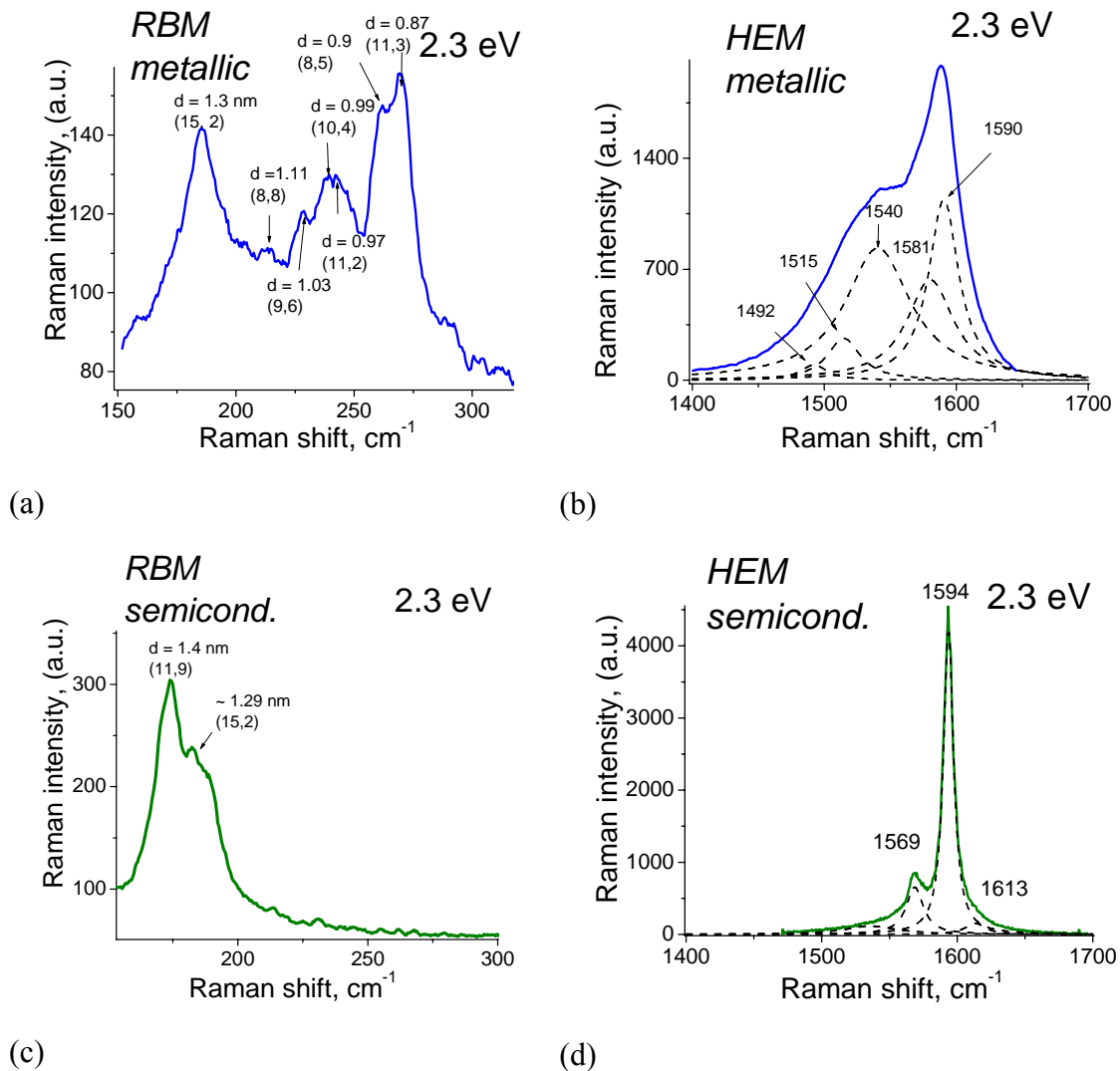


**Figure 4.8.** Parts of the Raman spectra of semiconducting and metallic CNTs (obtained at  $E_{\text{exc}} = 2.3$  eV): (a, b) RBM and HEM of metallic CNTs; (c, d) RBM and HEM of semiconducting CNTs. The HEM peaks are fitted with Lorentzians.

For the *HipCo*-tubes with smaller diameters mostly metallic tubes from the  $E_{11}^{\text{ME}}$  branch come into the resonance at this excitation energy (see Fig. 3.9). In contrast, for the *NiCo*-tubes with larger diameters only semiconducting tubes  $E_{33}^{\text{SE}}$  and  $E_{44}^{\text{SE}}$  are excited and their RBM peaks are seen in the spectra. Therefore, by varying either the excitation energy or tube diameters in different samples one can selectively excite either metallic (Fig. 4.8, a, b) or semiconducting tubes (Fig. 4.8, c, d).

A typical semiconducting HEM (Fig 4.8, d) consists of three lines at about 1569, 1594, and 1613  $\text{cm}^{-1}$  (Lorentzian fitting). A typical metallic HEM (Fig 4.8 b) is much broader and has additional components (at  $\approx 1515$ , 1540 and 1581  $\text{cm}^{-1}$ ).

An alternative explanation of the dependence of HEM on the excitation energy based on the defect-induced double-resonance process was proposed by Reich *et al.* [13]. Following this consideration, the Raman frequency of HEM changes not because *different tubes* are excited, but instead, due to different phonons excited for the *same tube* in a double-resonant scattering process. In contrast to the D-mode, where an excited electron is scattered by a defect, in the case of HEM an electron is scattered by a phonon with relatively small momentum across the conduction-band minimum [13].

Since HEM reflects a tangential C-C bond stretching vibration, it should also depend on pressure and temperature since the force constants between the atoms in the tube cage also changes [13, 38].

In summary, the position and the shape of HEM are found to be dependent on the electronic transition energies, laser excitation energy, tube diameters and also on temperature and pressure.

#### *D\* - mode and Intermediate frequencies*

The strongest peak in the second order Raman spectrum is the overtone of the D-mode at  $\approx 2700 \text{ cm}^{-1}$  which is called  $D^*$ - or  $G^*$ -mode because of the combination of the D and HEM frequencies. The  $D^*$ -mode does not depend on the excitation or defects. Therefore, the intensity ratio  $I(D)/I(D^*)$  can be used for calibration of the defect concentration [13, 103].

The intermediate frequencies between  $600$  and  $1100 \text{ cm}^{-1}$  appear due to the combination of the optical and acoustic modes and strongly depend on the excitation [106].

### 4.4 Experimental Raman set-up

The Raman set-up used in this work is schematically presented in Fig. 4.13.

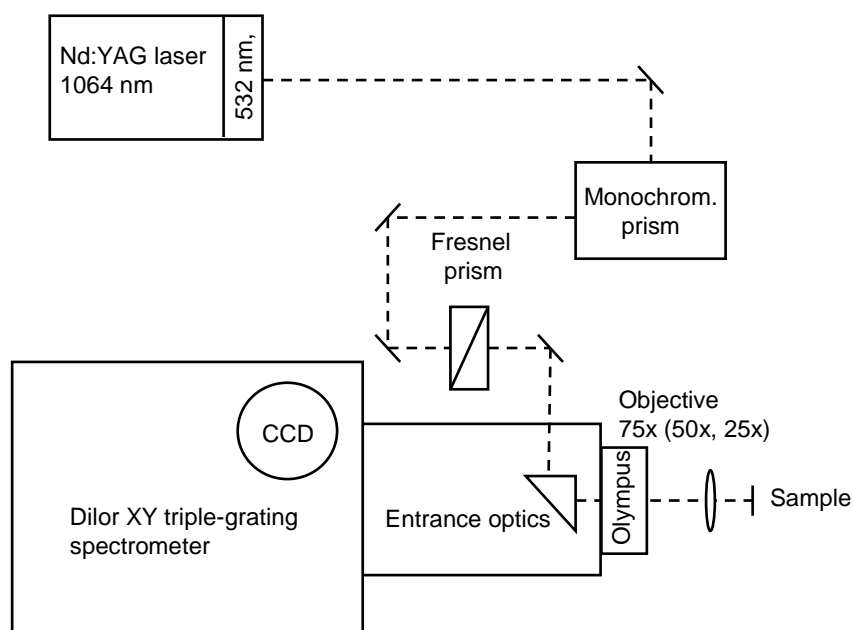


**Figure 4.13** Experimental Raman set-up consisting of the Dilor XY (800) triple-grating spectrometer, Olympus confocal microscope and Nd:YAG laser ( $\lambda_{\text{exc}} = 532 \text{ nm}, 1064 \text{ nm}$ ).

It consists of a standard Dilor XY (800) triple-grating spectrometer equipped with an Olympus optical confocal microscope. The spectrometer suppresses the elastic Rayleigh scattering and disperses the Raman spectrum. Spectra are collected with a multi-channel charge-coupled detector (CCD) cooled with liquid nitrogen. The set-up is optimized for recording of the weak signals in a vicinity of the Rayleigh peaks

using a notch filter. The intensity of the Stokes scattering is  $\approx 10^3$  weaker than the intensity of the Rayleigh scattering.

The laser light first passes a prism monochromator to remove the plasma lines of the laser. Then it is focused onto the sample, using one of the objectives (75x, 50x or 25x). The scattered light is collected in backscattering geometry. The spectrometer works in a subtractive mode to suppress the elastically scattered Rayleigh light with the help of two first gratings placed in a way to create a narrow band pass filter of variable wavelength. The line is dispersed by the last grating and collected by a CCD camera. The resolution for the green light was about  $3 \text{ cm}^{-1}$  what is smaller than the minimum width of the Raman peaks ( $10 - 15 \text{ cm}^{-1}$ ) observed in carbon nanotubes.

The scattering is excited by Nd:YAG diode-pumped solid state laser generating the wavelength 1064 nm and operating at the output power  $\approx 90 \text{ mW}$ . The wavelength 532 nm is obtained due to the frequency-doubling. The total power of the laser beam irradiating the sample is about 1 – 5 mW. The beam can be focused in a spot of different sizes using one of the objectives with magnification 75x, 50x and 25x. The minimum diameter of a spot  $\approx 1 \mu\text{m}$  was obtained with the objective 75x. The density of the laser power depending on the laser spot diameter, however, is a critical parameter in the investigation of carbon and  $\text{B}_x\text{N}_y\text{C}_z$ -nanotubes since these materials are unstable against prolonged and intensive irradiation. The stability of the samples depends on the material density, thermal conductivity and the element composition. A density of the laser power, less than  $10^9 \text{ W/m}^2$  (corresponding to 1 mW for the objective 75x), caused no thermal damage in any of the investigated materials.

## 4.5 Summary

In this chapter the basics of the resonance Raman scattering for CNTs were considered. A unique 1D structure of CNTs gives rise to a highly resonant Raman scattering process which characterizes their electronic DOS. The intensities of the Raman spectra depend on the difference between the electronic transition energy  $E_\mu$  of a tube and the laser excitation energy  $E_{\text{exc}}$ . Therefore, the electronic energies of CNTs can be studied analysing the resonance Raman intensities. The expression for the Raman intensity of a nanotube ( $n, m$ ) with a certain electronic transition energy  $E_\mu$  as a function of the laser excitation energy is also derived. This expression will be used in the theoretical analysis of the experimental data in *Chapters 5 and 6*.

# Chapter 5

## Bundling Effects

In *Chapter 5* the experimental and the theoretical study of the influence of tube-tube interaction (bundling effects) on the electronic properties of carbon nanotubes will be discussed. *Chapter 5* has the following structure:

- Motivation with analysis of the theoretically predicted changes in the electronic band structure of CNTs; manifestation of the bundling effects in Raman and photoluminescence experiments.
- Preparation of nanotube samples with different degree of bundling for the Raman experiment.
- Raman scattering experiments on single and bundled CNTs; comparison between their spectra and general conclusion about the change in the electronic band structure caused by the tube-tube interaction.
- Presentation of the theoretical model for the calculation of the resonance Raman intensities of CNTs as a function of the electronic energy change caused by different degree of the nanotube bundling.
- Comparison between the theoretical Raman intensities of CNTs and the experimental data obtained for the nanotube samples with different degree of bundling.
- Estimation of the *experimental* correlation between the nanotube bundle size (from the high resolution transmission microscopy images) and the experimental Raman intensities from those bundles.
- Finally, estimation of the *semi-empirical* correlation between the experimentally obtained nanotube bundle sizes and the theoretically calculated electronic energy shifts corresponding to those bundle sizes.

### 5.1 Motivation

Single-walled carbon nanotubes produced by laser vaporization using Ni and Co catalytic particles (*NiCo*-tubes) [57 – 60] or tubes grown in a process of high pressure catalytic decomposition of carbon monoxide CO (*HipCo*-tubes) [55, 56] are usually assembled in bundles of 20 – 100 tubes. Figure 5.1 shows a high resolution transmission electron microscopy (HRTEM) image of a typical bundle of the *NiCo*-carbon nanotubes.

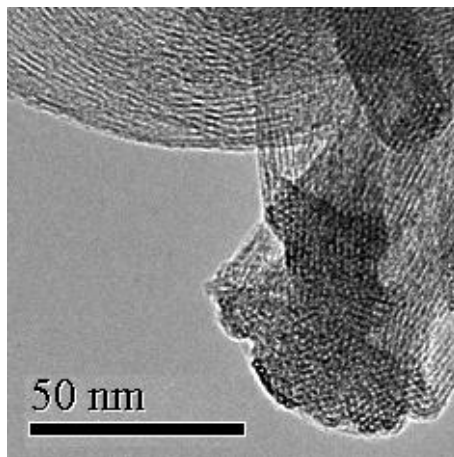


**Figure 5.1** HRTEM image of a typical carbon nanotube bundle containing hundreds of tightly packed nanotubes (NiCo-sample). This image and all the following HRTEM images were taken by P. Schweiss (IFP, Forschungszentrum Karlsruhe).

The tubes are held together by weak van-der-Waals forces. The bundles can be broken up by ultrasonication in aqueous solution with addition of surfactant. In this way a dispersion of isolated tubes with molecules of surfactant covering the tubes and protecting them from re-bundling can be prepared. An efficient method of creating the stable solutions of individualized SWNTs, which practically do not interact with each other, has been widely described in literature [6, 15, 18, 39] since the pioneering work of O’Connell *et al.* [17] was published. All previous research was performed on bundles containing nanotubes with different chiralities and diameters.

It was shown theoretically [46 – 51] and later on experimentally [18, 52 – 54] that bundling can strongly influence the nanotube properties. Following theoretical calculations, the tube-tube interaction manifests itself in:

- lowering the tube symmetry (the armchair (10, 10) tube, e.g. loses its mirror planes and changes its symmetry from  $D_{20h}$  to  $D_{6h}$  when bundled [48]);
- opening of an additional pseudo-gap with a size of approximately 200 meV in bundled metallic armchair nanotubes [53];
- appearance of an additional dispersion of 100 – 200 meV perpendicular to the  $k_z$ -axis [46];
- closing of the direct band gap in semiconducting tubes and opening of the indirect gap ( $\Gamma$ -K point transitions) smaller by 200 – 600 meV [46], appearance of metallic properties;
- broadening of the van Hove singularities [46];
- appearance of the additional peaks in van Hove singularities because of the splitting of doubly degenerate energy bands [51].

On the other hand, there are no significant changes registered so far in vibrational properties. The RBM frequency position is quite stable and does not depend on bundling effects [52].

The following section is focused on interesting effects caused by bundling in experiments carried out at the very beginning of this work. A more detailed explanation follows in the next sections.

First we found that the *fine structure* of the Near Infrared-visual-Ultraviolet (NIR-vis-UV) absorption signal appears only when tubes become individualized (single) or

assembled in very small bundles with reduced interaction, and disappears during the re-bundling processes in non-stabilized solutions [39, 45]. Fig. 5.2 shows the NIR-vis-UV absorption spectra of CNT samples with different degree of bundling.

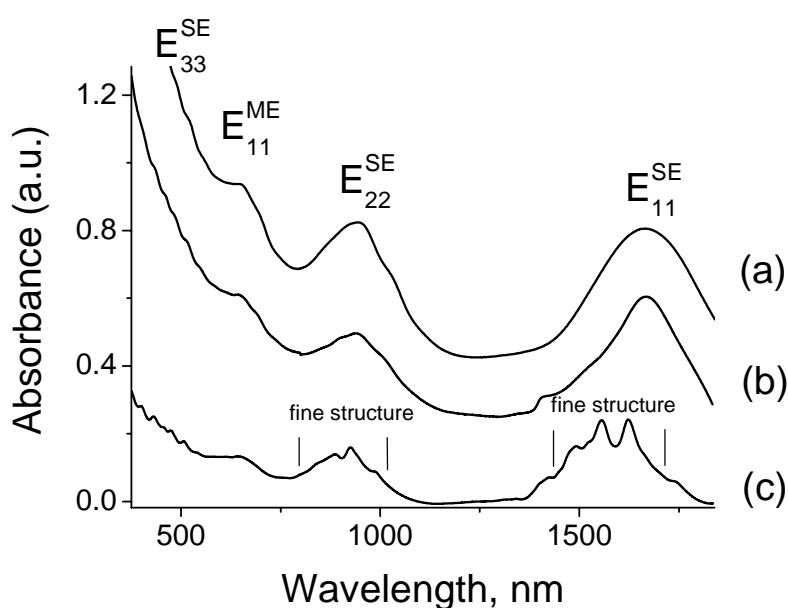


**Figure 5.2** NIR-vis-UV absorption spectra of CNTs with different degree of bundling: (a) strong interaction in a thin film, (b) reduced interaction in the  $D_2O/SDBS$  dispersion (for detail of the dispersion preparation see Section 5.2) centrifuged at 20 000 g, (c) low interaction in the  $D_2O/SDBS$  dispersion centrifuged at 180 000 g [39]. Spectra were taken by S. Lebedkin (INT, Forschungszentrum Karlsruhe).

The curve (a) shows the light absorption of a thin film of pressed and strongly interacting CNTs. The broad bands  $E_{11}^{SE}$ ,  $E_{22}^{SE}$ ,  $E_{33}^{SE}$  and  $E_{11}^{ME}$  corresponding to the interband electronic transitions (Fig. 3.9) of an ensemble of interacting tubes do not show fine structure because of the smearing out of the individual peaks.

The curve (b) was obtained from CNTs dispersed in  $D_2O/SDBS$  at moderate ultrasonic power and centrifuged at 20 000 g. The dispersion contains bundles of nanotubes and does not show any distinct peaks either. In the curve (c), obtained from the same solution which was dispersed at high ultrasonic power and centrifuged at 180 000 g, one can see, however, the fine structure. These sharp peaks correspond to the individual electronic transitions of single nanotubes.

The influence of bundling on Raman spectra is even more intriguing. Fig. 5.3 shows the low-frequency Raman spectra of *NiCo*-nanotubes dispersed in  $D_2O$  with addition of sodium cholate.

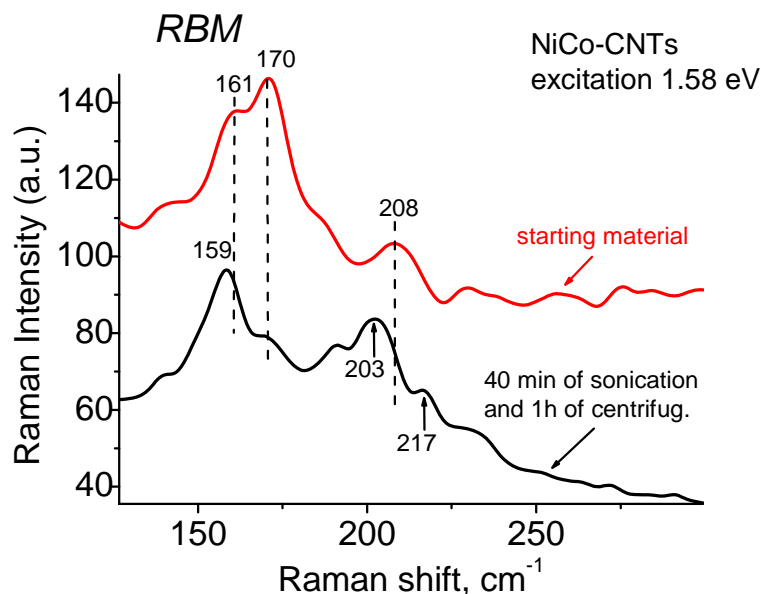


**Figure 5.3** Low frequency Raman spectra obtained from dispersions of CNTs in  $D_2O/NaCholate$  ( $E_{exc} = 1.58$  eV). The upper curve is for the dispersion before sonication containing big bundles of CNTs, the lower curve is for the sonicated and centrifuged dispersion with many individual CNTs. Spectra were taken by F. Hennrich (INT, Forschungszentrum Karlsruhe).

The upper curve is obtained from the starting material (before sonication), containing CNT-bundles of different sizes. The dispersion after sonication (lower curve) contains the same set of nanotubes as the starting material had, but in an isolated state. One can see that some peaks ( $208\text{ cm}^{-1}$  and  $170\text{ cm}^{-1}$ ) lose their intensity, while others ( $159\text{ cm}^{-1}$ ,  $203\text{ cm}^{-1}$  and  $217\text{ cm}^{-1}$ ) appear after the de-bundling process.

The next interesting phenomenon was an amazing difference between the Raman spectra obtained from two very close regions of the nanotube solid sample. Fig. 5.4 presents the high-resolution transmission electron microscopy (HRTEM) image obtained from the film ( $\approx 50\text{ }\mu\text{m}$ ) of tightly pressed *NiCo*-CNTs (so-called *bucky paper*) with the black (opaque for electrons) central part and the bundles ( $\approx 20\text{-}50\text{ nm}$  thick) well seen along the edge region of the particle.

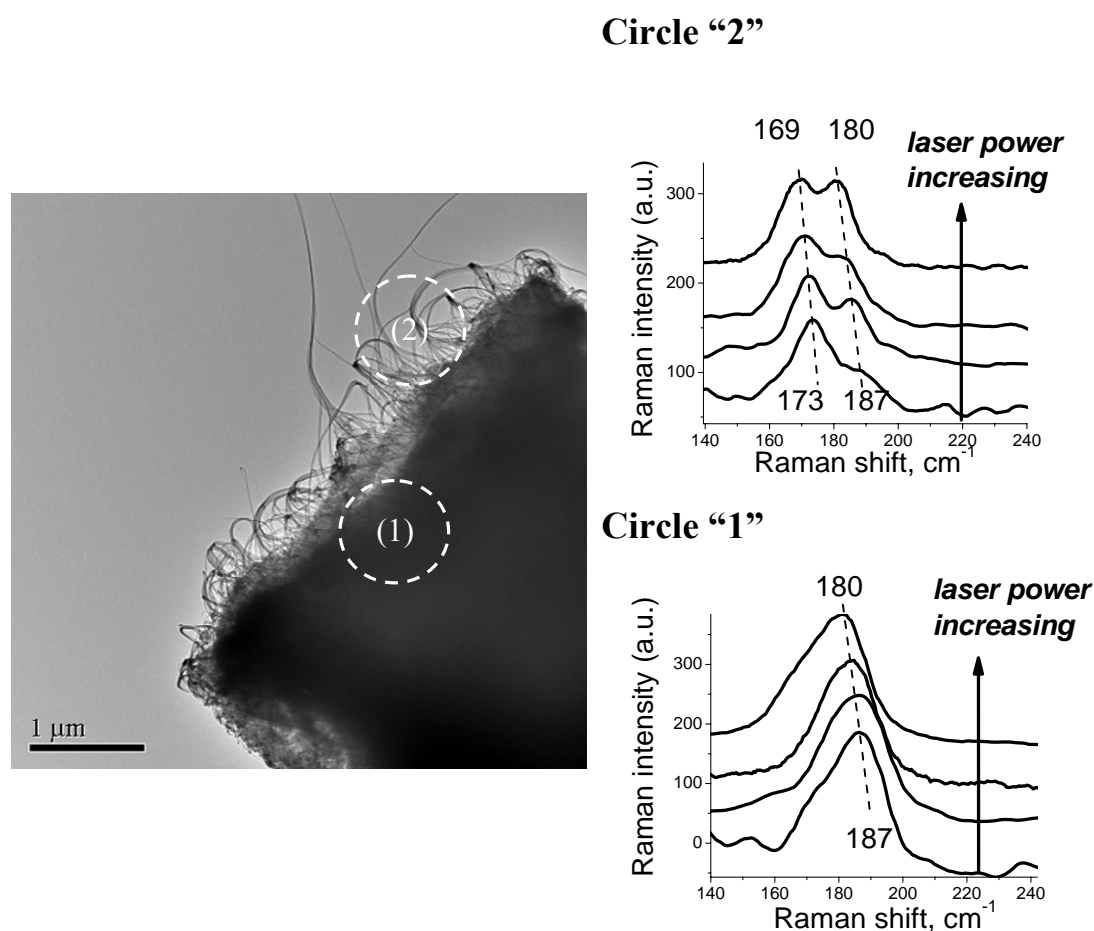


**Figure 5.4** HRTEM image of the *NiCo*-sample and low frequency Raman spectra ( $\lambda_{\text{exc}} = 2.3 \text{ eV}$ ) from different parts of it: strongly interacting tightly pressed CNTs (circle “1” in the HRTEM image) and bundles of tubes  $\approx 50 \text{ nm}$  (circle “2” in the HRTEM image). The circles indicate the laser beam size and its position.

The low frequency Raman spectra (RBM) obtained from the dense material (circle marked as “1”) were identical in any point of the sample and in other similar samples. The set of spectra presented on the right side is shown for increasing laser power (i.e. temperature). In the case of dense material “1” only a thermal shift in the RBM peak position ( $187 \text{ cm}^{-1}$  to  $180 \text{ cm}^{-1}$ ) was observed with increasing laser power, and no other obvious changes.

The edge region with bundles and comparatively reduced tube-tube interaction (circle marked as “2”), on the contrary, demonstrates completely different Raman spectra (upper right panel). The component at  $173 \text{ cm}^{-1}$  dominates at low laser power. With increase of the laser power the RBM peak changes its shape. Thus, growing of the component  $187 \text{ cm}^{-1}$  with respect to  $173 \text{ cm}^{-1}$  together with thermal shifts ( $187 \text{ cm}^{-1}$  to  $180 \text{ cm}^{-1}$  and  $173 \text{ cm}^{-1}$  to  $169 \text{ cm}^{-1}$ ) was observed. The only difference between the areas “1” and “2” is the degree of nanotube interaction (bundling), which changes their electronic properties.

In the following, the effects of bundling are studied in more detail taking into account the theoretical predictions of the influence of the intertube interaction on the electronic properties and using the resonance Raman technique.

## 5.2 Sample preparation

In order to study bundling effects one would ideally use several samples containing (1) strongly bundled nanotubes, (2) fully isolated nanotubes, and finally, (3) intermediate samples with bundles of different sizes. It would be a great experimental success to obtain the samples consisting of bundles of equal sizes to study them with routine Raman scattering or with PL in dispersions. In reality, however, most samples have a distribution of bundles, with the mean bundle size depending on the preparation procedure. Therefore, a Raman spectrum will reflect the average response from a mixture of nanotube bundles of different sizes. In this work the problem was partially solved by stabilizing single tubes and small bundles inside thin organic films on Si-substrates.

### *HipCo and NiCo – tubes in bundles*

In this work carbon nanotubes produced by two different methods were available: the *HipCo* – tubes prepared in a high-pressure decomposition of carbon monoxide CO method [55, 56] and the *NiCo* – produced by Pulse Laser Vaporization (PLV) method of carbon targets using Ni and Co particles as templates [57 – 60]. These two methods provide nanotubes covering a wide range of diameters from 0.8 to 1.5 nm (see Fig. 3.9): *HipCo*-tubes with a diameter distribution in the range of [0.8 – 1.2 nm], peaked at  $\approx 1$  nm, and *NiCo*-tubes with a narrow diameter distribution [1.2 – 1.5 nm] peaked at  $\approx 1.3$  nm.

The as-prepared *HipCo*- as well as *NiCo*- materials are powder-like substances of black appearance, containing admixtures of metals such as Ni, Co, and Fe, and up to 50% of single-walled CNTs (SWNTs) for *NiCo*- and up to 97% of SWNTs for *HipCo*- samples tightly packed in ropes. *NiCo*-materials contain a small amount of fullerenes, soot and other graphite-like materials.

### *Dispersions*

The dispersions were prepared with the assistance of F. Hennrich and S. Lebedkin (INT, Forschungszentrum Karlsruhe). For the preparation of individualized nanotubes few milligramms of as-prepared SWNTs are added to 1 ml of heavy water D<sub>2</sub>O (Aldrich Inc.) containing 0.1 – 0.3 mg/ml of the Sodium Cholate surfactant and dispersed with an ultrasonic tip for  $\approx 40$  min at  $\approx 100$  W/cm<sup>2</sup> power. This dispersion was centrifuged in a standard lab microcentrifuge for 1 hour at 100 000 g in order to remove large bundles and heavy metal catalyst particles. The typical final concentration of nanotubes was estimated to be about 20  $\mu$ g/ml. No aggregation and precipitation was observed over weeks.

In previous publications [6, 17, 18, 39, 52] routinely sodium dodecylsulfate cationic surfactant (SDS) and the Tween-80 surfactant were reported to have been used. Tween-80 was even preferred over SDS for the PL experiments [39] because of the very low ‘working’ concentration (critical micelle concentration CMC  $\approx 13$   $\mu$ g/ml compared to 2.4 mg/ml for SDS) and, consequently, a negligible NIR absorption. In this experiment, Sodium Cholate was used in order to improve the dispersion characteristics (increase the number of micelle-individualized tubes). The tubes in the dispersions are mostly individualized with a small residual of bundled tubes.

### *CNTs deposited on Si-wafers*

Concerning the separation of CNTs, a great success was achieved by R. Krupke *et al.* in the development of a method of selective deposition of metallic tubes using alternating current dielectrophoresis [15]. This method results in well-aligned single metallic tubes deposited between gold electrodes leaving semiconducting tubes in the dispersion. The elaboration of an efficient method of deposition from the dispersion of both isolated metallic and semiconducting nanotubes still remains an unsolved problem.

The nanotubes isolated inside the micelles of surfactant in dispersions are quite stable molecular complexes, which do not show any precipitation over weeks [39]. If one adds to the dispersion a pure solution with some surfactant, the chemical equilibrium in the system will be destroyed, resulting in re-bundling processes and tube sedimentation. Similar re-bundling of tubes sticking together can be observed in a drop of dispersion on a surface. Fig. 5.5 shows a scanning electron microscopy (SEM) image of such a drop of the dispersion of *NiCo*-nanotubes in  $D_2O/NaCholate$  dried out on the rotating silica surface (spin-casting method). The samples produced by the spin-casting on Si-wafers were prepared together with F. Hennrich (INT, Forschungszentrum Karlsruhe).

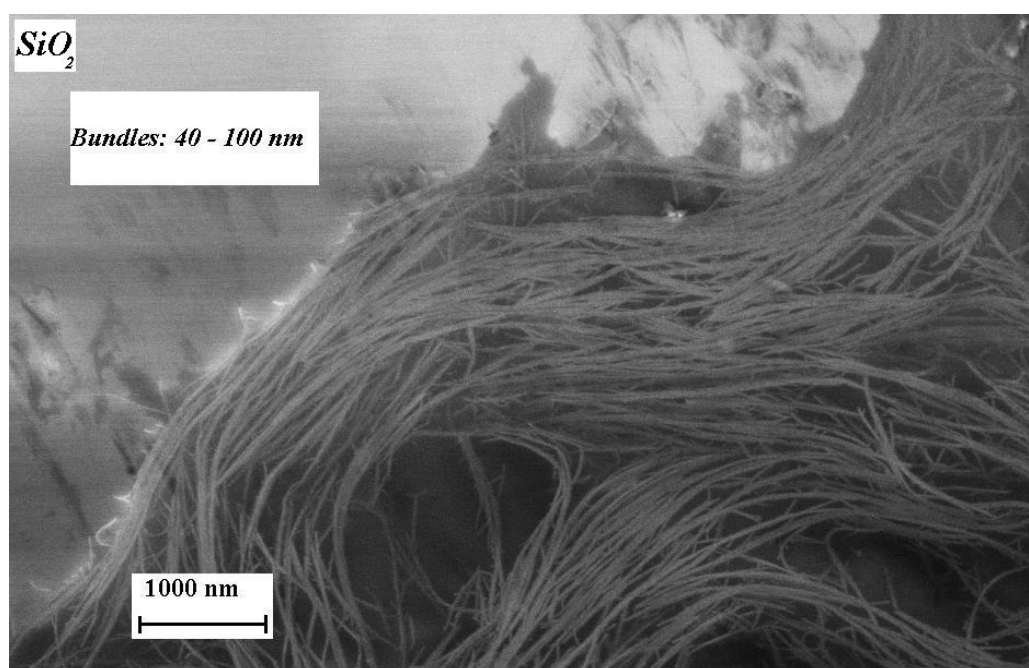


**Figure 5.5.** SEM image of a drop of the dispersion of *NiCo*-tubes in  $D_2O/NaCholate$  dried out on the Si-wafer. This image and all the following SEM images were taken by S. Malik (INT, Forschungszentrum Karlsruhe).

The tubes had been individualized in the dispersion as demonstrated by their PL and Raman spectra. They form on the Si-surface large and long bundles covered with molecules of surfactant. The spin-casting method does not efficiently prevent tubes from re-bundling, and such a sample brings no additional information about bundling compared to the sample in Fig. 5.4.

The sizes of bundles within the  $1\mu m$ -area (laser beam size) are quite large and inhomogeneous (40 – 100 nm thick), and the Raman signal varies from point to point, making the estimation of the correlation between the bundle size and the Raman spectrum impossible.

In the next step, which gave a surprisingly interesting result, the Si-wafer was heated up to  $\approx 100^{\circ}\text{C}$ . The thin film of the surfactant with nanotube bundles inside developed cracks of about  $1\mu\text{m}$  due to the thermal expansion of the Si-wafer (Fig. 5.6).

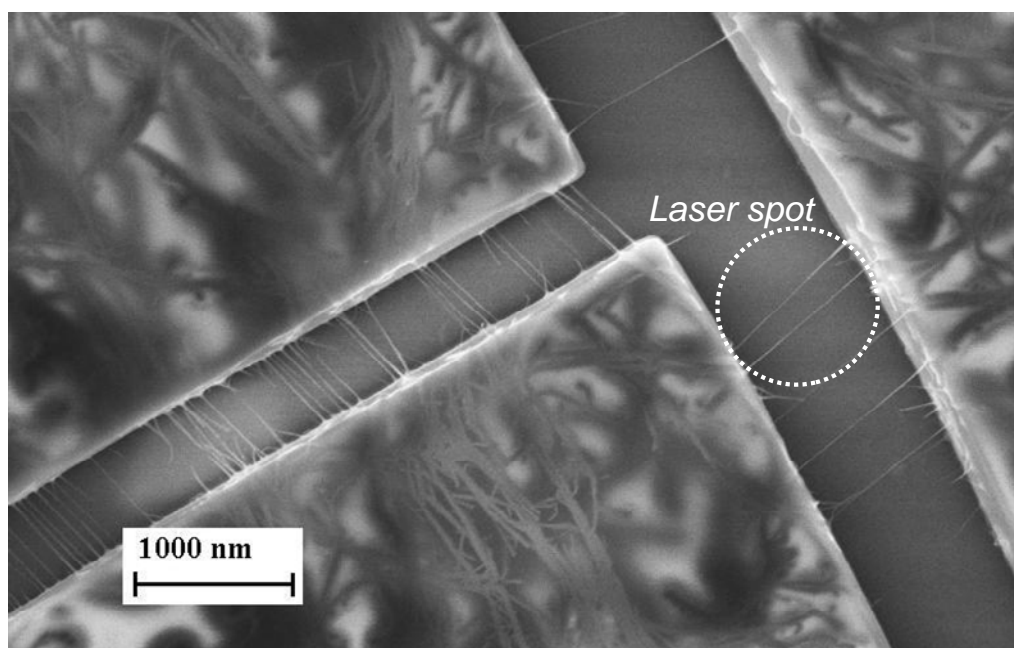


**Figure 5.6** SEM image of the surfactant film (NaCholate) deposited on the Si-wafer with *NiCo*-nanotubes coming out of the cracks. The small bundles ( $\approx 10\text{ nm}$ ) and single tubes appeared between cracks in the film after heating of the Si-wafer up to  $100^{\circ}\text{C}$ .

The nanotube bundles coming out of the cracks appear to be quite well aligned, thin ( $\approx 10\text{ nm}$ ), homogeneous in their sizes (see enlarged picture in Fig. 5.7), and containing only few tubes.

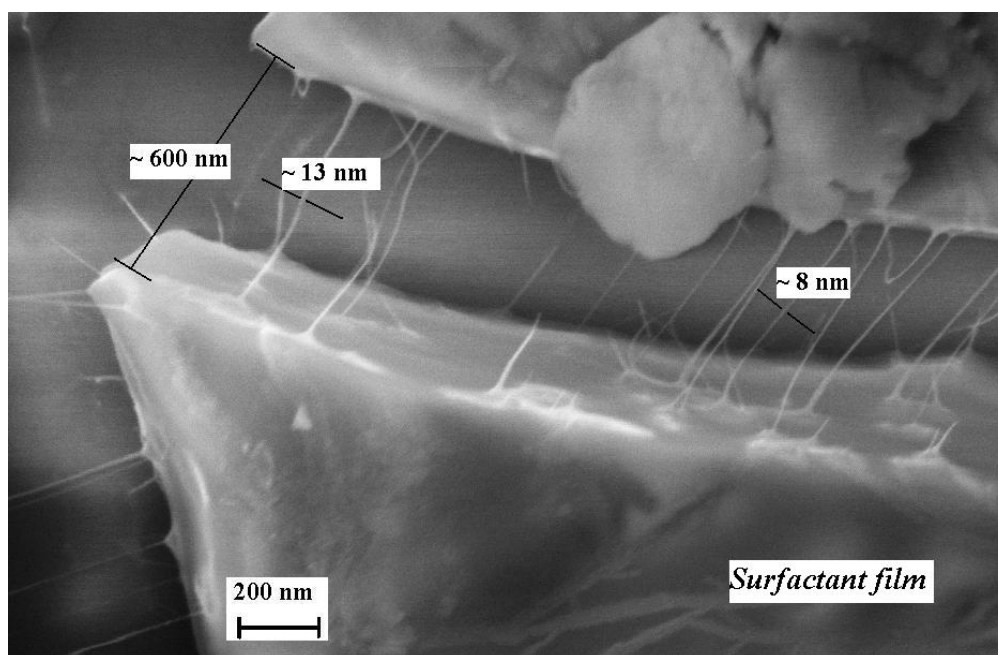


**Figure 5.7** An enlarged SEM image of the partially aligned *NiCo*-nanotubes crossing the crack in the surfactant film.

The main advantage of these samples is the possibility to study separate bundles or very few bundles by scanning the cracks with the laser beam which can be focused into a spot of about 1  $\mu\text{m}$ . In Fig. 5.6 the laser beam spot is shown as a dotted circle of 1  $\mu\text{m}$ . For that particular area only two bundles of about 10 nm thick are ‘trapped’ within the laser spot. Therefore, their Raman spectra can be related to their bundle size of 10 nm. The maximum resolution of the Raman microscope (objective 75x) is 0.5  $\mu\text{m}$ . The crossing cracks are thus well-distinguished. In these string-like samples the nanotube areas previously studied with SEM can be easily found again with an optical microscope. Therefore, the relation between the Raman spectra and the bundle sizes can be obtained with a high precision.

The samples were stable up to temperatures of 150<sup>0</sup>C, and up to powers of 5 mW of the Raman laser beam. Further heating increases the cracks and, upon reaching a certain value destroys such a string-like structure. The samples remain unchanged over days and sometimes weeks, depending on the storage conditions. A somewhat similar picture was observed for dispersions of *HipCo*-tubes in D<sub>2</sub>O/NaCholate which were dried out on standard gold grids for HRTEM microscopy (Fig. 5.8 *a*, and *b* enlarged).

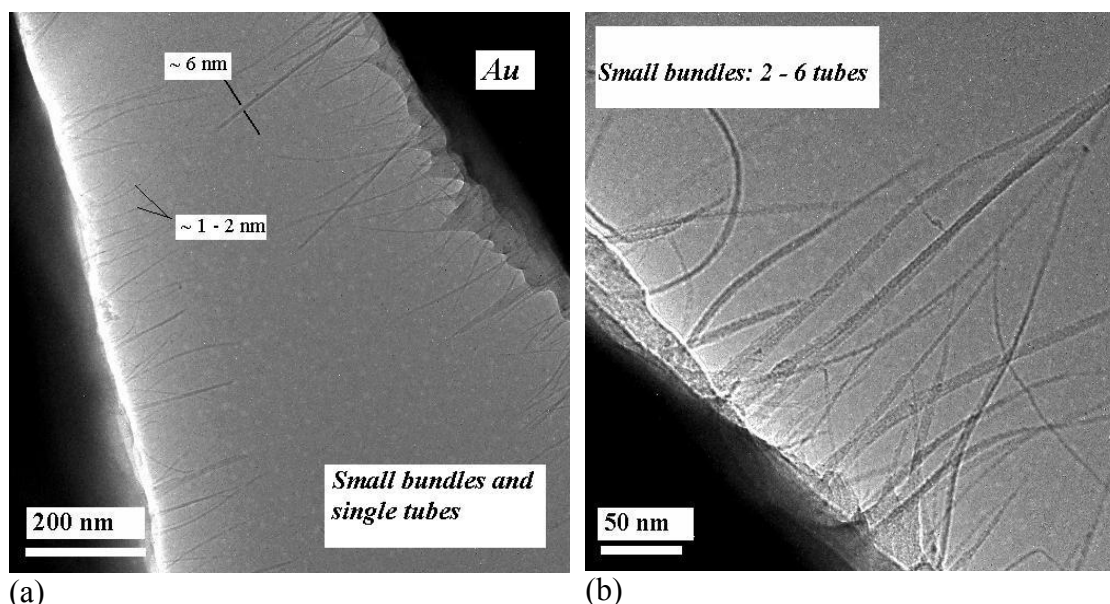


**Figure 5.8.** HRTEM images of the *HipCo*-tubes dispersed in D<sub>2</sub>O/NaCholate and dried out on an Au-grid.

The open cracks appear without heating due to the surface tension in the surfactant film. These samples were less stable against laser power heating than those on the Si-wafer. Moreover the films strained between the square holes of the gold grid (with a size  $\approx$  80  $\mu\text{m}$ ) decompose within hours.

### 5.3 Experimental results

#### *Resonance Raman scattering*

In order to understand the general tendencies of bundling effects the study was started with solid samples of strongly bundled tubes. Then the nanotubes were individualized

in dispersions. The resonance Raman spectra of strongly bundled tubes and “individual” ones in the dispersion are compared in Fig. 5.9. The comparison is presented for the *HipCo*-tubes as having many electronic transitions ( $\approx 10$ ) close to the resonance with  $E_{\text{exc}} = 2.3$  eV, in contrast to *NiCo*-tubes with only two transitions (see Raman spectra in Fig. 5.4).

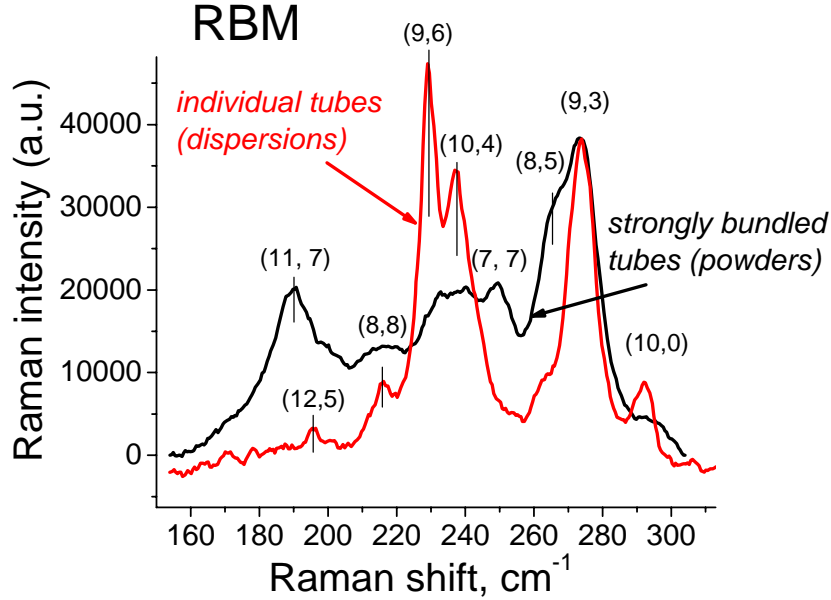


**Figure 5.9** Low frequency Raman spectra of *HipCo*-nanotubes ( $E_{\text{exc}} = 2.3$  eV): the strongly bundled tubes (powders) and individual tubes (dispersions). The  $(n, m)$  indices assignment was made using data from [18].

The spectra of strongly bundled and individual tubes in Fig. 5.9 have almost the same set of peaks (the same set of tubes) however, their relative intensities are different. Thus the *intensity difference* of the Raman peaks in spectra of single and bundled tubes is the most important manifestation of the bundling effects.

In order to assign the peaks one should look at Fig. 3.9 which shows the electronic transitions in resonance with  $E_{\text{exc}} = 2.3$  eV. The excitation energy  $E_{\text{exc}} = 2.3$  eV corresponds to electronic energies of *metallic* tubes for the *HipCo*-tubes. For metallic interband transitions semiempirical formulae connecting diameter and energies similar to semiconducting tubes [6] do not exist.

In this work an assignment based on the data from the resonance Raman experiment [18] was applied. Fantini *et al.* [18] managed to attribute the pairs of the experimental values  $\{E_{ii}, \omega_{\text{RBM}}\}$  obtained from the Raman spectra to  $(n, m)$  indices of metallic tubes comparing the TB model and the semiempirical formulae for semiconducting tubes [6]. They estimated the *down-shifts* of the electronic energies as well as broadening of the resonance windows for bundled tubes with respect to isolated ones.

According to Fantini *et al.* the values of the energy down-shift vary from 20 up to 140 meV for different tubes, and the width of the resonance Raman windows changes from the  $\Gamma = 60$  meV for micelles-isolated tubes up to  $\Gamma = 120$  meV for bundled tubes. Figure 5.10 presents the experimental energies  $E_{ii}$  from [18] plotted versus RBM frequencies for both bundled and single tubes together with their  $(n, m)$  indices.

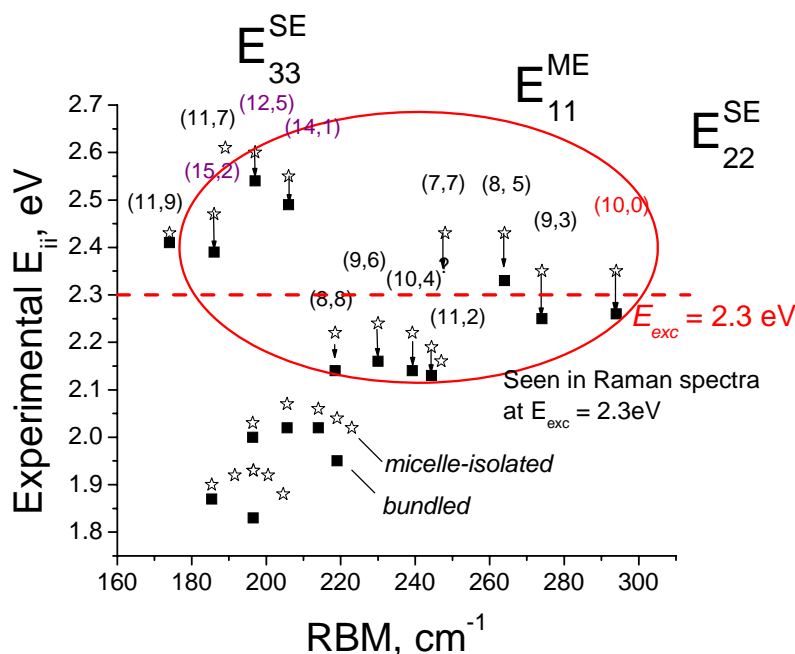


**Figure 5.10** Experimental transition energies  $E_{ii}$  of metallic and semiconducting *HipCo*-nanotubes plotted vs. their RBM frequencies: for micelle-isolated tubes (squares) and for bundled tubes (stars). Arrows show the energy *down-shifts* caused by bundling, for tube (7, 7) the “single” transition energy was not determined as well as “bundled” energy for (10, 0) tube (data from [18]).

The points in Fig. 5.10 are derived from the *maxima* of the resonance Raman windows (the Raman intensity vs. laser excitation energy, section 4.2) for each nanotube. Resonance windows have some width  $\Gamma$  (see eq. (4.16)), therefore the electronic transitions are possible within  $\Gamma$ . The intensity of the Raman peak for each tube is proportional to  $|E_{ii} - E_{exc}|$ : the smaller the difference, the larger the Raman peak intensity.

It can be seen from Fig. 5.10 that the transition energies of bundled tubes (marked with squares) are *red-shifted* (down-shifted) with respect to the micelle-isolated tubes (stars) for both semiconducting and metallic tubes. Fig. 5.10 explains, thus, the intensity changes in the Raman spectra shown in Fig. 5.9. The single tubes with transition energies *above* the laser excitation energy (dashed line in Fig. 5.10) move towards resonance with increasing of bundling. Their intensities grow, since the difference  $|E_{ii} - E_{exc}|$  decreases.

At the same time tubes with transition energies *below* the excitation energy move out of resonance in bundled state. Their intensities decrease, since the energy difference  $|E_{ii} - E_{exc}|$  increases. For instance, the Raman peaks of the tubes (11, 7), (12, 5), and (8, 5) have higher intensities in bundled samples than in dispersions (Fig. 5.9). On the contrary, the tubes (8, 8), (9, 6), and (10, 4) have higher Raman peaks in single state. The energy of the tube (9, 3) appears to be at the same distance from the  $E_{exc}$  in an isolated and bundled state, therefore, its Raman intensity should be similar in the single and the bundled state (Fig. 5.9). Fig. 5.10 gives an explanation of the difference in Raman intensities for bundled and single nanotube samples in Fig. 5.9. The parameters of the energy shifts are summarized in **Table 5.1**.

**Table 5.1** The parameters of single and bundled tubes (from [18]). ‘S-type’ means the “family” of the tube, or the Mod  $[(n - m), 3]$ . For tubes (11, 7), (12, 6), (14, 2), and some others the values  $E_{\text{bundled}}$  were not detectable.

RBM, $\text{cm}^{-1}$	$(n, m)$	$E_{\text{single}},$ eV	$E_{\text{bundled}},$ eV	Chiral angle, $\theta, ^\circ$	S- type	Diameter, nm	Metallic or semicond. transition $E_{ii}$
174	(11, 9)	<b>2.427</b>	<b>2.41</b>	26.7	2	1.38	$E_{33}^{\text{SE}}$
185.4	(11, 8)	1.9	1.87	24.8	0	1.29	$E_{11}^{\text{ME}}$
186	(15, 2)	<b>2.47</b>	<b>2.39</b>	6.2	1	1.29	$E_{33}^{\text{SE}}$
189	(11, 7)	2.61	–	22.7	1	1.27	$E_{33}^{\text{SE}}$
191.6	(12, 6)	1.92	–	19	0	1.25	$E_{11}^{\text{ME}}$
196.4	(9, 9)	2.03	2	30	0	1.22	$E_{11}^{\text{ME}}$
196.5	(13, 4)	1.93	1.83	13	0	1.21	$E_{11}^{\text{ME}}$
196.6	(13, 4)	1.93	–	13	0	1.21	$E_{11}^{\text{ME}}$
197	(12, 5)	2.6	2.54	16.6	1	1.21	$E_{33}^{\text{SE}}$
200.5	(14, 2)	1.92	–	6.6	0	1.19	$E_{11}^{\text{ME}}$
204.6	(15, 0)	1.88	–	0	0	1.16	$E_{11}^{\text{ME}}$
205.6	(10, 7)	2.07	2.02	24.2	0	1.16	$E_{11}^{\text{ME}}$
206	(14, 1)	2.55	2.49	3.4	1	1.16	$E_{33}^{\text{SE}}$
214	(11, 5)	2.06	2.02	17.8	0	1.11	$E_{11}^{\text{ME}}$
218.5	(8, 8)	2.22	2.14	30	0	1.09	$E_{11}^{\text{ME}}$
219	(12, 3)	2.04	1.95	10.9	0	1.08	$E_{11}^{\text{ME}}$
223	(13, 1)	2.02	–	3.7	0	1.06	$E_{11}^{\text{ME}}$
230	(9, 6)	2.24	2.16	23.4	0	1.03	$E_{11}^{\text{ME}}$
239.2	(10, 4)	2.22	2.15	16	0	0.99	$E_{11}^{\text{ME}}$
244.4	(11, 2)	2.19	2.13	8.2	0	0.96	$E_{11}^{\text{ME}}$
247	12, 0	2.16	–	0	0	0.95	$E_{11}^{\text{ME}}$
248	(7, 7)	2.43	–	30	0	0.95	$E_{11}^{\text{ME}}$
264	(8, 5)	2.43	2.33	22.4	0	0.89	$E_{11}^{\text{ME}}$
274	(9, 3)	2.35	2.25	13.9	0	0.85	$E_{11}^{\text{ME}}$
294	(10, 0)	2.36	2.26	0	1	0.79	$E_{22}^{\text{SE}}$

## 5.4 Data analysis

In the previous section the manifestation of the bundling effects in Raman spectra was illustrated as the intensity difference between the RBM peaks of bundled and single nanotubes. Bundling causes the *down-shift* of the electronic energy with respect to the single state for both metallic and semiconducting nanotubes. The increase/decrease of the intensities of the RBM peaks in bundled samples with respect to single ones depends on the position of the nanotube electronic energy  $E_{ii}$  with respect to the excitation energy (above/below).

Following Eq. (4.16) the Raman intensity depends on the difference  $|E_{ii} - E_{\text{exc}}|$ , where  $E_{ii}$  can be  $E_{\text{single}}$  (min bundling),  $E_{\text{bundled}}$  (max bundling) or an intermediate energy  $E_i$  corresponding to any degree of bundling between min and max. It would be convenient now to obtain a *numerical relation* for the Raman intensity as a function of the electronic energy change caused by bundling.

In order to solve this problem, the following section is devoted to the calculation of the Raman intensities of carbon nanotubes within the model described in Section 4.2 using Eq. (4.16). Experimental values of  $E_{\text{single}}$  and  $E_{\text{bundled}}$  from [18] are taken as the parameters.

#### 5.4.1 Raman intensities and electronic energy shift

In the following theoretical model introduced for the calculation of the Raman intensities as a function of electronic energy  $E$  ( $E_{\text{single}} \leq E \leq E_{\text{bundled}}$ ) two assumptions have been made:

- (i) nanotubes of different kinds in a sample undergo the *same interaction*, i.e. they are all in the same bundling state;
- (ii) the relative shift  $\alpha$  of electronic energies varies *synchronously* for all types of tubes. I.e. in the same environment the electronic energies of different nanotubes is described by

$$E(\alpha) = E_{\text{single}} - \alpha(E_{\text{single}} - E_{\text{bundled}}).$$

Here,  $\alpha$  is the “*degree of bundling*” which shows the relative energy shift (in %) with respect to single state and takes values from 0 to 100. In this way,  $E_{\text{single}}$  corresponds to  $\alpha = 0\%$ ,  $E_{\text{bundled}}$  to  $\alpha = 100\%$  of bundling.

Experimental parameters  $E_{\text{single}}$  and  $E_{\text{bundled}}$  are individual for different nanotubes [18] (see Table 5.1). In terms of the parameter  $\alpha$ , the relative energy shift for two tubes in the same bundling state will be the same, i.e.,  $\alpha_1 = \alpha_2$  (assumption (ii)).

The Raman intensities as a function of the electronic energy shift will be calculated using eq. (4.16), where the parameters are taken as follows:  $A = 1$ ,  $E_{\text{laser}} = E_{\text{exc}} = 2.3 \text{ eV}$ ,  $E_{\mu} = E_i(\alpha)$ , is a value of the individual electronic transition energy for each tube depending on the degree of bundling;  $E_{\text{ph}}$  is an individual phonon energy of the vibration, i.e. the value

$$\frac{\omega_{\text{RBM}} \text{ cm}^{-1} \cdot 0.001 \text{ eV}}{9 \text{ cm}^{-1}}.$$

The individual values  $\Gamma$  for different nanotubes were not given in [18]. Therefore, in this model the values of  $\Gamma$  were set to be *the same* for all nanotubes. The experimental widths of the resonance windows [18] also depend on the degree of bundling and were determined to be approximately:  $\Gamma_{\text{single}} = 60 \text{ meV}$  for single tubes and  $\Gamma_{\text{bundled}} = 120 \text{ meV}$  for bundled tubes. The parameters for the resonance window width  $\Gamma(\alpha)$  can be modelled analogically to  $E(\alpha)$  as:

$$\Gamma(\alpha) = \Gamma_{\text{single}} + \alpha(\Gamma_{\text{bundled}} - \Gamma_{\text{single}}).$$

Here, the degree of bundling  $\alpha$  shows the relative change of the width (in %) of the resonance window. In this model,  $\{E(\alpha), \Gamma(\alpha)\}$  change together with  $\alpha$ .

Fig. 5.11 presents the Raman intensities vs. the degree of bundling  $\alpha$  calculated as a function of  $\{E(\alpha), \Gamma(\alpha)\}$  using eq. (4.16) for 9 tubes seen in the experimental Raman spectra of *HipCo*-nanotubes (Fig. 5.9).

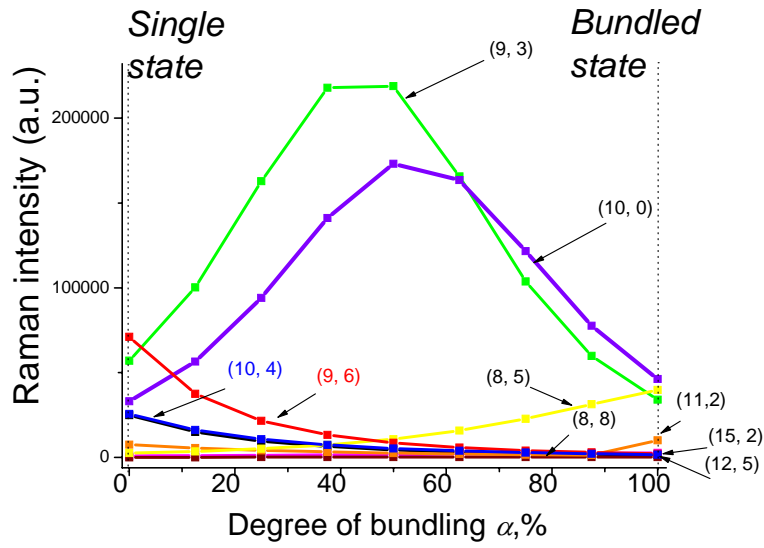


**Figure 5.11** Raman intensities plotted vs. the “degree of bundling”  $\alpha$ . The intensities of 9 tubes seen in the Raman spectra of *HipCo*-samples were calculated for  $\{E(\alpha), \Gamma(\alpha)\}$  using Eq. (4.16) (see text for details).

It should be noted, however, that as far as the individual values  $\Gamma$  for different nanotubes were not available this introduces an additional uncertainty to the Raman intensity estimation.

In order to determine how large this uncertainty can be the values  $\Gamma$  were varied in the following ranges: for single tubes  $\Gamma_{\text{single}} = [50 - 70 \text{ meV}]$  and for bundled tubes  $\Gamma_{\text{bundled}} = [110 - 130 \text{ meV}]$ . Then the Raman intensities were calculated as a function of  $\alpha$  (the same as in Fig. 5.12) but for *all possible* combinations of the varying  $\Gamma_{\text{single}}$  and  $\Gamma_{\text{bundled}}$  parameters. The result of the calculation is presented in Fig. 5.12 as vertically scattered dots around the intensity values calculated for the  $\Gamma_{\text{single}} = 60 \text{ meV}$  and  $\Gamma_{\text{bundled}} = 120 \text{ meV}$  (dots connected with lines).

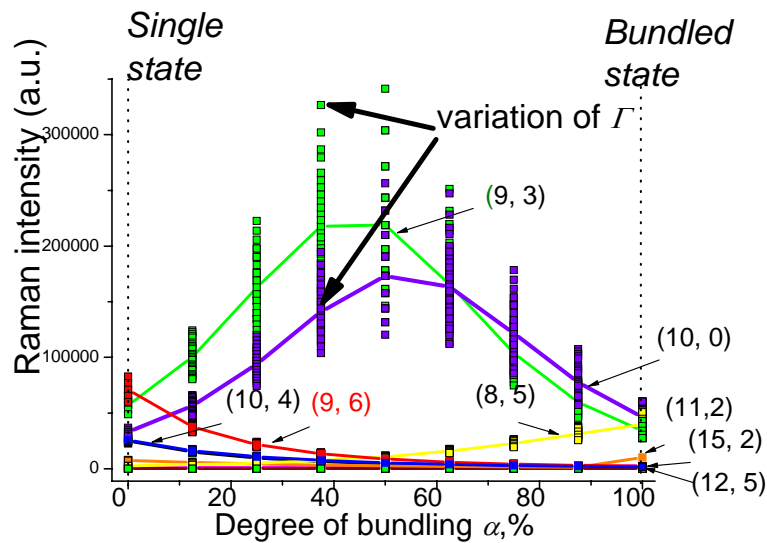


**Figure 5.12** Raman intensities vs. the degree of bundling  $\alpha$  calculated using eq. (4.16). The vertically scattered dots are for for all possible combinations of the parameters  $\Gamma_{\text{single}} = [50 - 70 \text{ meV}]$ , and  $\Gamma_{\text{bundled}} = [110 - 130 \text{ meV}]$  (see text for details).

The variation of the Raman intensities caused by possible uncertainty of the  $\Gamma$ -parameter (in modelled range) is quite large, especially for tubes (9, 3) and (10, 0). In order to check how the uncertainty of  $\Gamma$  influences the model, the experimental Raman spectra from single tubes (dispersions) and strongly bundled tubes (powders) were presented together with the modelled Raman intensities.

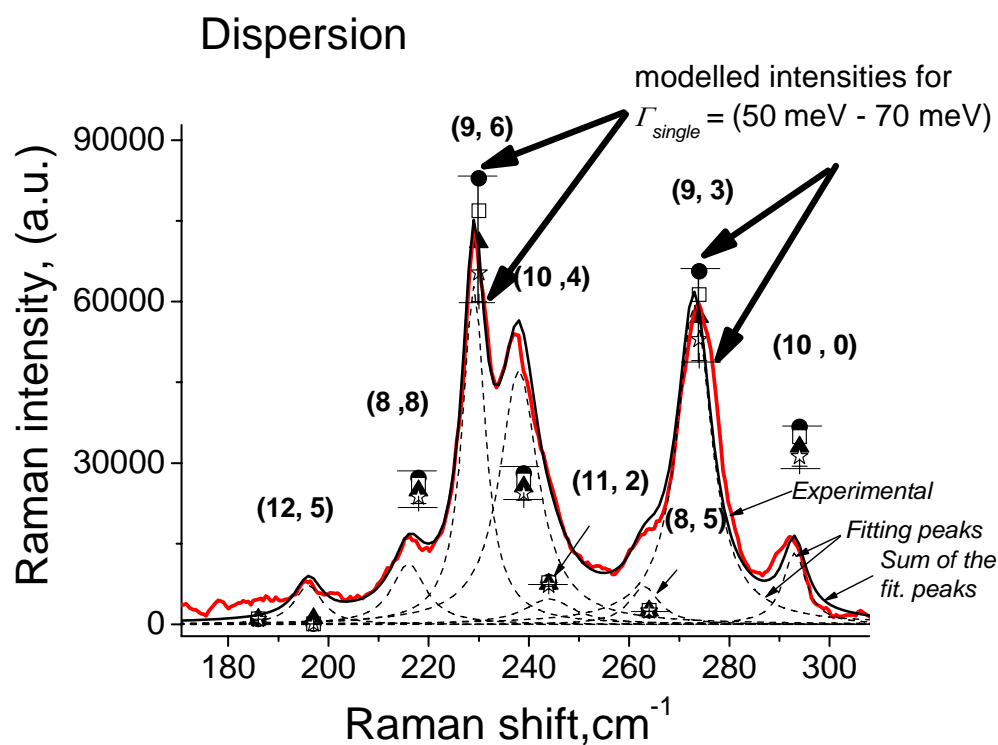


**Figure 5.13** Low frequency Raman spectra of single *HipCo*-tubes in the dispersion of  $D_2O/NaCholate$  and their Raman intensities calculated for the variation of the parameters  $\Gamma_{single} = [50 - 70 \text{ meV}]$ . Raman spectra are fitted with Lorentzian peaks.

Here the experimental RBM frequencies of single *HipCo*-tubes (and small bundles) in the dispersion of  $D_2O/NaCholate$  are presented with their theoretically calculated intensities (see Fig. 5.12,  $\alpha = 0 \%$ ) taking into account the variation of the  $\Gamma_{single} = [50 - 70 \text{ meV}]$ . The calculated intensities are shown as vertically spread symbols corresponding to different values of  $\Gamma_{single}$  for each tube. In Fig. 5.14 the analogous result for the strongly bundled nanotubes in powder samples is presented.

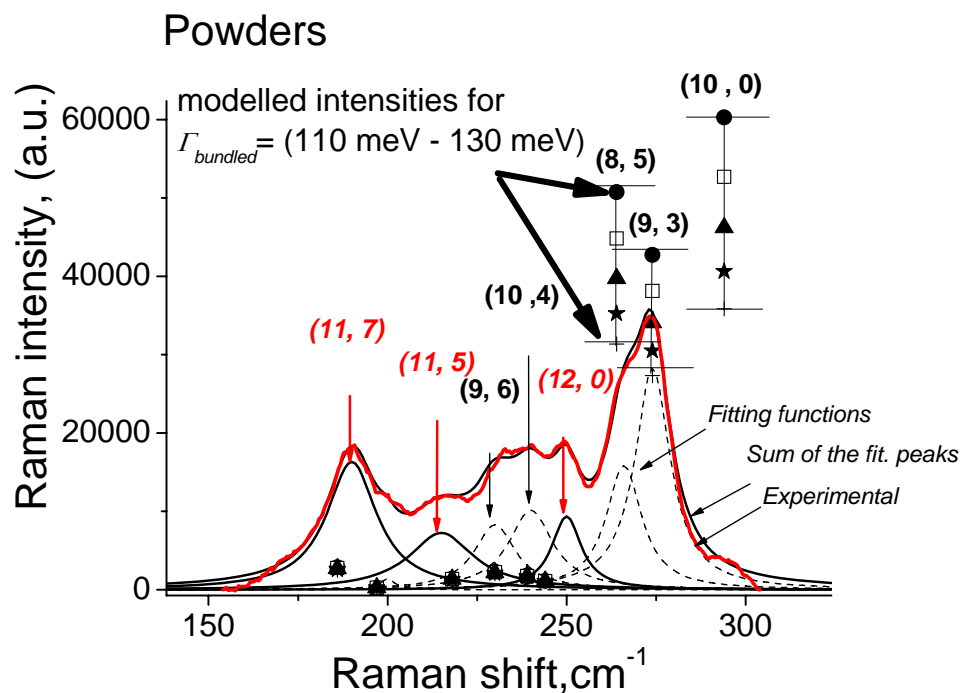


**Figure 5.14** Low frequency Raman spectra of bundled *HipCo*-tubes in powders and their Raman intensities calculated for the variation of the  $\Gamma_{\text{bundled}}$  parameter. Raman spectra were fitted with Lorentzian peaks.

Comparing the theoretical intensities with the experimental spectra (in Figs. 5.13 and 5.14) one can conclude: although the experiments are not described in every detail by this simple model the general trends are still well reproduced. There are many reasons for a certain discrepancy between the calculated and the experimental intensities. The most influential one is that the real systems (dispersions, powders) are far from the ideal modeled cases:

- (i) homogeneously distributed tubes that absolutely do not interact with the environment, or
- (ii) highly interacting and well-aligned tubes, and in any case at constant temperature.

Concerning the solid sample, the thermal down-shifts in the peak positions ( $\approx 2 \text{ cm}^{-1}$ ) indicate the heating of the sample by the laser beam. Heating can also influence the electronic and vibrational properties of the nanotubes (see *Chapter 6* about the temperature effects).

To conclude, the nanotube dispersions and their solid powders can be approximately modeled by the theory described above. The general trends are clearly seen. The experimental Raman intensities were found to be sensitive to the following factors not included in the present model:

- tube packing efficiency (in solid);
- tube alignment (in solid);
- relative concentration of different tubes (in dispersion and solid);
- temperature effect due to laser heating (in solid).

In order to find quantitative correlations between the Raman intensity and the bundle size one would need to study a sample with reduced influence of the factors listed above. The following section is devoted to such a study.

#### 5.4.2 Correlation between the Raman intensity, electronic energy shift and bundle size

*HipCo*-samples with *homogeneously distributed* tubes of different diameters were not available in this study. The dispersions of the *HipCo*-nanotubes obviously contain various partial concentrations of different tubes because of their different concentrations in the original material produced by the *HipCo*-method [55, 56]. Reducing the number of tube types active in Raman scattering makes it easier to produce a homogeneous sample of only few tube species.

The nanotubes grown by the *NiCo*-method have a narrower diameter distribution (see Fig. 3.9) and contain only two tubes which are active in Raman spectra for the excitation energy  $E_{\text{exc}} = 2.3$  eV (Fig. 5.15, b, c). These are the semiconducting tubes (11, 9) with  $\omega_{\text{RBM}} = 174$   $\text{cm}^{-1}$  and (15, 2) with  $\omega_{\text{RBM}} = 186$   $\text{cm}^{-1}$ .

Therefore, the *NiCo*-tubes were chosen for the estimation of the correlation between the Raman intensity, nanotube bundle size and the electronic energy shift. Electronic transition energies for two tubes (11, 9) and (15, 2) in single and bundled states can be found in Table 5.1. The ratio of the peak intensities  $y = I(174 \text{ cm}^{-1})/I(186 \text{ cm}^{-1})$  is the value reflecting the predominance of a certain kind of tube, i.e. the position of the nanotube electronic energies with respect to the laser energy (Fig. 5.10). Therefore, the Raman peak ratio  $y = I(174 \text{ cm}^{-1})/I(186 \text{ cm}^{-1})$  can serve as an *indicator for the degree of bundling* of the tubes (11, 9) and (15, 2).

In this study four kinds of *NiCo*-samples with tubes of different degree of bundling were used to determine the experimental correlation between the Raman intensity ratio and the nanotube bundle size. The procedure of the estimation of the experimental correlation is described in Section 5.2. Interesting areas of the sample previously studied with HRTEM or SEM could be found again with an optical microscope and their Raman spectra were then measured.

Fig. 5.15 (a) presents the SEM image of the first sample: a film produced from the dispersion of the *NiCo*-nanotubes in  $\text{D}_2\text{O}/\text{NaCholate}$ . The sample has cracks with nanotube bundles coming out of the film. These bundles can be scanned with the laser beam (marked as dotted circle) in order to obtain their Raman spectra.

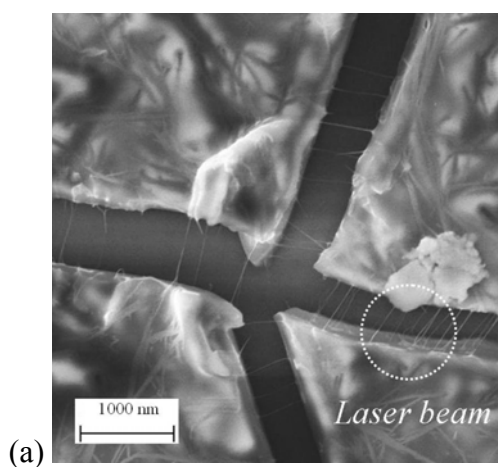
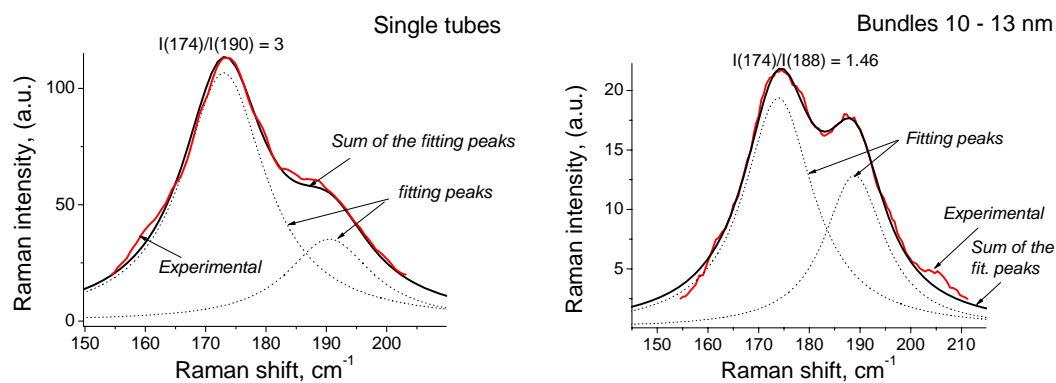


**Figure 5.15 (a)** SEM image of small bundles of *NiCo*-CNTs and single nanotubes strained between cracks in a film of the surfactant NaCholate (a);



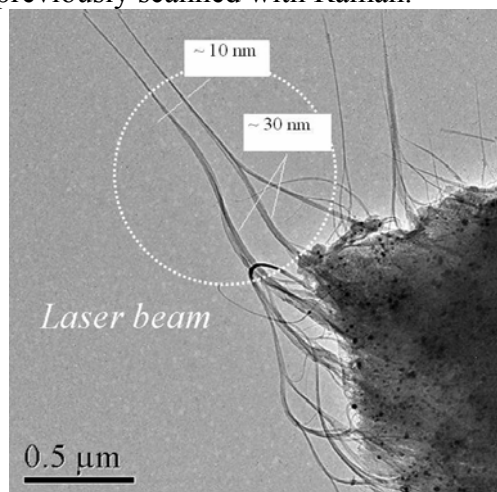
(b)

(c)

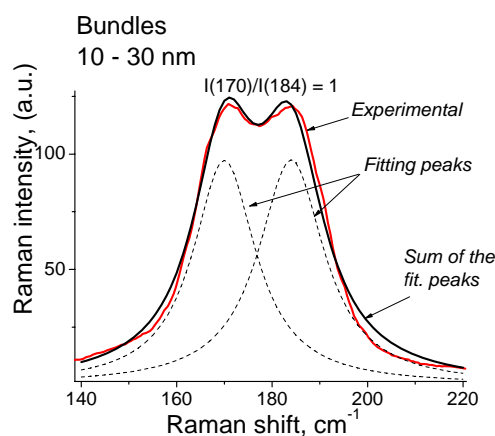
**Figure 5.15 (b, c)** Typical low frequency Raman spectra from the bundles coming out of the cracks: (b) single tubes and bundles  $\approx 2$  nm; (c) bundles 10 - 13 nm. The fitting of the Raman spectra has been done with Lorentzian peaks.

Figures 5.15 (b) and (c) present typical RBM Raman frequencies obtained by scanning the tube bundles along the cracks. A distribution of the bundle sizes for such a sample is about 2 – 13 nm (see also Fig. 5.7). The ratio between the Raman peaks appearing from two active tubes  $I(174 \text{ cm}^{-1})/I(186 \text{ cm}^{-1})$  varies from 3 for single tubes to 1.5 for bundles of about 10 – 13 nm.

The TEM image of the second sample used in this study is presented in Figure 5.16 (a). This is a piece of solid NiCo-nanotube material put on a standard gold HRTEM-grid. The grid had special markers which makes it possible to find the same part of the sample again (for instance, the sharp spike of the particle), that was previously scanned with Raman.



(a)



(b)

**Figure 5.16** HRTEM image of the solid NiCo-sample with different degree of tube bundling (a); typical Raman spectra obtained from circled area in the TEM image (b, c). The sizes of the bundles growing from the spike are 10 – 30 nm. The fitting of the Raman spectra has been done with Lorentzian peaks.

Typical Raman spectra from the bundles of 10 – 30 nm (circled white in Fig. 5.16 (a)) have the peak's ratio  $I(174 \text{ cm}^{-1})/I(186 \text{ cm}^{-1}) = 1$  (Fig. 5.16 (b)). A resolution of the bundle sizes was not possible within the laser beam area  $\approx 1 \mu\text{m}$  therefore this intensity ratio was attributed to the bundle size distribution 10 – 30 nm.

The third sample used for the estimation of the correlation was the surfactant film dried out on the Si-surface at room temperature (SEM image in Fig. 5.17 (a)). This sample showed distribution of the bundle sizes between 60 and 100 nm (with the mean size of about 80 nm). Here, typical Raman spectra have the peak's ratio  $I(174\text{ cm}^{-1})/I(186\text{ cm}^{-1}) \approx 1.7$  (Fig. 5.17 (b)). For the correlation this value was attributed to 80 nm within the distribution of the bundle sizes.

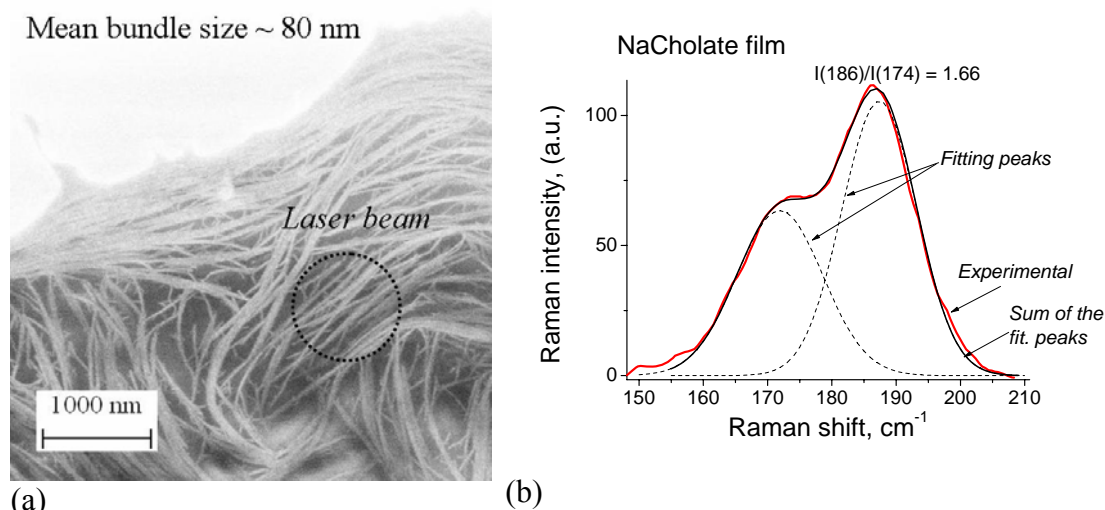


**Figure 5.17** SEM image of the *NiCo*-nanotubes inside the surfactant film (a), and typical RBM Raman frequencies from the area circled black in the SEM image (b). Lorentzian fitting.

Finally, a solid sample of the *NiCo*-nanotubes with large bundles along its edge was studied with both HRTEM (Fig. 5.18, a) and Raman scattering (Fig. 5.18, b).

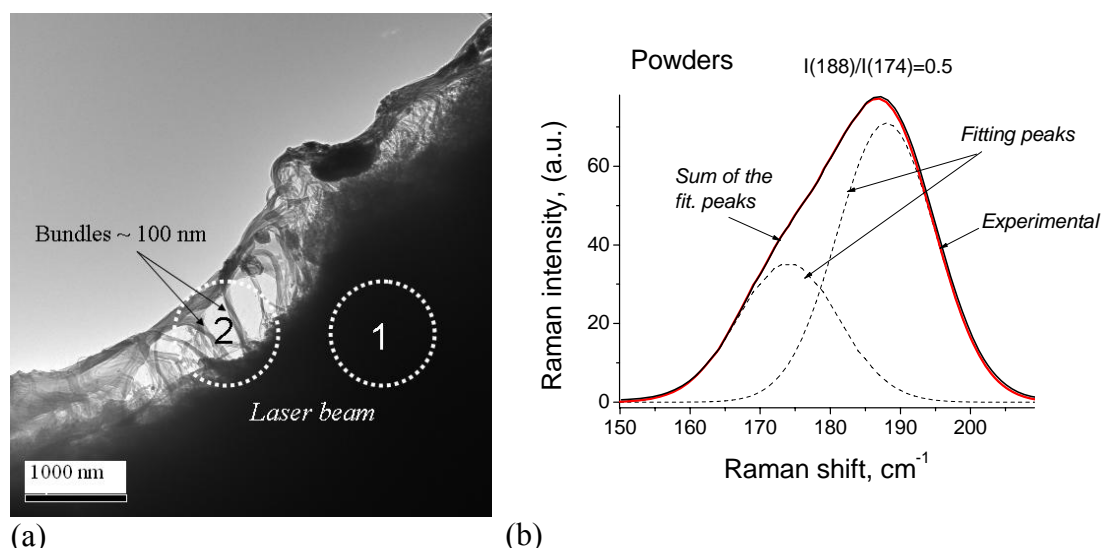


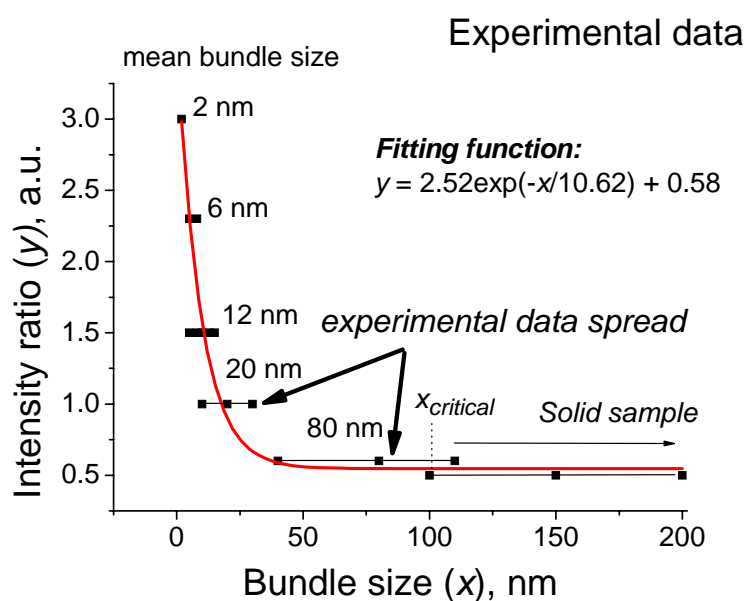
**Figure 5.18** HRTEM image of the solid *NiCo*-sample investigated with Raman; (a) typical RBM Raman frequencies from the circled area “2”. Lorentzian fitting.

The Raman spectra appear to be *the same* for the tightly pressed solid sample (circled area “1” in Fig. 5.18, a) as well as for nanotube bundles  $\approx 100$  nm (circled area “2” in Fig. 5.18, a). This result leads to a conclusion about the “critical” bundle size related to the “strongly-bundled state” in which the tubes exhibit maximum mutual interaction. Further increasing of bundling does not influence the electronic properties

of CNTs as they are bound with crystallitic forces. The critical bundle size  $x_{\text{critical}}$  for the strongly-bundled state was found to be about  $\approx 100$  nm.

All Raman spectra in Figs. (5.15) – (5.18) were fitted with Lorentzian peaks using the program *Fityk* for nonlinear fitting of analytical functions [110]. The fitting has been done for *the same* parameter of the full width at the half maximum (FWHM). Therefore, the maxima of the Raman peaks can be taken as the characteristic of the nanotube ensemble instead of the total peak area.

The *experimental correlation* between the Raman intensity and the bundle size derived using combined HRTEM, SEM and Raman study (Figs. 5.15 – 5.18), as just described is presented in Fig. 5.19.

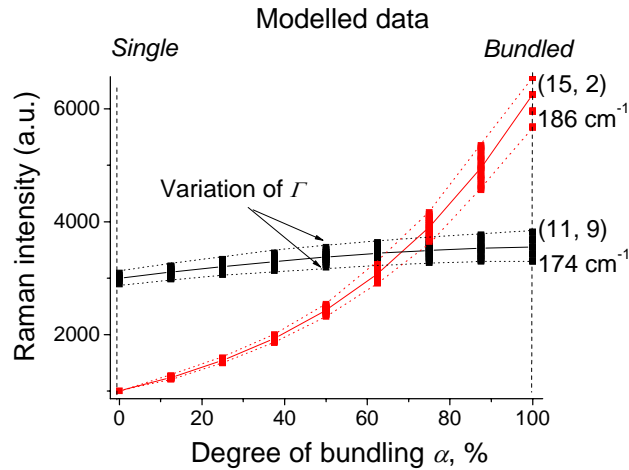


**Figure 5.19** Experimental correlation between the intensity ratio ( $y$ ) of the Raman peaks from tube (11, 9) and (15, 2) and the nanotube bundle size ( $x$ ). Combination of HRTEM, SEM and Raman study (for  $E_{\text{exc}} = 2.3$  eV).

The data spread along the  $x$ -axis corresponds to the distribution of the bundle sizes in the samples in Figs. (5.15) – (5.18). For the small bundle sizes the variation of the intensity ratio  $y(x)$  is quite large demonstrating a strong dependence on the bundle size  $x$  up to  $x \approx 30$  nm. The relation demonstrates a decay-like character and converges to the value of the intensity ratio  $y_0 = 0.58$  for large  $x$ . This dependence can be fitted with an exponent  $y = A\exp(-x/t) + y_0$ , where  $A = 2.52$ ,  $t = 10.62$ , and  $y_0 = 0.58$ .

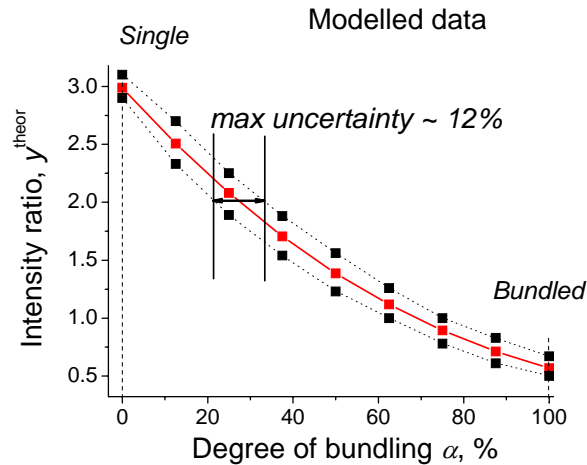
The physics behind the exponential dependence is not completely clear. It provides only a *qualitative* description of the experimental data.

Estimation of the correlation between the degree of nanotube bundling and the energy shift would need *a combination of the experiment and theory*. The data from the empirical correlation presented in Fig. 5.19 must be related to the theoretical Raman intensities vs. the electronic energy shifts calculated within the theoretical model described in Section 5.4.1. This calculation was carried out in two steps. First, the Raman intensities for two tubes (11, 9) and (15, 2) were calculated as a function of the degree of bundling  $\alpha$  (Fig. 5.20). Then their ratio was calculated as a function of  $\alpha$  (Fig. 5.20, b).

**Figure 5.20 (a)**

Raman intensities for the tubes (11, 9) ( $\omega_{\text{RBM}} = 174 \text{ cm}^{-1}$ ) and (15, 2) ( $\omega_{\text{RBM}} = 186 \text{ cm}^{-1}$ ) vs. the degree of bundling  $\alpha$  calculated using Eq. (4.16).

(a)

**Figure 5.20 (b)**

The ratio  $I(174 \text{ cm}^{-1})/I(186 \text{ cm}^{-1})$  between the Raman intensities of the tubes (11, 9) and (15, 2) vs. the degree of bundling  $\alpha$  calculated using Eq. (4.16).

(b)

The parameters for the calculation of the Raman intensities were taken as follows: for the tube (11, 9):  $E_{\text{single}} = 2.43 \text{ eV}$ ,  $E_{\text{bundled}} = 2.41 \text{ eV}$ ; for the tube (15, 2):  $E_{\text{single}} = 2.47 \text{ eV}$  and  $E_{\text{bundled}} = 2.39 \text{ eV}$  (see Table 5.1). With increasing  $\alpha$ , the tube (15, 2) moves to the resonance faster than tube (11, 9) because the value of the energy shift  $\Delta(E_{\text{single}} - E_{\text{bundled}})/\Delta\alpha$  is larger for (15, 2) than for (11, 9). Therefore, the intensity of the peak of the (15, 2) tube grows faster with  $\alpha$  than for the (11, 9) tube (Fig. 5.20, a).

The parameter  $\Gamma$  was taken to be:  $\Gamma_{\text{single}} = [50 - 70 \text{ meV}]$  and  $\Gamma_{\text{bundled}} = [110 - 130 \text{ meV}]$ . The vertically dispersed points in Fig. 5.20, (a, b) show the intensity variation caused by changing of  $\Gamma$  (see Section 5.4.1). The maximum uncertainty of the theoretical intensity ratio  $y$  due to the variation of  $\Gamma$  is  $\approx 12\%$  (Fig. 5.20, b).

Finally, the theoretical Raman intensity ratio  $y^{\text{theor}}$  vs. degree of bundling  $\alpha$  (Fig. 5.20 (b)) can be combined with the experimental Raman intensity  $y$  ratio vs. bundle size  $x$  (Fig. 5.19.). In this way, the *semiempirical* correlation between the degree of bundling  $\alpha$  and the bundle size  $x$  can be derived. The result of such a combination is presented in Fig. 5.21.

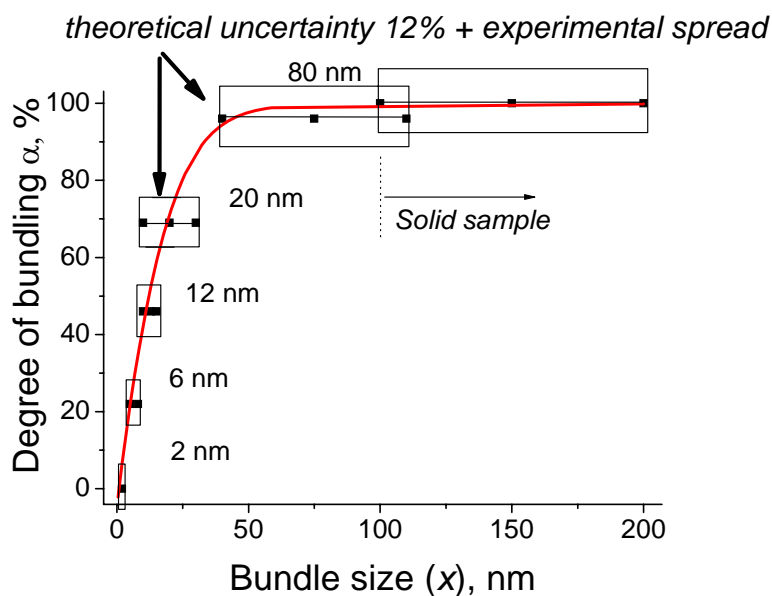


**Figure 5.21** Semi-empirical correlation between the degree of bundling  $\alpha$  and the nanotube bundle size  $x$ . Rectangles indicate the theoretical uncertainty of 12% and the experimental data spread.

The data in Fig. 5.21 (b) are surrounded by rectangles indicating the theoretical uncertainty 12% (vertically) and the experimental data spread (horizontally). Fitting of the data had been done *numerically* by re-calculating the exponential dependence  $y(x)$  (Fig. 5.19) and the polynomial dependence  $y^{\text{theor}}(\alpha)$  (Fig. 5.20, b) into  $\alpha(x)$ . The function in Fig. 5.21 demonstrates a saturation-like behaviour for large  $x$ .

Although, this correlation was derived using the Raman intensity ratios of only two tubes, it could be considered after the theoretical re-calculation as *universal for any kind of tube* ( $n, m$ ) since it describes simply the relative energy shift  $\alpha$  in % with respect to the single state. Of course, one should bear in mind the assumption of the synchronous shifts of energies for all the tubes with bundling (Section 5.4.1). In other words, the correlation is valid only for the tubes whose electronic energies are modified *by the same value*  $\alpha$  for the same  $x$ .

## 5.5 Summary

In this chapter an empirical correlation between the nanotube bundle size  $x$  and the Raman intensity ratio  $y$  was demonstrated for the first time. It was obtained by HRTEM and SEM techniques combined with Raman scattering. The correlation was fitted with the exponential function which converges to the value  $y = 0.58$  for large bundle size  $x$ . Starting from  $x^{\text{critical}} \approx 100$  nm, further increasing of the bundle size does not detectably change the Raman intensity ratio, i.e. does not influence the electronic properties of CNTs as they are bound with strong crystallitic forces.

Furthermore, a semi-empirical correlation between the relative energy shift  $\alpha$  (or degree of bundling) and the bundle size  $x$  was derived combining the theoretical model for the calculation of the Raman intensities vs.  $\alpha$  with the empirical correlation for Raman intensities vs. bundle size  $x$ . This correlation can be applicable within the

assumption about the synchronous energy shift of different tubes with bundling. Both correlations provide an idea about the saturation of the nanotube interaction at some value of the bundle size.



# Chapter 6

## Temperature Effects

In *Chapter 6* the influence of temperature on the electronic properties of carbon nanotubes will be considered experimentally and within the theoretical model. *Chapter 6* has the following structure:

- Motivation with analysis of the theoretical model for the temperature dependence of the band gap of semiconducting nanotubes; corrections to the model for study of the electronic transitions of CNTs in the present samples;
- Combination of two models: the model for the temperature dependence of the electronic energies and the model developed for the influence of the tube-tube interaction (*Chapter 5*);
- Calculation of the Raman intensities of semiconducting nanotubes within the combined model as a function of both temperature and degree of nanotube bundling;
- Temperature-dependent Raman scattering experiments on samples with *semiconducting* CNT having different degree of bundling;
- Comparison between the calculated and the experimental Raman intensities as a function of temperature; analysis of the theory applicability;
- Finally, the temperature-dependent Raman scattering experiments on samples with *metallic* nanotubes; conclusion about the possible temperature dependence of their electronic structure.

### 6.1 Motivation

The influence of temperature on Raman-active modes of carbon-based materials such as diamond, highly oriented pyrolytic graphite (HOPG), and single-crystalline graphite has been widely studied [63 – 67]. Thermal shifts of the phonon modes in these materials usually indicate changes in the elastic modulus and reflect two effects: changes in the interatomic distances due to thermal expansion of the crystalline lattice (pure volume effect) and a softening of the elastic modulus due to the temperature increase (pure temperature effect). The frequency change can be written as

$$\Delta\omega = \left(\frac{\partial\omega}{\partial T}\right)_V \Delta T + \left(\frac{\partial\omega}{\partial V}\right)_T \left(\frac{\partial V}{\partial T}\right)_P \Delta T$$

In diamond and graphite thermal shifts are caused by both volume and temperature effects. In contrast, single crystal graphite and HOPG, as well as carbon nanotubes with well graphitized structure have high thermal conductivity, and there was no significant in-plane thermal expansion detected by X-ray measurements [68, 69]. Therefore, a small downshift in their Raman frequencies is attributed to a purely thermal effect  $\sim \left(\frac{\partial\omega}{\partial T}\right)_V$ . Defects (vacancies, impurities, structural disorder) reduce the thermal conductivity leading to larger C-C bond stretching, and the observed

downshifts in Raman frequency arise due to both temperature and volume  $\sim \left(\frac{\partial \omega}{\partial V}\right)_T \left(\frac{\partial \omega}{\partial T}\right)_P$  effects [68, 69].

It is obvious that the influence of temperature on the electronic properties of the CNT material provides important insight into the nature of the electron-phonon interactions. As mentioned in *Chapter 4* the unique properties of 1D carbon nanotubes manifest themselves in a strong electron-phonon coupling, and their Raman spectra reflect both vibrational and electronic properties. Therefore, thermal shifts in Raman spectra of carbon nanotubes should reflect the influence of temperature on the electronic properties of nanotubes as well. Up to now, however, there were very few theoretical [19, 70] and experimental publications [18, 71] devoted to the influence of temperature on the band gap of semiconducting carbon nanotubes, and no information is currently available on the influence of temperature on metallic nanotubes. Partly, the lack of information can be explained by the absence of a universal model and experimental method for nanotube  $(n, m)$  assignment. A further reason is the necessity to perform measurements of the band gap value (or higher interband transition energies) on *single* nanotubes, as bundling effects substantially change their electronic properties (see Chapter 5). The method of individualizing tubes inside micelles was invented relatively recently [17]; since then there have been many successful efforts to find a route to  $(n, m)$  assignments using vibrational as well as photoluminescence spectroscopy.

This Chapter presents the study of the temperature influence on the electronic properties of carbon nanotubes and is based on three main parts:

- analysis of Raman intensities of the RBM frequencies as a function of temperature;
- application of the theoretical model of the electronic energy shifts developed for bundling effects (see Chapter 5);
- application of the theory of temperature dependence of the band gap of semiconducting carbon nanotubes recently developed by R. Capaz *et al.* [19].

## 6.2 Theoretical model for temperature behaviour of the band gap of semiconducting CNTs

The temperature dependence of the band gap ( $E_g$ ) is one of the fundamental signatures of a semiconductor reflecting processes of electron-phonon ( $e-ph$ ) interactions. Usually,  $E_g(T)$  curves show a monotonic decrease with increasing temperature that is nonlinear at low  $T$  and linear at sufficiently high  $T$  [73, 74]. Understanding  $E_g(T)$  for nanotubes is extremely important since experiments are often performed at room temperature and the corresponding predictions are usually done at  $T = 0$ .

A model for the temperature dependence of the band gap of semiconducting single-walled nanotubes has been proposed by Capaz *et al.* [19]. It is based on the direct evaluation of electron-phonon coupling within a “frozen-phonon” scheme for the single-particle band gap. A complex dependence of  $E_g(T)$  on chirality and diameter with an unusual *nonmonotonic* behavior for certain classes of tubes was found. This behavior arises from the difference in sign of the  $e-ph$  coupling associated with low-energy optical phonons. Using the relation for  $E_g(T)$  derived by Capaz *et al.* one can calculate the temperature behavior of the band gap of any given SWCNT as a function of diameter and chirality. The common relation for the band gap energy change for a semiconductor within a two-phonon model [75] is

$$\Delta E_g(T) = \frac{\alpha_1 \Theta_1}{e^{\Theta_1/T} - 1} + \frac{\alpha_2 \Theta_2}{e^{\Theta_2/T} - 1}, \quad (6.1)$$

where  $\Theta_1$  and  $\Theta_2$  ( $\Theta_1 < \Theta_2$ ) are “effective temperatures” for two “average phonons”,  $\alpha_j \Theta_j = \partial E_g / \partial n_j$  are their effective  $e-ph$  coupling coefficients, and  $n_j = (e^{\beta \hbar \omega_j} - 1)^{-1}$  is the Bose-Einstein occupation number of the phonon mode  $j$ . The parameters  $\alpha_j$  and  $\Theta_j$  depend on the SWCNT’s diameter and chirality [19] as follows: the effective frequency for the lowest-energy phonon mode  $\Theta_j$  dictating the behavior of  $E_g(T)$  at low  $T$  ( $< 100$  K) is proportional to the inverse square of the diameter  $d$  and does not depend on chirality:

$$\Theta = \frac{A}{d^2}. \quad (6.2)$$

We note that Eq. (6.2) is in contradiction with the empirical  $1/d$  dependence of the RBM. Taking into account the other proposed empirical dependence (Eq. (4.19)) we use Eq. (6.2) in the framework of Eq. (6.1) for consistency.

The dependence on chirality can be expressed as polynomial expansions  $f(\xi)$  of a “chirality variable”  $\xi = (-1)^\nu \cos(3\theta)$ , where  $\nu = \text{Mod}[(n-m)]$  is the number defining the family of the semiconducting tube. The second order term is then [19]:

$$f_\eta(\xi) = \gamma_1^\eta \xi + \gamma_2^\eta \xi^2, \quad (6.3)$$

where  $\eta$  indicates the parameter under consideration. The parameter  $\alpha_1$  is given by

$$\alpha_1 = \alpha_1^0 + f_{\alpha_1}(\xi)d. \quad (6.4)$$

The parameters  $\alpha_1$  and  $\Theta_2$  effectively represent a large number of phonon modes that start to become “active” at temperatures between 350 and 500 K. They are given by the following expressions:

$$\Theta_2 = \Theta_2^\infty + \frac{f_{\Theta_2}(\xi)}{d}, \quad (6.5)$$

$$\alpha_2 = \frac{1}{d} \left( B + \frac{f_{\alpha_2}(\xi)}{d} \right). \quad (6.6)$$

The equations (6.1) – (6.6) provide a recipe for the estimation the band gap shifts as a function of temperature *for any tube*. The ten parameters obtained by best fits [19] are the following:

$$A = 9.45 \cdot 10^3 \text{ K}; \alpha_1^0 = -1.70 \cdot 10^{-5} \text{ eV/K}; \gamma_1^{\alpha_1} = 1.68 \cdot 10^{-6} \text{ eV/K}; \gamma_2^{\alpha_1} = 6.47 \cdot 10^{-7} \text{ eV/K}; \\ \Theta_2^\infty = 470 \text{ K}; \gamma_1^{\Theta_2} = 1.06 \cdot 10^3 \text{ K}; \gamma_2^{\Theta_2} = -5.94 \cdot 10^{-2} \text{ K}; B = -4.54 \cdot 10^{-4} \text{ eV/K}; \\ \gamma_1^{\alpha_2} = -2.68 \cdot 10^{-3} \text{ eV/K}; \gamma_2^{\alpha_2} = -2.23 \cdot 10^{-5} \text{ eV/K}.$$

The contribution of an anharmonic term to the band gap variation with  $T$  is found to be quite small ( $\approx 0.2$  meV at 300 K for the tube (10, 0)) and can be neglected in this consideration. Capaz *et al.* [19] consider an anharmonic term as caused by changes in C-C bond lengths and angles rather than by changes in the lattice force constants. The theory described above was developed for the temperature range [0 – 400 K]. At higher temperatures a renormalization of the bands is expected.

In this work the maximum temperatures were  $\approx 450$  K, therefore, the theoretical limit of  $T_{\max} = 400$  K was not substantially exceeded and the theory can be used. The theory developed by Capaz *et al.* [19] can be used not only for the calculation of the band gap values as a function of  $T$  but also for higher interband electronic transition energies  $E_{ii}$ . In that case, the sign of  $(-1)^v$  in the chirality variable  $\xi$  should be reversed and the parameters  $\alpha_1$  and  $\alpha_2$  in eqs. (6.4) and (6.6) should be rescaled by a corresponding factor according to the ratios between the electronic transition energies are  $E_{11}(=E_g)/E_{22}/E_{33}/E_{44} \dots = 1/2/4/5 \dots$

Figure 6.1 presents the electronic transition energies  $E_{33}$  versus temperature  $T$  calculated with eqs. (6.1) – (6.6) for two experimentally accessible semiconducting nanotubes (11, 9) and (15, 2). The laser excitation energy  $E_{\text{exc}} = 2.3$  eV will be in resonance with the third electronic interband transitions  $E_{33}$  of these tubes. The eq. (6.1) must be rescaled by a factor of 4 since  $E_g/E_{33} = 1/4$ .

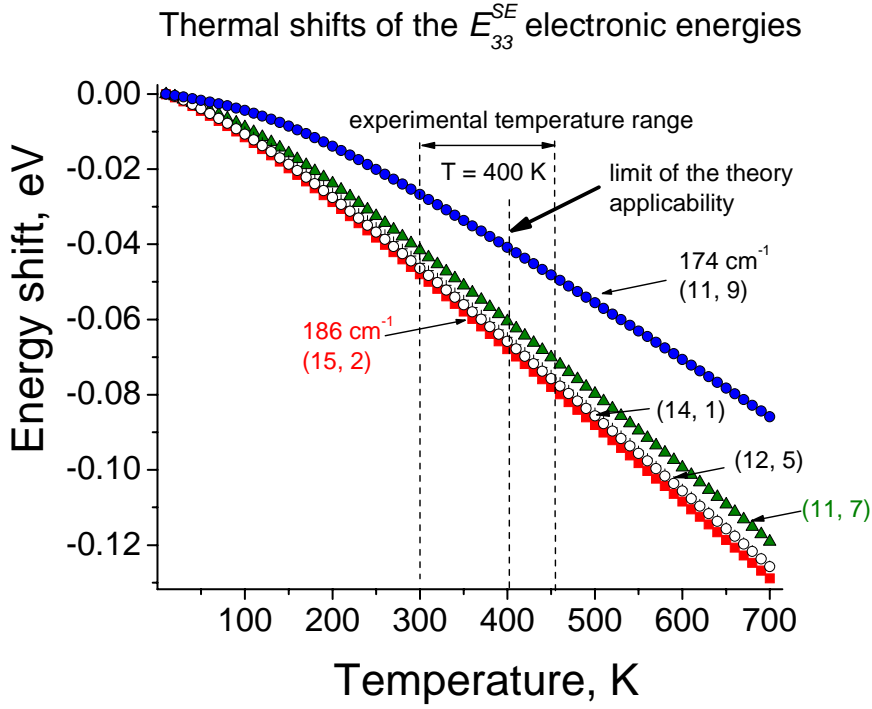


**Figure 6.1** Electronic transition energies  $E_{33}^{ME}$  for five semiconducting nanotubes calculated using theory of the temperature dependence of the band gap [19] in a wide temperature range [0 – 700 K].

The theoretical shifts of  $E_{33}^{SE}(T)$  are about the same for the tubes (15, 2), (14, 1), (12, 5), and (11, 7). However, they are different for the tubes (11, 9) and (15, 2): the thermal shift coefficient  $\Delta E_{33}^{SE}(T)/\Delta T \approx 0.13$  meV/K and  $\approx 0.2$  meV/K, respectively. It means that the peak intensity of the tube (15, 2) will grow faster with temperature since (15, 2) moves to the resonance with  $E_{exc}$  faster than (11, 9) (has larger coefficient  $\Delta E_{33}^{SE}(T)/\Delta T$ ).

To adapt this theory to the experiment one should take into account bundling of the nanotubes in real samples. Bundling shifts the electronic transition energies of the nanotubes depending on the bundle size (*Chapter 5*). In a bundled sample the initial electronic energies will be shifted even at room temperature. Following heating of the sample modifies these perturbed by tube-tube interaction energies according to the model described above.

The electronic energy shifts caused by both bundling and temperature can be modelled using the combined code developed for bundling effects (*Chapter 5*) and the theory for temperature dependence of the band gap values proposed by R. Capaz *et al.* [19]. For that purpose, in the theory [19] the initial electronic energies of the semiconducting tubes (11, 9) and (15, 2) at  $T_{room}$  were substituted by the energies modified by different degree of bundling  $\alpha$ . Then the temperature shifts of the electronic energies were calculated for those perturbed electronic energies using Eqs. (6.1) – (6.6). Finally, the Raman intensities (and their ratio) of two tubes were calculated using eq. (4.16) as a function of  $T$  for different degrees of bundling  $\alpha$ . The result of such a calculation is presented in Fig. 6.2. Here the resonance window widths  $\Gamma$  are taken as  $const(T)$  since their variation does not substantially change the final result.

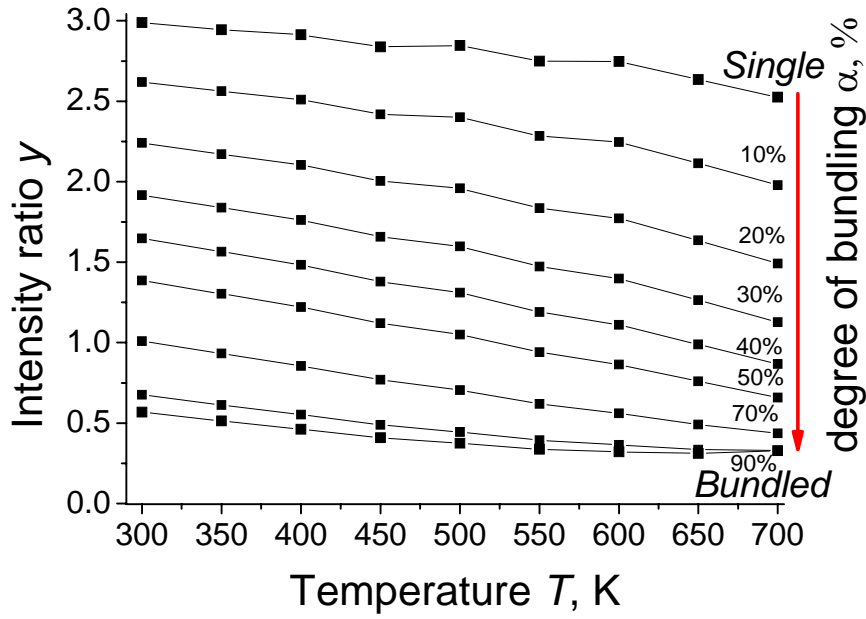


**Figure 6.2** Raman intensity ratio of two tubes (11, 9) and (15, 2) versus temperature for different degrees of bundling  $\alpha$  calculated within the combined model (see text). Parameters were taken as follows:  $E_{\text{single}} = 2.47$  eV,  $E_{\text{bundled}} = 2.39$  eV ( $186$   $\text{cm}^{-1}$ ),  $E_{\text{single}} = 2.43$  eV,  $E_{\text{bundled}} = 2.41$  eV ( $174$   $\text{cm}^{-1}$ ),  $\Gamma_{\text{single}} = 0.06$  eV,  $\Gamma_{\text{bundled}} = 0.12$  eV,  $\Gamma = \text{const}(T)$ .

Here the intensity ratio of two Raman peaks  $y = I(174 \text{ cm}^{-1})/I(186 \text{ cm}^{-1})$  is plotted as a function of temperature for different degree of bundling  $\alpha$ . Temperature varies in a range from  $T_{\text{room}} = 300$  K to  $T_{\text{burn}} = 700$  K (temperature of the nanotube burning).  $T_{\text{burn}}$  exceeds the limit of the Capaz's theory applicability  $T_{\text{max}} = 400$  K. However, this result can be useful for the general consideration of the band gap behaviour at high temperature.

The curves show a *monotonic decrease* of the Raman intensity ratio  $y$  with  $T$  for all bundle sizes up to  $\alpha = 90\%$  (bundle sizes  $> 60$  nm). For  $\alpha > 90\%$  at  $T \geq 650$  K the electronic energy  $E_{33}^{\text{SE}}$  of the tube (15, 2) crosses the resonance energy  $E_{\text{exc}} = 2.3$  eV and further increase of  $T$  results in an increase of the ratio  $y$ .

## 6.3 Experimental results

### 6.3.1 Samples and experimental details

The samples for the study of the temperature effects were prepared from dispersions as described in Section 5.2. The spin-casting method provides a thin film of nanotubes covered with molecules of the surfactant Na/Cholate on the Si-surface. In the present experiment temperature of the samples can be varied in two ways: by changing the intensity of the laser beam or by heating up the sample on a copper heater plate.

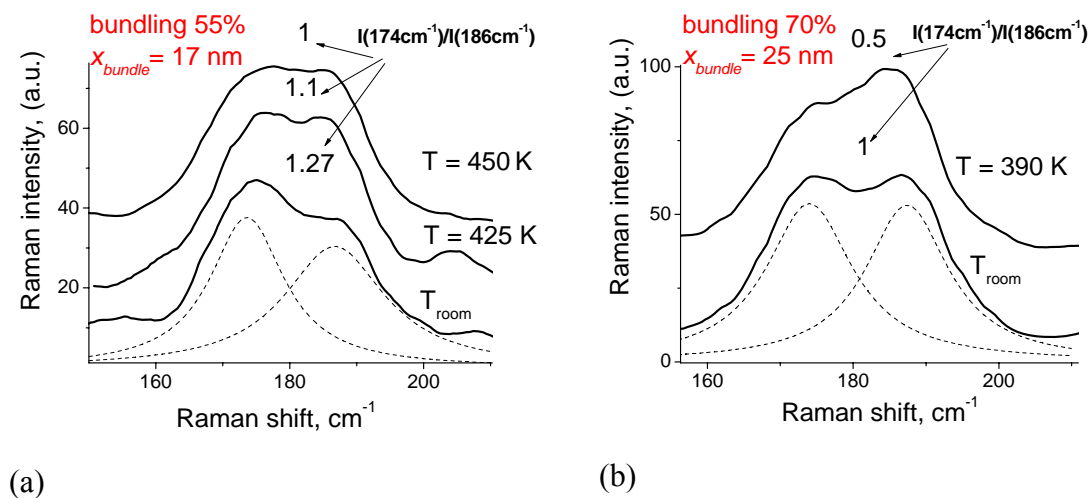
In the case of the heating with the laser beam temperature of the sample is unknown due to the absence of a preliminary procedure for temperature calibration. The usual method of the temperature estimation with Stokes and Anti-Stokes line ratio is not applicable for carbon nanotubes since their Raman spectra are excitation-energy dependent. It leads to the excitation of *different* tubes in Stokes and Anti-Stokes spectra for a given  $E_{\text{exc}}$  [72].

Therefore, the samples were heated up with the hot copper plate after careful calibration of temperature with the surface thermometer. The sample temperature does not exceed 450 K (melting temperature of the surfactant film).

In this study the NiCo-samples with two Raman-active (for  $E_{\text{exc}} = 2.3$  eV) nanotubes (11, 9) and (15, 2)) were used. After a set of measurements at different temperatures Raman spectra were reproduced again at  $T_{\text{room}}$  to reassure that the investigated area had not changed its properties.

### 6.3.2 Temperature changes in Raman spectra of semiconducting nanotubes

The temperature-dependent Raman experiment on nanotube films had been carried out as follows. First, the most interesting areas of the sample, for instance, those with surface cracks (see Figs. 5.6, 5.7) were selected by optical microscopy. These areas can be easily recognized any time, even after a thermal drift of the investigated points due to the thermal expansion of the Si-surface. For these regions the Raman spectra were measured at different temperatures. The result of such a temperature-dependent Raman study is presented in Fig. 6.3 (a-c).



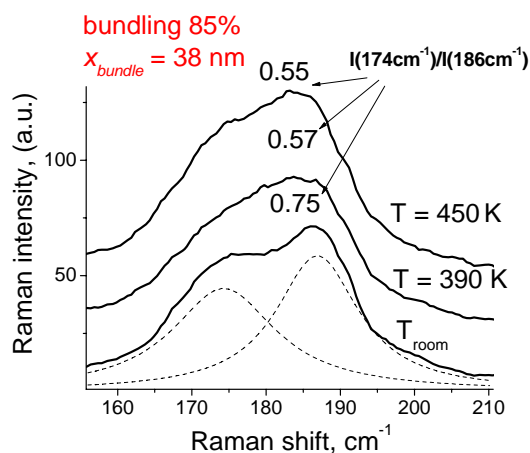


**Figure 6.3** (a-c) Low frequency Raman spectra from the samples with different degree of bundling measured at different temperatures (a-c); the Lorentzian fit of the peaks at  $174 \text{ cm}^{-1}$  and  $186 \text{ cm}^{-1}$  (dotted profiles) is presented only for the lowest curves.

(c)

The three sets of the Raman spectra (a – c) are obtained from areas with different degree of the nanotube bundling. The degree of bundling can be easily determined from the spectra measured at  $T_{\text{room}}$  simply analysing the ratio of the peaks  $y = I(174 \text{ cm}^{-1})/I(186 \text{ cm}^{-1})$ . The values  $y$  are 1.27, 1 and 0.75 for the spectra (a), (b) and (c), respectively. In *Chapter 5* two correlations for the Raman intensity ratio vs. bundle size (Fig. 5.20) and for the degree of bundling vs. bundle size (Fig. 5.21) were derived. With these correlations one can estimate the bundle size  $x$  and the degree of bundling  $\alpha$  for the ratios  $y$ , i.e.  $x \approx 17 \text{ nm}$  ( $\alpha = 55 \%$ ) for  $y = 1.27$  (a);  $x \approx 25 \text{ nm}$  ( $\alpha = 70 \%$ ) for  $y = 1$  (b);  $x \approx 40 \text{ nm}$  ( $\alpha = 85 \%$ ) for  $y = 0.75$  (c). With increasing  $T$  of the sample the intensity of the peak at  $186 \text{ cm}^{-1}$  grows with respect to  $174 \text{ cm}^{-1}$  for all three sets of spectra in Figs. 6.3 (a – c).

Fig. 6.4 shows the theoretical ratios of the Raman peak intensities vs. temperature calculated within the modified model (see Fig. 6.2) for three experimental bundling degrees  $\alpha = 55 \%$ ,  $70 \%$  and  $85 \%$ . Here, the experimental peak ratios from Fig. 6.3 (a – c) are also presented. The theoretical data are marked as closed squares connected with lines. The experimental data are marked as triangles.

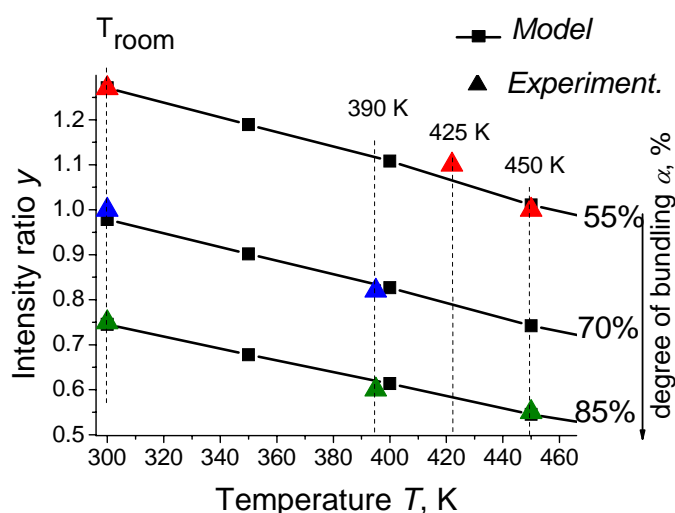


**Figure 6.4** Theoretical Raman intensity ratio  $y$  (squares) for two tubes (11, 9) and (15, 2) with calculated within the combined theoretical model for  $\alpha = 55 \%$ ,  $70 \%$  and  $85 \%$  (see text for details) and the experimental intensity ratios (triangles) obtained from the spectra in Fig. 6.3 (a – c).

Fig. 6.4 shows a very close agreement between the experiment and the comparatively simple theory bearing in mind the approximations and limitations of the model. Among these approximations is an assumption about the *synchronous shift* of the electronic energies for different tubes in the same environment (Section 5.4.1). The agreement between the experimental and theoretical data confirms this assumption at least, for two semiconducting tubes (11, 9) and (15, 2). Therefore, the model developed in *Chapter 5* for study of the bundling effects is consistent and can be used for the analysis of both bundling and temperature effects.

The set of curves in Fig. 6.2 calculated for the degree of bundling  $\alpha = (0 - 100\%)$  provides, thus, a ready-to-use correlation between the Raman intensity ratio for two nanotubes  $I(174 \text{ cm}^{-1})/I(186 \text{ cm}^{-1})$  and temperature at the laser excitation energy  $E_{\text{exc}} = 2.3 \text{ eV}$ . From these curves one can determine for example, temperature and electronic energies of the nanotubes (11, 9) and (15, 2) if the experimental temperature  $T$  is unknown.

The same procedure can be reproduced, in principle, for any other set of semiconducting tubes at different  $E_{\text{exc}}$ . The only critical point is the correct calculation of the Raman intensities which requires the evaluation of the matrix element for *e-ph* coupling. In this consideration, however, these effects were neglected (see Section 4.2).

The next interesting question is: what happens to the electronic energies of *metallic* nanotubes with changing temperature?

### 6.3.3 Temperature changes in Raman spectra of metallic nanotubes

Up to the present time no experimental data as well as theoretical calculations concerning the influence of temperature on  $E_{ii}$  values of metallic nanotubes were available in literature. This work presents first attempts of such a study.

In order to understand the difference between ordinary metals and metallic carbon nanotubes one should compare their basic properties given in Table 6.1.

**Table 6.1** Parameters of metallic CNTs compared to the nanowire of copper [76].

Parameters	<i>Single CNT</i>	<i>Cu 22 nm via node</i>
Resistance (Ohms)	$6.5 \cdot 10^3$	4
Max current density (A/cm <sup>2</sup> )	$\sim 10^9$	$\sim 10^7$
Temperature coefficient of resistivity ( $^{\circ}\text{C}$ )	$-1.5 \cdot 10^{-3}$	$+4 \cdot 10^{-3}$
Thermal conductivity (W/mK)	6600	400

Carbon nanotubes are ballistic conductors which can support huge current densities of up to  $10^9 \text{ A/cm}^2$ . Compared to metals, CNTs have a negative temperature coefficient of resistivity and high thermal conductivity. All these characteristics make CNTs attractive for the nanoelectronic applications [76]. For some applications, however, metallic nanotubes will be used in a wide temperature range where their electronic characteristics must be predictable.

In this section the influence of temperature on the energy separations  $E_{ii}$  of metallic *HipCo*-nanotubes was investigated using the resonance Raman spectroscopy which provides information about the vibrational and the electronic properties of nanotubes.

The temperature-dependent Raman experiment on the metallic nanotubes had been carried out similar to that on semiconducting *NiCo*-nanotubes (Section 6.3.2). The *HipCo*-nanotube films on the Si-surface were prepared from the nanotube solutions using the spin-casting method (Section 5.2). Temperature of the samples was controlled varying the laser beam power in a range of 0.1 – 2.5 mW. Heating with the heating plate (as for semiconducting *NiCo*-CNTs) was not possible due to the burning of the smallest *HipCo*-tubes (with  $d < 1$  nm and  $\text{RBM} > 236$   $\text{cm}^{-1}$ ) under the laser irradiation at relatively low  $T < 400$  K of the plate. In that case the simultaneous heating of the sample by the laser beam and the plate leads to high local temperatures of about 700 K at which the smallest nanotubes burn out. Therefore, the present study is focused only on the *general trends* of temperature effects with no exact temperature values given. Figure 6.5 presents two Raman spectra of the *HipCo*-nanotubes measured at different laser powers of 0.2 and 2.5 mW.

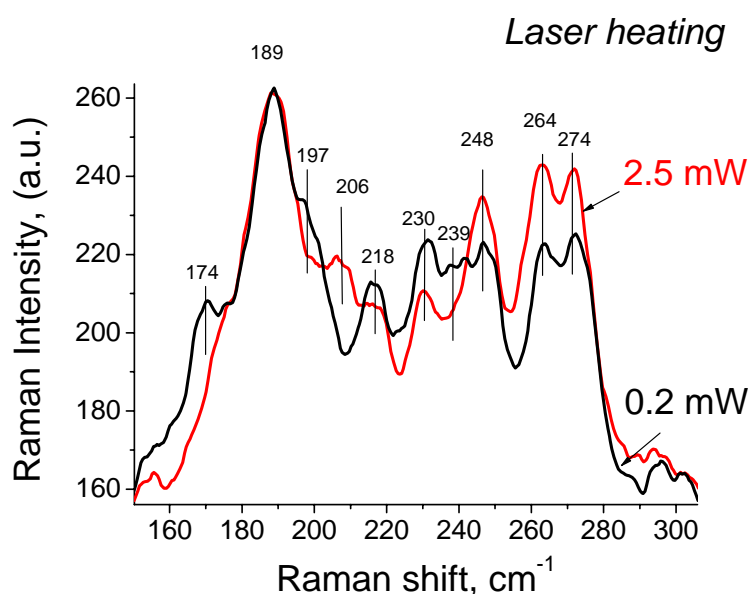


**Figure 6.5** Low frequency Raman spectra of the *HipCo*-samples. The spectra were measured at different laser beam power: 0.2 mW and 2.5 mW. At the laser powers  $> 2.5$  mW the smallest nanotube (with  $d < 1$  nm) burn out.

Both spectra were normalized to the intensity of the RBM peak of the semiconducting nanotube (11, 7) ( $\omega_{\text{RBM}} = 189$   $\text{cm}^{-1}$ ) with known theoretical energy shift (see Fig. 6.1). In this way the thermal changes in the Raman peak intensities appear more obvious. The intensity for some peaks (248, 264 and 274  $\text{cm}^{-1}$ ) grows with increasing of the laser power while for the others (218, 230 and 239  $\text{cm}^{-1}$ ) it decreases. The explanation is given by the plot for the energy down-shifts caused by bundling (Fig. 6.6) (see also Section 5.3).

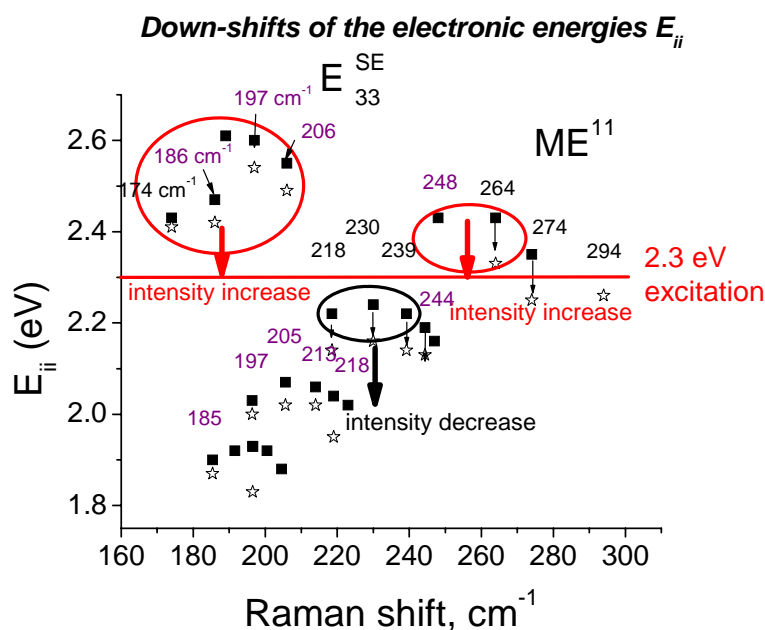


**Figure 6.6** Electronic transition energies of semiconducting and metallic tubes in single state (closed squares) and bundled state (open stars) [18]. The circles mark the energies of the tubes with similar temperature behaviour: those *above* the excitation energy line move to the resonance (their Raman intensities increase) and those *below* the excitation move out of the resonance (their Raman intensities decrease), compare Figs. 6.5 and 6.6.

Temperature leads to *similar* changes in the Raman intensities as bundling does! Analogous to bundling effects, the temperature influence on the electronic energies  $E_{ii}$  of metallic nanotubes can be seen from comparison between Figs. 6.5 and 6.6. The tubes with  $E_{ii}$  *above* the excitation energy at 2.3 eV (248, 264 and 274  $\text{cm}^{-1}$ ) move to the resonance with temperature increasing and therefore, exhibit increase in the peak intensity. At the same time, the tubes with the energies *below* the excitation energy (218, 230 and 239  $\text{cm}^{-1}$ ) move out of resonance and their peak intensities decrease. Such behaviour can be explained by the temperature-induced *energy down-shift*.

## 6.4 Summary

In this chapter the temperature dependence of the electronic transition energies of *semiconducting* nanotubes was studied theoretically and experimentally. The theoretical model for the temperature behaviour of the band gap [19] modified for higher electronic transitions was combined with the model for bundling effects developed in *Chapter 5*. The theoretical ratios of the Raman intensities calculated for two semiconducting nanotubes (11, 9) and (15, 2) within this combined model provide a very close agreement with temperature-dependent Raman experiment. Such an agreement confirms the consistency of the developed model which can be also applied for temperature estimation of the nanotube samples using Raman intensities. The temperature-dependent Raman scattering experiments on the *metallic* nanotubes demonstrate the *energy down-shift* caused by temperature.



# Chapter 7

## B- and N- Doping

In *Chapter 7* the experimental study of the newly-synthesised  $B_xN_yC_z$ -NTs and the other nanostructures is presented. *Chapter 7* contains the following parts:

- Motivation with the analysis of the theoretically predicted electronic properties of boron carbo-nitride nanostructures.
- Description of the production of single-walled and multi-walled  $B_xN_yC_z$  – nanostructures, HRTEM study of their morphology, interlayer stacking and the element composition ( $x, y, z$ ).
- Non-resonance Raman scattering on  $B_xN_yC_z$ -NTs having different  $x, y$ , and  $z$  element compositions; analysis of changes in the Raman spectra and the electronic band structure as a function of boron and nitrogen doping concentration  $x$  and  $y$ .
- Near infrared-visual-ultraviolet (NIR-vis-UV) absorption spectroscopy on the aqueous dispersions of  $B_xN_yC_z$ -NTs; analysis of changes in the electronic structure caused by B and N-doping comparing NIR-vis-UV spectra of  $B_xN_yC_z$ -NTs and CNTs.
- General conclusions about the methods of production and investigation of  $B_xN_yC_z$ -NTs and their electronic properties as a function of B and N-concentration.

### 7.1 Motivation

The field of nanotube science is represented by many exotic nanostructures made of carbon (CNT,  $CN_x$ ,  $BC_3$ ,  $B_xN_yC_z$ ), boron and nitride (BN), and composites of molybdenum ( $MoS_2$ ), vanadium ( $V_2O_5$ ), tungsten ( $WS_2$ ), etc. [77]. All these structures having different electronic properties were expected to be useful for nanoelectronics applications.

The electronic properties of single-walled carbon nanotubes depend strongly on their chiralities and diameters. The commonly obtained nanotube mixtures with mean diameters of 1.3 nm are mostly semiconducting (2/3 of all tubes) with band gaps of about 0.5 eV, or metallic (1/3 part).

BN-NTs represent a structural analogue of carbon tubes with quite different electronic properties. They are insulators with a large band gap (about 5.5 eV) of ionic origin, almost independent of chiralities, diameters and intertube interactions [20, 78]. The estimated band gap of  $BC_3$  nanotubes is about 0.5 eV [79], and the experimental data confirmed their semiconducting behavior [80].  $CN_x$  nanotubes were predicted [81] and confirmed [82] to be metallic.

Among these composite nanotubes,  $B_xN_yC_z$ -nanotubes play a special role due to their “tunable” electronic properties. The band gap energies of these nanotubes are not strongly dependent on the diameter and chirality. They show, however, essential changes for different atomic compositions [20 – 22], which hints at a way to control their electronic properties.

There are many experimental methods of investigating the electronic properties of nanostructures. Photoluminescence spectroscopy (PL) and Near-IR-vis-UV absorption on CNTs give directly the band gap values  $E_{11}^{SE}$  of semiconducting nanotubes (PL) and the electronic transition energies  $E_{11}^{SE}$ ,  $E_{22}^{SE}$ ,  $E_{33}^{SE}$  and  $E_{11}^{ME}$  (NIR-vis-UV).

Raman scattering is an indirect method to study both electronic and vibrational properties of carbon nanotubes. Raman response from CNTs is very strong, highly resonant and gives diameters and the electronic transition energies of metallic and semiconducting CNTs. This method, however, does not work that well for BN- and  $B_xN_yC_z$  nanotubes.

Raman spectra of pure BN-nanotubes having a large band gap  $\approx 5$  eV ( $> E_{exc}$ ) [89] are much weaker compared to CNTs due to the absence of the resonance enhancement of Raman scattering.

The electronic structure of  $B_xN_yC_z$ -NTs was analysed in Section 3.4. It was shown [22] that doping with B and N shifts the electronic energy bands of pure CNTs and broadens the van Hove singularity (vHs) peaks in the electronic density of states (DOS).  $B_xN_yC_z$ -nanotubes can have band gaps of 0 – 5 eV (Fig. 3.14) depending on the B- and N-concentration. Their electronic transitions are thus accessible with  $E_{exc}$  of the Raman experiment. However, the sharp vHs peaks disappear with doping making the Raman scattering non-resonant. The Raman signal from  $B_xN_yC_z$ -NTs loses intensity and becomes structureless depending on the doping concentration. Therefore, non-resonance Raman spectra of  $B_xN_yC_z$ -NTs characterize the tube composition ( $x, y, z$ ). Non-resonance Raman scattering is also non-selective for a certain nanotube diameter (compared to pure CNTs), i.e. for  $B_xN_yC_z$ -NTs the simultaneous excitation of many tubes with different diameters is possible.

Some Raman results on BC, CN and  $B_xN_yC_z$  nanotubes can be found in literature [82, 84, 90 – 94]. The main change in those Raman spectra compared to the spectra of CNTs was the growth of the D-mode responsible for the scattering on defects. Some work has already been done on correlations between the composition of  $B_xN_yC_z$ -NTs and their Raman peak intensities [90, 94, 95]. However, the dependence of the RBM on the doping concentration was not studied so far.

In this chapter a Raman study (as well as PL and NIR-vis-UV absorption) on  $B_xN_yC_z$ -NTs with different element compositions ( $x, y, z$ ) is presented. The method developed for the synthesis of  $B_xN_yC_z$ -NTs allows the preparation of nanotubes with various B and N concentrations up to 100% (pure BN-NTs). The correlation between doping concentrations and Raman spectra was studied combining the energy dispersive X-ray analysis (EDX) with Raman spectroscopy. HRTEM study gives additional information about the nanotube morphology and interlayer stacking.

## 7.2 Material preparation

$B_xN_yC_z$ -nanotubes of different compositions and morphologies can be produced by various preparation methods such as substitution reaction, arc-discharge, laser ablation, chemical vapour deposition, and pyrolysis [80, 83 – 88]. In this work  $B_xN_yC_z$ -NTs have been synthesized following the procedure of Golberg *et al.* [83] which was modified to reach better purity of the material.

$B_xN_yC_z$ -NTs and BN-NTs were produced in a substitution reaction between single-walled *NiCo*-CNTs and boric acid  $H_3BO_3$  in  $NH_3$  atmosphere. *NiCo*-CNTs which serve as starting materials in the reaction were produced by pulsed laser vaporization (PLV) of carbon targets [58]. They are defect-free nanotubes with a diameter distribution [1.0 – 1.5 nm], peaked at  $\approx 1.3$  nm.

For the synthesis of  $B_xN_yC_z$ -NTs two kinds of CNTs were used as templates: (1) as-prepared single-walled CNTs (black powders); (2) bucky papers (of about 50-100  $\mu m$  thickness) produced by a treatment of as-prepared CNTs with boiling sulphuric acid, filtration and drying [96]. The acid treatment removes most of the Ni/Co catalyst and amorphous carbon particles, but causes numerous structural defects in CNTs. These defects are apparently responsible for production of  $B_xN_yC_z$ -NTs with higher B-, N-concentrations compared to those produced from as-prepared CNTs.

Figure 7.1 shows the experimental set-up for the  $B_xN_yC_z$ - and BN-NTs synthesis.

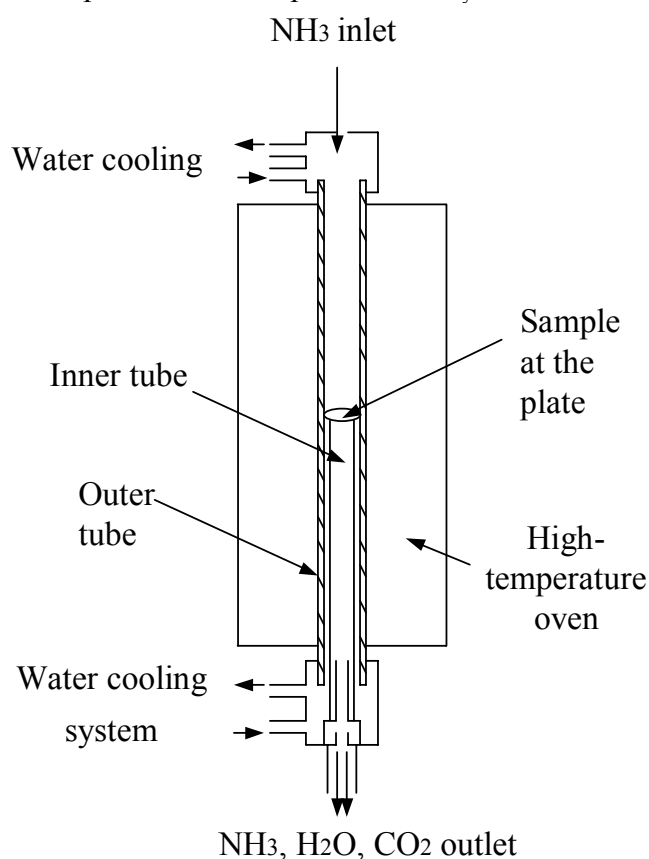
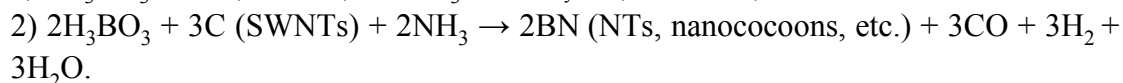


**Figure 7.1.** Schematics of the high temperature oven used for the  $B_xN_yC_z$ -NTs synthesis.

In the preparation procedure with as-prepared CNTs as templates the nanotubes were homogeneously mixed with  $H_3BO_3$  in stoichiometric 1:3 mole ratio and placed inside

the alumina tube within a high temperature oven. In the case of bucky papers small pieces of the material were placed on the top of  $\text{H}_3\text{BO}_3$  powder and covered with a platinum grid. During the synthesis  $\text{NH}_3$  flows through the inner tube and induces two types of substitution reactions:



The process of the  $\text{B}_x\text{N}_y\text{C}_z$ -NTs formation from CNTs in  $\text{B}_2\text{O}_3$  vapour is believed to take place as a statistical process where oxygen oxidizes carbon atoms that leaves the structure as  $\text{CO}_2$  molecule and creates a hole in the nanotube shell. Then boron can be easily incorporated into that defect [97]. As-prepared CNTs need significantly higher temperatures ( $1300^\circ\text{C} - 1500^\circ\text{C}$ ) to reach high B- and N-doping compared to the bucky papers with structural defects. For the bucky-papers  $T = 1250^\circ\text{C}$  turned out to be sufficient for a complete transformation into BN-NTs.

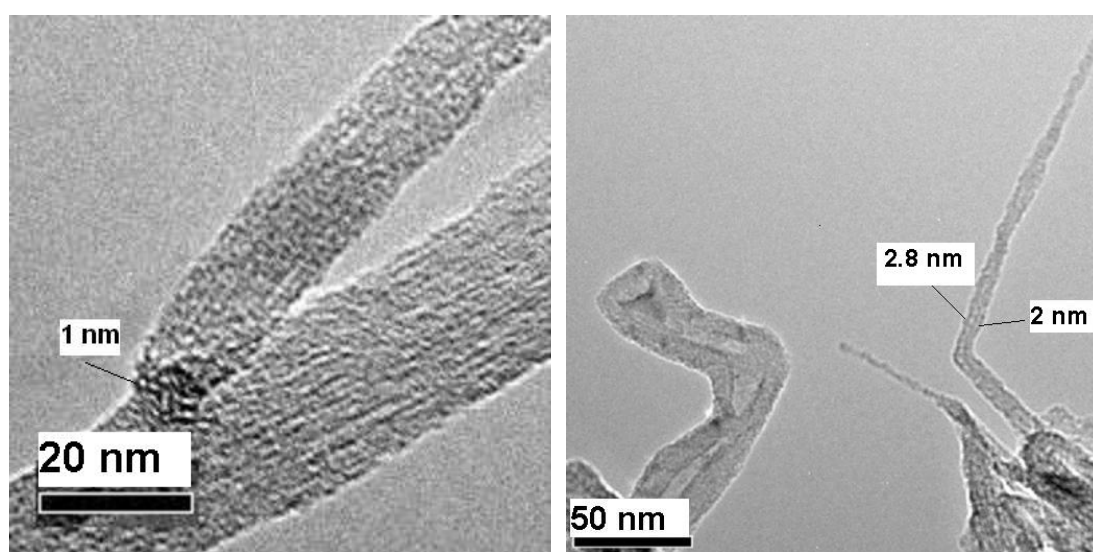
Under this thermo-chemical treatment, bucky papers did not lose their paper-like morphology, became thinner and change color to shades of grey, whereas the as-prepared CNTs turned into a fine grey powder. The samples can be studied *as-produced* in powders or dispersed in  $\text{D}_2\text{O}$  with addition of SDS or Ni/Cholate in order to destroy the big bundles and make the tubes individualized.

## 7.3 Experimental results

### 7.3.1 Morphology of the $B_xN_yC_z$ nanostructures: HRTEM study

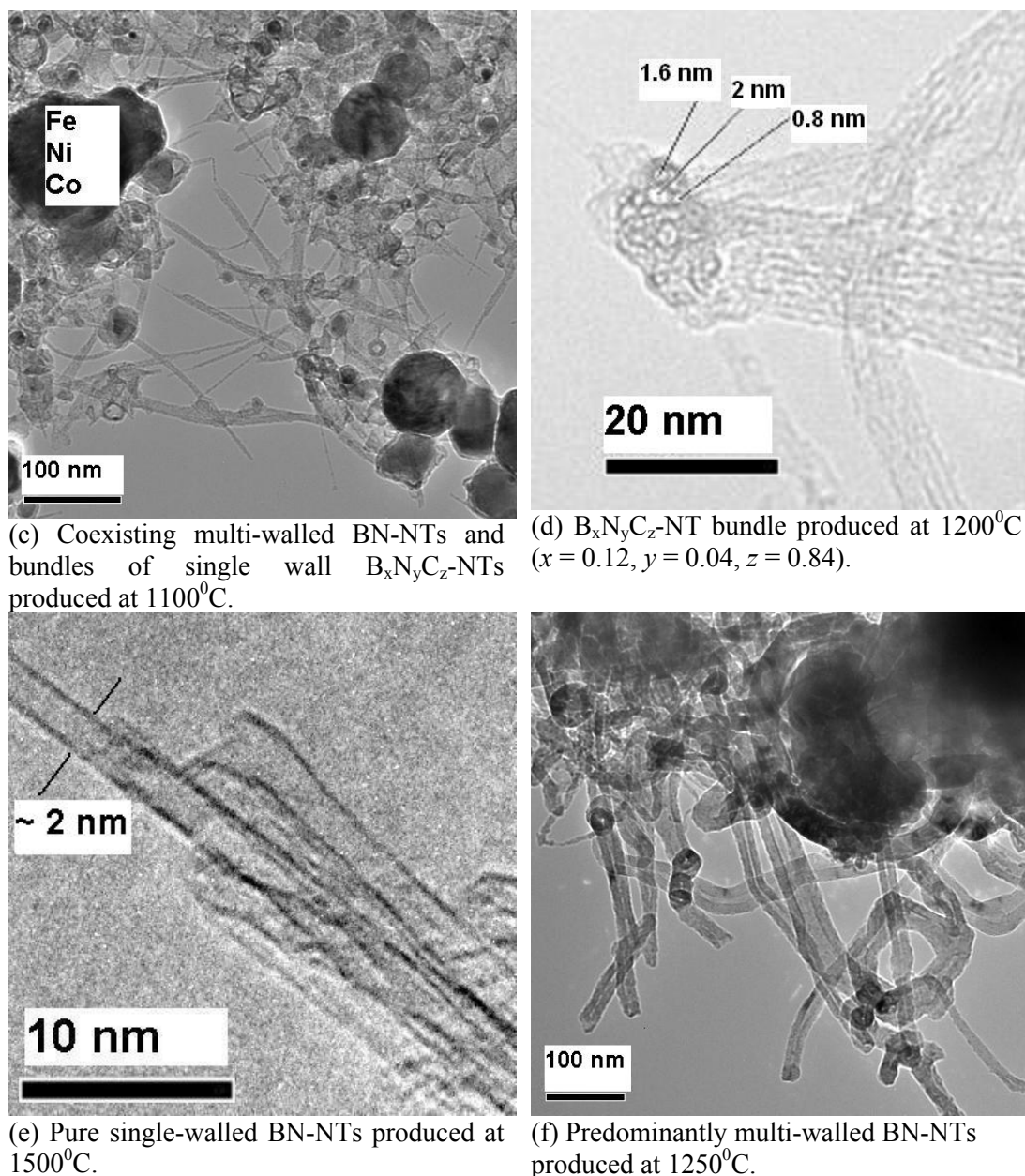
#### $B_xN_yC_z$ -nanotubes

In the course of this work a plenty of different nanostructures was synthesized varying temperature regimes and using as-prepared CNTs and bucky paper as templates. Among these structures are  $B_xN_yC_z$ -nanotubes with various B and N concentrations, pure BN-nanotubes (single-walled and multi-walled) of different lengths and diameters, exotic structures such as nanococoons and nanorods, etc. A higher purity of the  $B_xN_yC_z$ -NT material (free of bulk BN) was achieved using bucky-papers as templates. The B- and N-doping concentrations, in general depend on the synthesis temperature. The mean concentration of B and N in the  $B_xN_yC_z$ -NTs did not exceed  $x = 0.15$  and  $y = 0.13$  for samples synthesized at  $1100^\circ\text{C}$ , or  $x = 0.37$  and  $y = 0.28$  at  $1250^\circ\text{C}$ , respectively. At higher temperature, bucky papers burned out. In samples produced from bucky papers at  $1100^\circ\text{C}$  as well as  $1250^\circ\text{C}$ , a co-existence of pure BN-NTs and  $B_xN_yC_z$ -NTs with high concentrations of B and N and low concentration of C (up to  $x = 0.45$ ,  $y = 0.4$ ,  $z = 0.15$ ) was observed. In Figure 7.2 (g-f) high resolution transmission electron microscopy (HRTEM) images of some nanostructures are presented.



(a)  $B_xN_yC_z$ -NT bundles produced at  $1250^\circ\text{C}$  ( $x = 0.07$ ,  $y = 0.06$ ,  $z = 0.87$ ).

(b)  $B_xN_yC_z$ -NTs produced at  $1250^\circ\text{C}$  ( $x = 0.24$ ,  $y = 0.22$ ,  $z = 0.54$ ) and multi-walled BN-NT with closed tip.



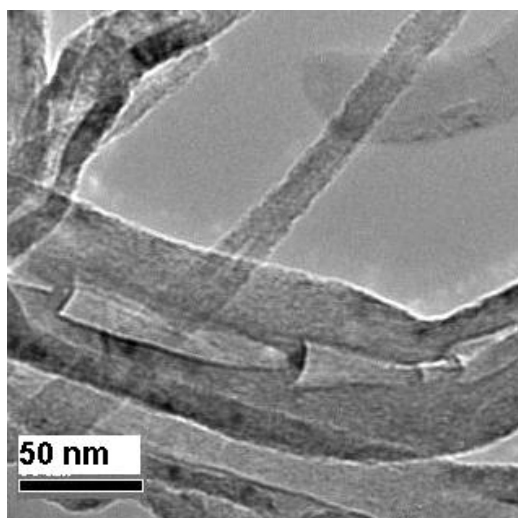
**Figure 7.2.** HRTEM images of the nanostructures synthesized under different temperatures regimes.

Figure 7.2 (a) shows typical bundles of  $B_xN_yC_z$ -NTs with an average element composition  $x = 0.07, y = 0.06, z = 0.87$ . Figure 7.2 (b, c) show the co-existence of multi-wall BN - NT with bundles of single-wall  $B_xN_yC_z$ -NTs; (f) shows an area with mostly multi-wall BN-NTs produces at 1250°C. The black particles in the mixture are catalysts (Ni, Co, Fe). The original CNTs had diameters ranging from 1 to 1.5 nm with a mean value of 1.3 nm. Bundles of slightly doped  $B_xN_yC_z$ -NTs look very similar to those of pure CNTs (Fig. 7.2, a, d). At higher B, N concentrations, the diameters of some tubes increased up to 2.8 nm (Fig.7.2, b). This could be explained by the formation of structural defects with open bonds [83]. In the reaction between CNTs, boric oxide and  $NH_3$  strongly damaged tube shells may combine to form a new nanotube with a larger diameter. This is not the case for nanotubes inside the big bundles (Fig.7.2, a). At high temperature, nanotube ropes tend to be transformed into

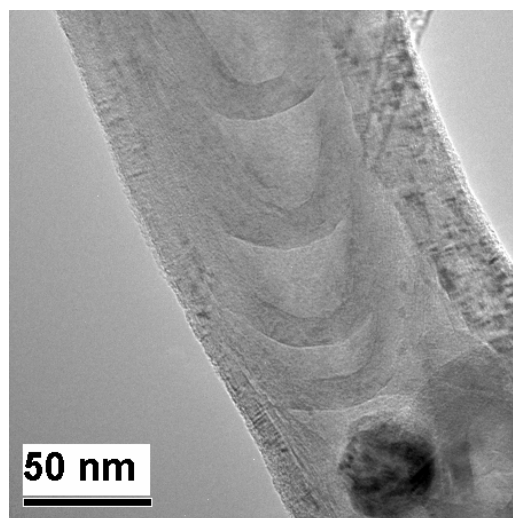
multi-walled nanotubes. Figure 7.2 (b) shows the co-existence of such multi-walled BN-NT and highly doped  $B_xN_yC_z$ -NT rope ( $x = 0.24, y = 0.22, z = 0.54$ ).

### ***Multi-walled BN- nanococoons, nanorods, and bamboo-like structures***

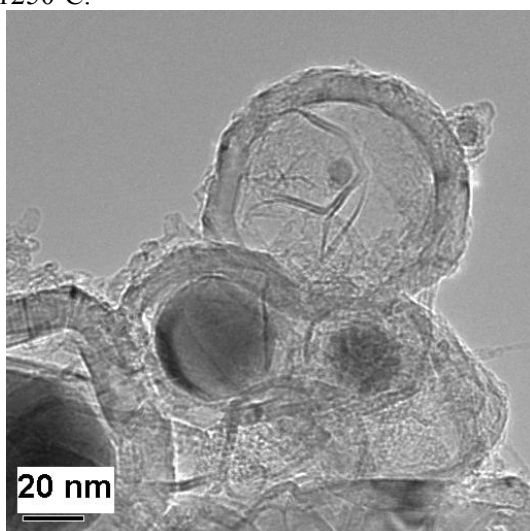
Apart from  $B_xN_yC_z$ -NTs of different  $x, y, z$  compositions many exotic structures were also synthesized. Among them are the bamboo-like BN-nanotubes (Fig. 7.3, a) and multiwalled BN-NTs with closed inner shells (Fig. 7.3, b), BN-nanococoons either empty or filled with metal particles or hexagonal BN (Fig. 7.3, c, e), nanopolyhedrons (Fig. 7.3, d), and many others.



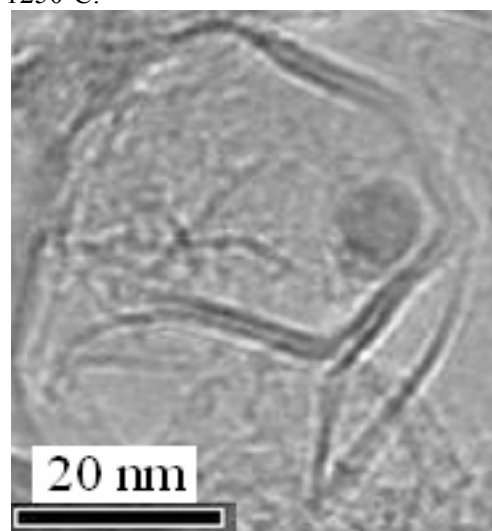
(a) Multi-walled BN-NTs produced at 1250°C.



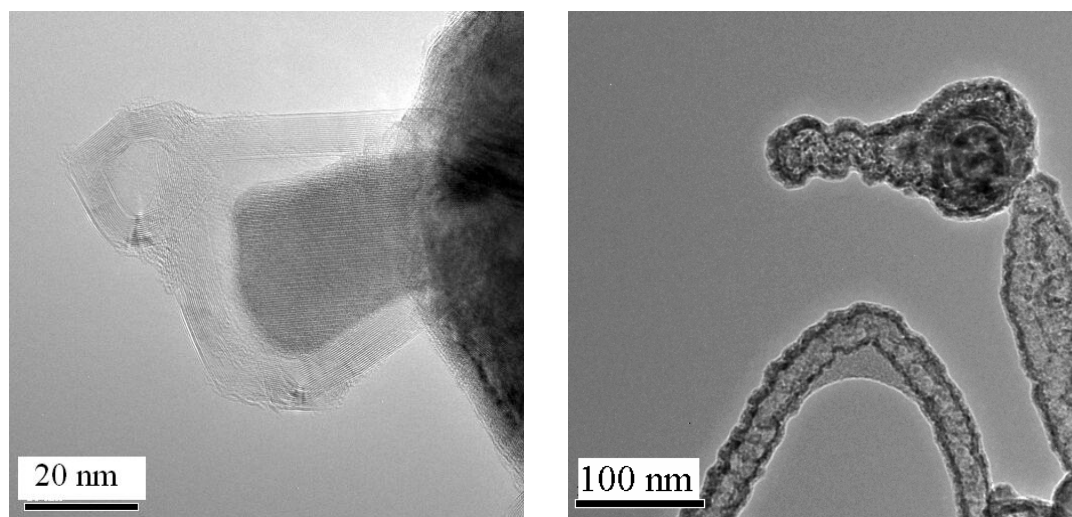
(b) Multi-walled BN-NT produced at 1250°C.



(c) BN-nanococoons (empty and filled with metal particles) produced at 1250°C.



(d) Closed BN-parallelepiped with hexagonal cross-section produced at 1250°C.

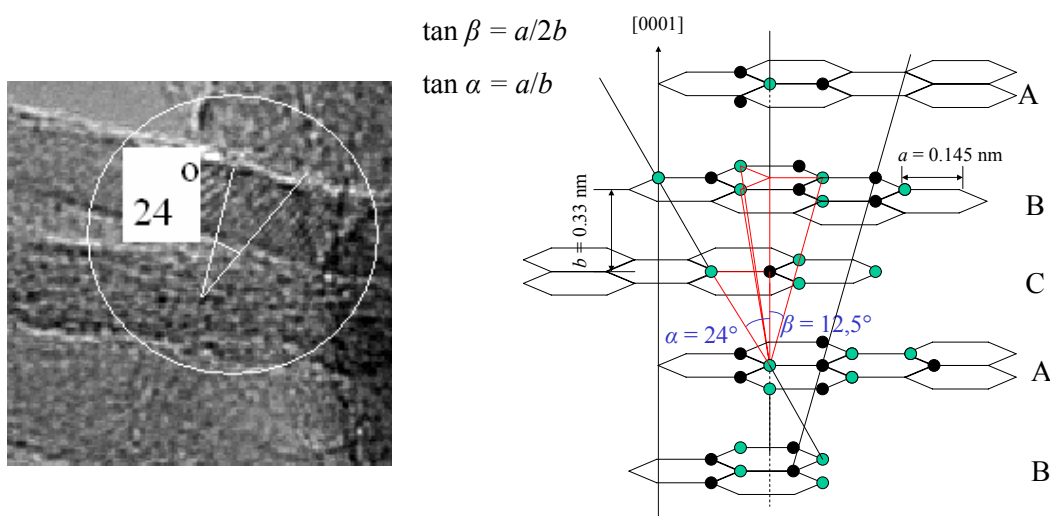


(e) Closed hexagonal BN-shells filled with metal produced at 1500°C (f)  $B_2N_yC_z$ -NTs with distorted walls produced at 1200°C.

**Figure 7.3** HRTEM images of the  $B_xN_yC_z$ -nanostructures synthesized in a substitution reaction at different temperatures.

### Interlayer stacking

The structural peculiarities of the nanotubes are a very interesting topic to study with HRTEM. For multi-walled BN-NTs one can observe a different interplanar orientation of the BN-layers which can be either hexagonal AA...AA... or rhombohedral (ABC...ABC...) or simple (AB...AB...). In Fig.7.4 (a-g) three examples of the hexagonal, rhombohedral and AB interlayer stacking are presented. B and N atoms marked are shown in shades of grey inside the hexagonal BN-sheets. An atomically resolved HRTEM image reproduces B and N atoms aligned along the same direction as dark contrasts. The case of the rhombohedral stacking with the plane orientation  $24^\circ$  with respect to the BN-sheet is shown in Fig. (7.4, a, b). Figs. 7.4 (c, d) and (e, f) present the hexagonal and the simple AB...AB interlayer stacking together with sketches of corresponding orientation of the BN-sheets.



(a) rhombohedral

(b) rhombohedral ABC...ABC...

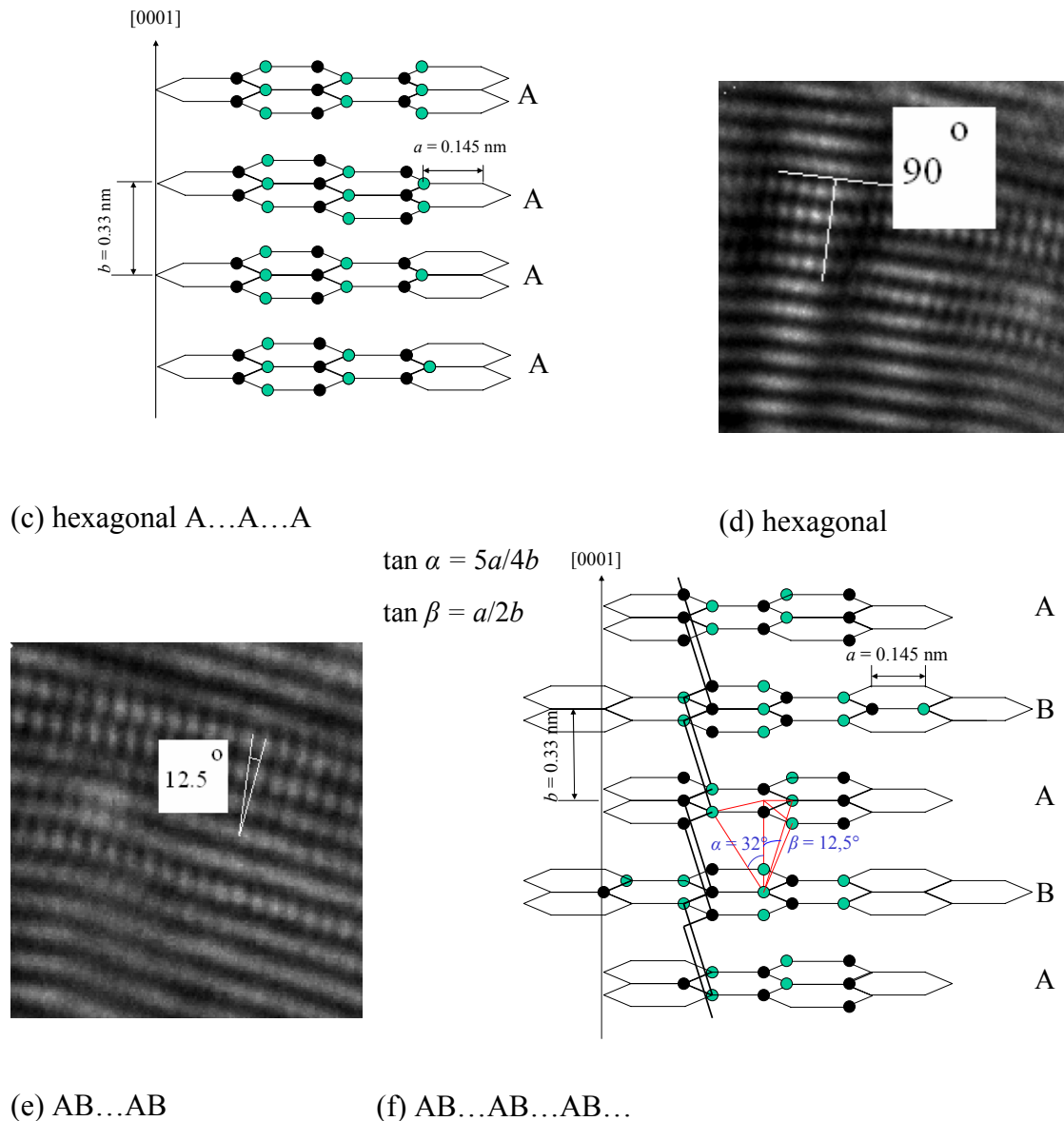


**Figure 7.4** Atomically resolved HRTEM images of different interlayer stacking for BN-sheets (a, d, and e) and sketches of corresponding orientation of the BN-planes (b, c, and f).

Analysis of the interlayer stacking provides information about the process of nanostructure formation, their layer homogeneity and structural order. Multi-walled structures with well-aligned defect-free BN-shells prevail at higher temperatures when the process of a BN-layer formation is completed. The materials produced at lower  $T$ , however, have a lot of structural defects since the transformation into BN-NTs is not yet completed. It leads to a high output of the structures with distorted walls similar to those shown as in Fig. 7.3 (f).

### 7.3.2 Element composition: EDX study

In order to obtain B and N concentrations for  $B_xN_yC_z$ -nanotubes one can use the energy dispersive X-ray analysis (EDX) combined with the high resolution transmission electron microscopy (HRTEM).

For the EDX element analysis of the  $B_xN_yC_z$ -materials a very small amount of the samples was placed onto standard gold grids (mesh 300) with markers which allowed selecting certain areas for the investigations. The electron beam can be focused onto a 1 nm-spot which allows determination the element composition of a certain nanotube. Figure 7.5 presents concentrations of B and N obtained by EDX for small ropes of  $B_xN_yC_z$ -NTs.

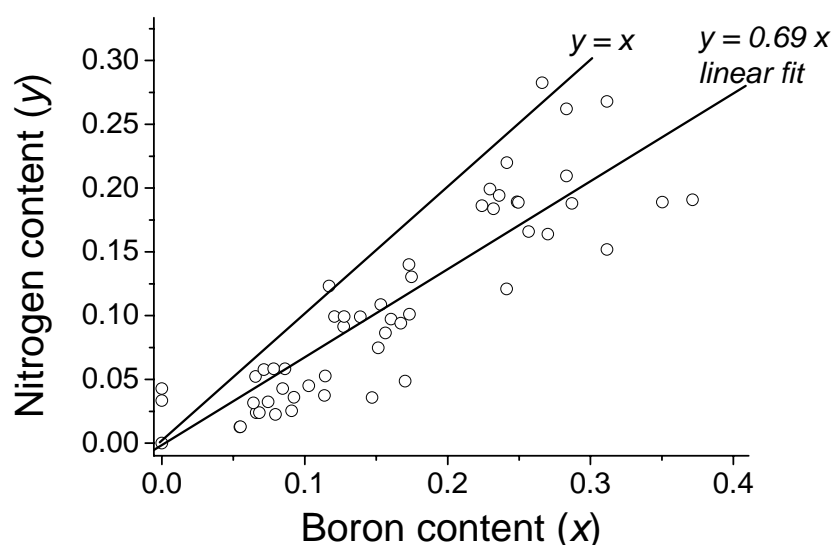


**Figure 7.5.** Concentrations of B ( $x$ ) and N ( $y$ ) obtained by the EDX method for small ropes of  $B_xN_yC_z$ -NTs.

In agreement with previous reports [79, 83, 97, 98] for all the  $B_xN_yC_z$ -NTs samples, the observed B-concentration  $x$  was a little higher than the N-concentration  $y$  except for some bundles with very low N content where B was not detectable. A linear fit  $y = 0.69x$  approximates this correlation between B ( $x$ ) and N ( $y$ ) concentration.

Concerning the possibility of the *surface deposition* of B and N atoms the following arguments can be presented.  $B_2O_3$  surface deposition is not considered to occur since in all EDX measurements a constant diffusive oxygen background was determined. Although N atoms may be adsorbed in between nanotube ropes, this possibility for measurements on single tubes and small bundles of 2 or 3 nanotubes can be excluded. Thus, the doped B and N atoms are believed to be integrated in the nanotube structure.

### 7.3.3 Non-resonant Raman spectroscopy on $B_xN_yC_z$ -NTs

#### *Samples*

The Raman study is performed at room temperature for the excitation energy  $E_{exc} = 2.3$  eV on *as-produced*  $B_xN_yC_z$ -NT powders. Even for the bulk samples the Raman response becomes very weak due to disappearance of the sharp resonance with

broad vHs peaks (Section 3.4). At very low concentrations of the material (for instance, in dispersions) the Raman spectra of  $B_xN_yC_z$ -NTs are not detectable at all. The bulk samples give thus an opportunity to obtain better signal/noise ratio. In that case, however, the Raman response is averaged for all the tubes inside the laser beam area of about  $1\ \mu\text{m}$ . Fortunately, the HRTEM and EDX study revealed that the areas of about  $1\ \mu\text{m}$  in the  $B_xN_yC_z$ -NTs bundles have more or less homogeneous doping within a variation  $\leq 0.05$  ( $x, y \pm 0.05$ ). Hence, a reasonable correlation can be expected between the average B- and N-doping ( $x$  and  $y$ ) and the measured Raman spectra.

Figure 7.6 presents the Raman spectra obtained from bundles of  $B_xN_yC_z$ -NTs with various average doping concentrations ( $x, y$ ) from 0 (pure CNTs) up to 0.6.

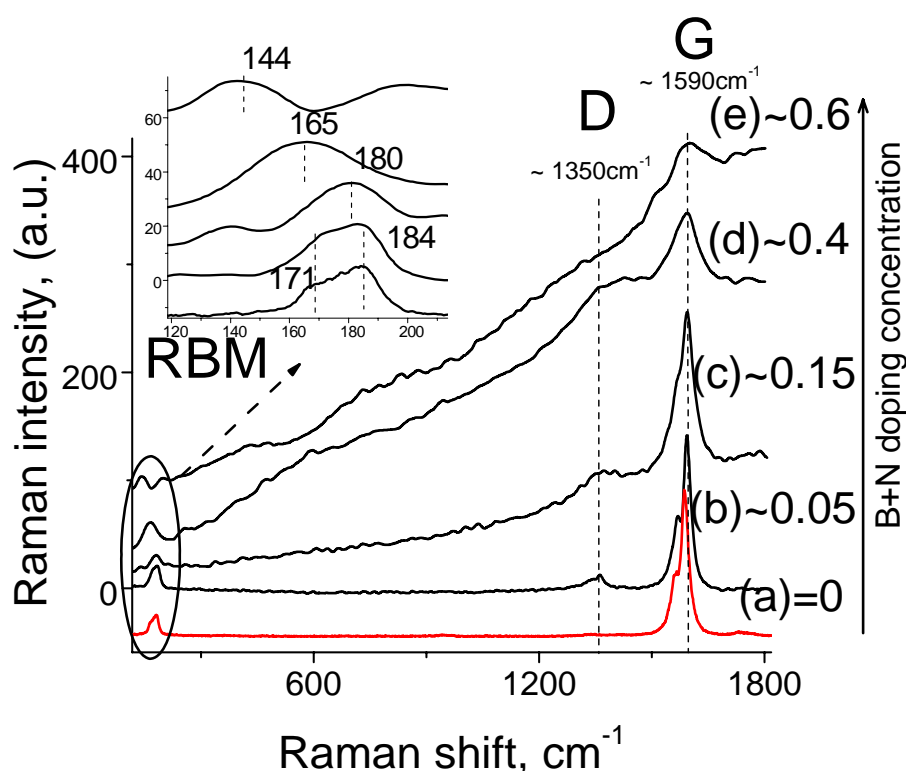


**Figure 7.6** Raman spectra of  $B_xN_yC_z$ -NTs with different boron- ( $x$ ) and nitrogen- ( $y$ ) concentrations from 0 (pure CNTs) up to 0.6.

The main changes in Raman spectra caused by B and N doping can be summarized as follows:

- the graphite-like G-mode becomes broader, loses its two-peak structure, its position shifts from  $\approx 1587\ \text{cm}^{-1}$  (for pure CNTs) to  $1594\ \text{cm}^{-1}$  (for doped  $B_xN_yC_z$ -NTs);
- the intensity of the defect-induced D-mode grows due to the increase of the number of defects (B and N atoms) in a hexagonal carbon framework;
- the luminescent background appears, probably, due to the BN-admixtures whose output increases at higher synthesis temperatures;
- RBM frequencies (see inset in Fig. 7.6), in general, decrease; their peaks become broader.

All these changes will be discussed in more detail in the following section.

### G-mode

The graphite-like G-mode or high energy mode (HEM) in CNTs is caused by the zone-center phonon excitation and usually consists of two mode frequencies with symmetries  $E_{1g}$  ( $\approx 1570 \text{ cm}^{-1}$ , full width at half maximum FWHM  $\approx 30 \text{ cm}^{-1}$ ) and  $E_{2g}$  ( $1580 - 1590 \text{ cm}^{-1}$ , FWHM  $\approx 16 \text{ cm}^{-1}$ ). The origin of the G-mode in CNTs was discussed in Section 4.1.3 in more detail.

For the  $B_xN_yC_z$ -NTs samples the broadening of the G-mode correlates with B and N concentration inside a nanotube bundle. The reason for that can be the following. Doping by B and N atoms is expected to form new chemical bonds such as B–N, B–C, and C–N [91, 94]. It leads to the local distortions in the graphite layers due to differences in atom masses, force constants and chemical bond lengths. Such a reduction of the crystal symmetry breaks down the selection rule  $k \approx 0$  (first order process) or the  $k_1 \pm k_2 \approx 0$  (second order process) and gives rise to other phonon frequencies near the main peak. Therefore, in spectra of  $B_xN_yC_z$ -NTs the broadening of the G-mode is observed. For pure CNTs the value of the full width at half maximum change FWHM  $\approx 30 \text{ cm}^{-1}$ ; for the doping concentration  $(x + y) \approx 0.25$  FWHM  $\approx 70 \text{ cm}^{-1}$  (Fig. 7.6).

There is also a small shift of the G-peak frequency for  $B_xN_yC_z$ -NTs. For pure CNTs its position is  $\approx 1587 \text{ cm}^{-1}$ , for  $B_xN_yC_z$ -NTs it is  $\approx 1594 \text{ cm}^{-1}$ . The explanations for such a shift could be the following:

- (i) the incorporation of B and N atoms which changes the lattice parameters (masses) of the carbon framework and leads to the frequency up-shift since boron atoms are lighter than carbon atoms (in  $B_xN_yC_z$ -NTs the concentration of light boron usually is higher than that of heavier nitrogen);
- (ii) presence of the *thermal shifts* of the frequencies due to the laser heating of the sample. Different thermal conductivities for CNTs and  $B_xN_yC_z$ -NTs lead to different local heating of the sample for the same laser power. Temperature dependence of  $\omega(T)$  for pure and doped nanotubes is also different.

Since the G-mode is an excitation-dependent mode and directly connected to the resonance phenomena in carbon nanotubes [13, 42, 95, 103] it can be used to point out changes in electronic structure of CNTs caused by B- and N- doping.

### D-mode

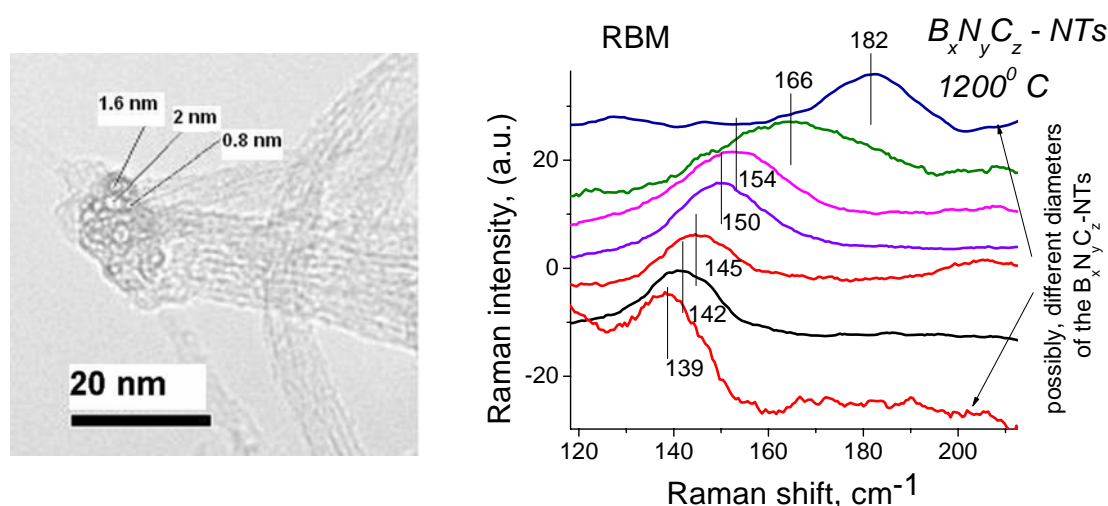
The D-mode ( $\approx 1350 \text{ cm}^{-1}$ ) is traditionally considered to be responsible for defects in the nanotube structure (voids, pentagon-heptagon pairs, kinks, incorporated atoms, admixtures) and finite size effects in CNTs, (i.e. continues nanotube length). D-mode appears due to the interaction of the *K*-point phonons with structural defects and demonstrates dependence on the excitation energy *via* the double-resonance scattering process [13, 95, 103]. It is known that the D-peak intensity in carbon-based materials is connected to the number of defects. The relative Raman peak intensities can be used for the determination of the crystallite size [99]. In CNTs the ratio between the second and the first order peak intensities  $I(D)/I(D^*)$  is found to be the value which is proportional to the defect concentration [42, 95, 103]. At the same time, the intensity ratio  $I(D)/I(G)$  used previously for the defect estimations in many publications [94, 100 – 102] can be applied only with a great caution since the G-mode itself depends on defects.

Fig.7.6 demonstrates the relative D-mode growth and broadening with respect to the G-mode and RBM. The second-order D\*-mode was experimentally inaccessible. The explanation of the D-mode broadening can be the same as for the G-mode: the break down of the selection rule  $k_1 \pm k_2 \approx 0$  (second order process) and the appearance of the additional peaks near the main peak. Finally, the D-mode (the ratio  $I(D)/I(D^*)$ ) can be used after the corresponding calibration for the estimation of B- and N-concentration in  $B_xN_yC_z$ -NTs.

### RBM

The B- and N- doping influence on the RBM frequencies manifests itself in a frequency decrease and peak broadening. The decrease of the RBM frequencies can be explained by the appearance of tubes with larger diameters (as in Figs. 7.2 b, d) due to collapse of several tubes with smaller diameters at high  $T$ .

The RBM broadening could be explained by the following arguments. According to the tight-binding calculations for  $B_xN_yC_z$ -NTs having different doping concentrations [22] the incorporation of B and N results in broadening of the vHS-peaks in the (DOS) function (Section 3.4). For the atomic concentrations of B and N ( $x + y$ ) ranging from 0.1 to 0.6 the sharp vHS-peaks disappear more and more (Fig. 3.14). At the same time, the energy separations between the van Hove singularities increase with increasing the B- and N- concentration and approaches the value of  $E_g \approx 4.5$  eV for pure BN-NTs. The concentrations accessible with Raman technique depend on the excitation energy, therefore only the tubes with the transition energies  $E_{ii} < E_{exc} = 2.3$  eV can contribute to the Raman spectra. By comparison with the tight-binding calculations [22] one can estimate this 'limit' concentration of B and N to be  $(x + y) \leq 0.74$ . It may cause *simultaneous excitation* of many tubes with different diameters and  $E_{ii}$ . In that case, however, the intensities of the Raman spectra become very weak and unstructured. In Figure 7.7 (b) the RBM frequencies obtained from the low-doped bundles similar to those in Fig.7.7 (a) are shown.



(a)

(b)

**Figure 7.7** (a) HRTEM image of the  $B_xN_yC_z$ -NT bundle produced at  $1200^\circ\text{C}$  with the mean element concentrations  $x = 0.12$ ,  $y = 0.04$ ,  $z = 0.84$ ; (b) The RBM frequencies obtained from the bundles similar to that in Fig. 7.7 (a).

For low doping concentrations ( $< 0.15$ ) the electronic transition energies of  $B_xN_yC_z$ -NT bundles are close to those of CNTs. The diameters, however, became larger during the synthesis process. Thus, in Fig. 7.7(b) one can see the RBM frequencies  $< 166 \text{ cm}^{-1}$  corresponding to the diameters of pure CNTs  $> 1.46 \text{ nm}$  with transition energies  $E_{ii}$  close to  $E_{exc} = 2.3 \text{ eV}$  (semiconducting branch  $E_{44}^{SE}$  in Fig. 3.12). It should be possible to see all those tubes in the same Raman spectrum only if they are all present inside a bundle within the laser beam (spot  $\approx 1 \mu$ ) (as in Fig. 7.7, a). The broad RBM peak centered at  $166 \text{ cm}^{-1}$  was obtained from such a bundle with tubes of different diameters. The other RBM frequencies relate to different places of the sample with tubes having either a narrower diameter distributions or  $E_{ii}$  far from  $E_{exc} = 2.3 \text{ eV}$ .

Finally, RBM is the most sensitive Raman mode immediately “feeling” any changes in the electronic properties of CNTs. These changes can be caused either by diameter growth or by B- and N- doping each of which influencing the band gap value and the electronic DOS function. The pure diameter growth (without doping) can change the transition energies taking the tube off the resonance with  $E_{exc}$ . In contrast, B- and N-doping can bring to resonance simultaneously many tubes with different diameters just because of the smearing out of the vHs peaks in DOS function. In this case, the intensity of the Raman signal decreases.

For high B- and N-doping concentrations electronic transition energies  $E_{ii}$  exceed  $E_{exc}$ . The intensity of the Raman signal decreases by orders of magnitude and the Raman spectra become hardly detectable. This limiting concentration was experimentally estimated to be of about 0.6. The theoretical value was predicted to be  $\approx 0.74$  (see Section 3.4).

### 7.3.4 Photoluminescent and NIR-vis-UV absorption spectroscopy on $B_xN_yC_z$ -NTs

Raman spectroscopy is an effective *indirect* technique for characterization of the nanotube electronic band structure since it is related to both vibrational and electronic properties of either CNTs or  $B_xN_yC_z$ -NTs. It needs, however, a reliable theoretical model connecting the experimental Raman features with the nanotube electronic energies  $E_{ii}$ , diameters  $d$  and structural  $(n, m)$  indices. Such a semi-empirical model exists for pure CNTs [6], namely, for the band gap energies  $E_{11}^{SE}$  of the semiconducting CNTs (Section 3.3). Also, for some semiconducting and metallic CNTs the higher energies  $E_{ii}$  were experimentally derived using the resonant Raman spectroscopy [18].

For  $B_xN_yC_z$ -NTs with different element compositions a similar assignment model is not available and, probably, not possible at all. The reason for that is a large experimental variation of the concentrations  $x, y, z$  and the non-resonant nature of the scattering process. At the moment non-resonant Raman spectroscopy on  $B_xN_yC_z$ -NTs can provide a comparative study only, and gives no accurate information about the electronic band structure of individual nanotubes.

In order to fill the gaps in the knowledge about the electronic structure of  $B_xN_yC_z$ -NTs the Near-Infrared-Visual-Ultraviolet absorption study (NIR-vis-UV) was carried out. NIR-vis-UV spectroscopy gives a *direct* information about the electronic interband transitions.

### Samples and experimental details

The bundling forces of all *as-produced*  $B_xN_yC_z$ -NTs are ionic forces interacting between polar B and N atoms. Therefore, the experiments on the de-bundling of  $B_xN_yC_z$ -NTs were not that efficient as for CNT bundles interacting with weak van der Waals forces. The bundles appeared to be quite stable against prolonged sonication during hours at high ultrasound powers.

Figure 7.6 (a, b) shows scanning electronic microscopy (SEM) images of the residuals deposited on the Si-wafer by spin-casting from the dispersion of  $B_xN_yC_z$ -NTs in SDBS/D<sub>2</sub>O. The dispersion was preliminary sonicated and centrifuged in order to break the big bundles and remove heavy particles (bulk BN, multi-walled BN-NTs, BN-nanococoons, etc) from the dispersion. The final dispersion contains a very low concentration of nanotubes which were not detectable with Raman scattering.

Fig. 7.6 shows a mixture of curved and knotted nanotube bundles covered with soap and ‘dirt’ of the BN-hexagonal origin. These could be the BN-nanococoons filled with metals, MWBN-NTs, etc. similar to the structures from Fig. 7.2 (c).

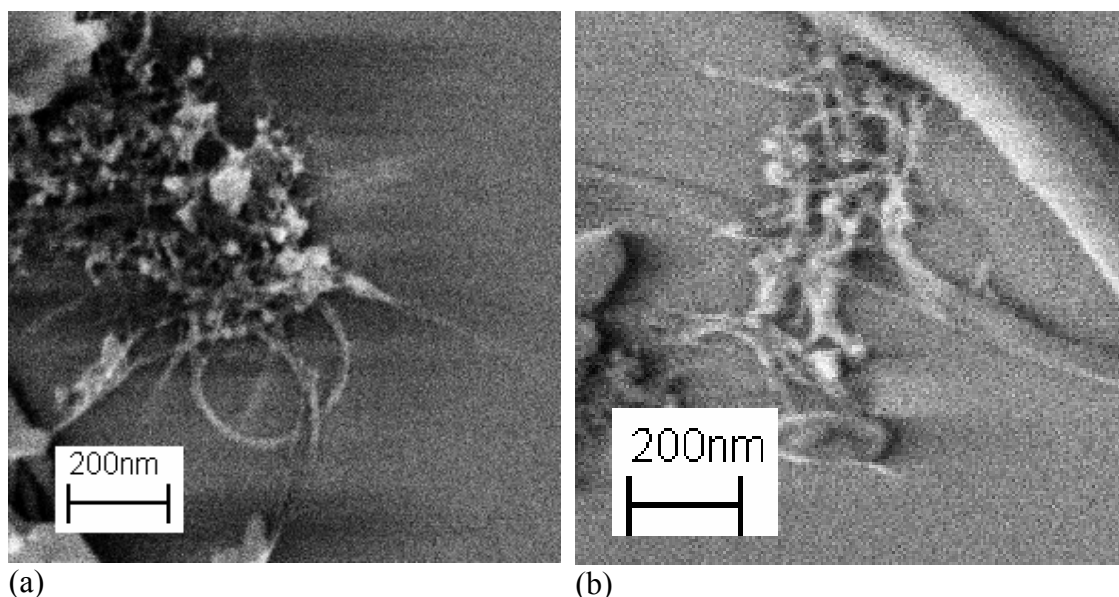


**Figure 7.6** SEM images of the residuals deposited onto the Si-wafer from the dispersion of  $B_xN_yC_z$ -NTs in SDBS/D<sub>2</sub>O after sonication and centrifugation.

The strong ionic interaction in  $B_xN_yC_z$ -NTs bundles mentioned above does not allow the separation of nanotubes from bundles to study them individually. Therefore, the photoluminescence (PL) study of the dispersions of *bundled*  $B_xN_yC_z$ -NTs gave no result. It is known that the PL signal appears only in the dispersions of well-individualized tubes having no structural defects. Thus, in bundled samples of CNTs no PL was detected.

At the same time, the PL study on *as-grown well-aligned arrays of single*  $B_xN_yC_z$ -Ts [92, 93, 105], has shown intense and stable PL bands in both blue-violet (3.14 – 2.55 eV) and yellow - green (2.13 – 2.34 eV) spectral regions. Their emission bands appeared to be broad, unstructured and adjustable by variation of the B- and N-concentration.

$B_xN_yC_z$ -NTs investigated in the present work differ substantially from those well-aligned array. Since they produced by the substitution reaction from highly interacting CNTs they stuck together due to strong ionic forces and have neither well-graphitized

walls nor homogenous distribution of the B and N. The observation of the PL on the dispersions of  $B_xN_yC_z$ -NTs produced in this way was not possible.

Changes in the electronic structure of  $B_xN_yC_z$ -NTs caused by B- and N-incorporation must be reflected in their NIR-vis-UV absorption spectra. Therefore, NIR-vis-UV absorption seems to be a more convenient way giving the electronic interband transitions of either metallic or semiconducting nanotubes in a wide spectral range (350 nm to 1850 nm) covering energies  $E_{11}^{SE}$ ,  $E_{22}^{SE}$ , and  $E_{11}^{ME}$  of pure CNTs.

Fig. 7.7 presents the NIR-vis-UV absorption spectra of the dispersions  $B_xN_yC_z$ -NTs in  $D_2O$ /SDBS (three middle curves) combined with the spectra from *NiCo*-CNTs in  $D_2O$ /SDBS (upper curve) for comparison. The spectrum of the pure solvent  $D_2O$ /SDBS is also presented (two lowest curves). All the spectra are normalized on its intensity: the original spectrum of CNTs was about 10 times higher than others; the peaks from  $D_2O$ /SDBS were negligibly small in the original CNTs spectrum.

The absorption peaks corresponding to  $D_2O$ /SDBS are centered at  $\approx 1320$  nm, 1411, 1512 and 1670 nm. The broad bands  $E_{11}^{SE}$ ,  $E_{22}^{SE}$ , and  $E_{11}^{ME}$  with several poorly resolved individual peaks correspond to the electronic transitions of pure *NiCo*-CNTs present in the dispersion.

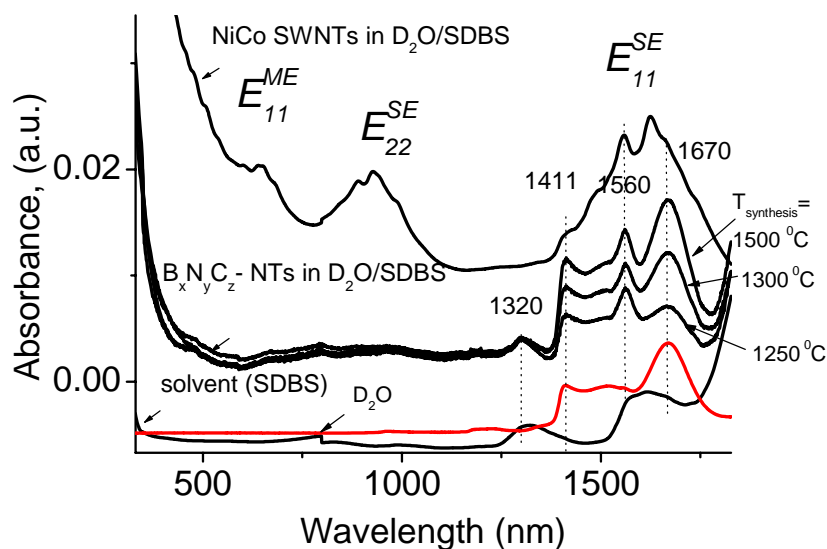


**Figure 7.7** NIR-vis-UV spectra of the dispersion of CNTs in  $D_2O$ /SDBS (the upper curve), the dispersions of  $B_xN_yC_z$ -NTs produced at different temperatures in  $D_2O$ /SDBS (three middle curves), and the solution  $D_2O$ /SDBS (two lower curves).

It is clearly seen that the absorption spectra of  $B_xN_yC_z$ -NTs dispersions (three middle spectra) in a given scale mostly reflect intense peaks of the solvent  $D_2O$ /SDBS except for one peak at  $\approx 1560$  nm ( $\approx 0.8$  eV) similar to that appearing from the band gap electronic transitions  $E_{11}^{SE}$  of a certain pure CNT. If one zooms in the spectral region  $\approx 500 - 1100$  nm which is free from the solvent features, the resolved absorption spectra of  $B_xN_yC_z$ -NTs will appear in more detail (Fig. 7.8).

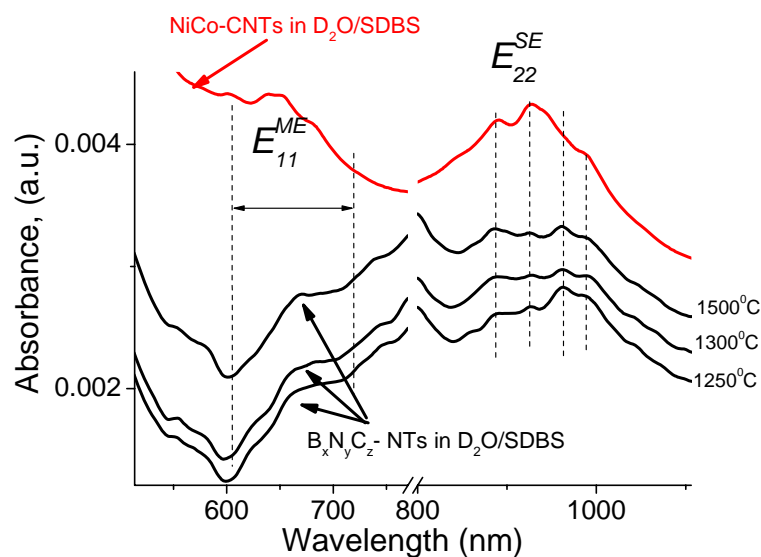


**Figure 7.8** NIR-vis-UV spectra of the dispersion of CNTs in  $D_2O/SDBS$  (the upper curve), and the dispersions of  $B_xN_yC_z$ -NTs with different  $x, y, z$  compositions in  $D_2O/SDBS$  (four lower curves) in the spectral range of 500 – 1100 nm.

The four lower spectra correspond to four  $B_xN_yC_z$ -NTs samples produced at different temperatures (1250, 1300 and 1500 $^{\circ}C$ ). They have various mean B and N concentrations. The absorption bands from different samples of  $B_xN_yC_z$ -NTs in Fig. 7.8 are identical and very similar to those of pure CNTs. They appear from slightly-doped individual  $B_xN_yC_z$ -NTs ( $(x + y) < 0.1$ ) present in the dispersion. The intensity of these peaks is low due to the very low concentration of  $B_xN_yC_z$ -NTs. The highly doped  $B_xN_yC_z$ -NTs (with  $(x + y) > 0.1$ ) can contribute to the spectrum as well. They should give the unstructured broad bands. The ultra-violet range  $> 4$  eV ( $< 300$  nm) where pure BN-NTs have their electronic transitions was not experimentally accessible.

To conclude, the electronic band structure of  $B_xN_yC_z$ -NTs was studied with NIR-vis-UV absorption method. The success of the experiment depends on the degree of tube individualization in dispersion.  $B_xN_yC_z$ -NTs appeared to be stuck into bundles due to the ionic B–N bridges between them. The method of ultrasonication does not efficiently break the bundles, and the following centrifugation removes heavy ropes of highly doped  $B_xN_yC_z$ -NTs from the dispersion. The final dispersion has a very low concentration of tubes giving a weak absorption signal. This signal looks very similar to that of CNTs, probably because of low B- and N- doping concentrations of tubes left in the dispersion.  $B_xN_yC_z$ -NTs produced from the bundled CNT-templates in a substitution reaction are not appropriate objects for the NIR-vis-UV absorption spectroscopy as well as PL study.

## 7.4 Summary

In this chapter the experience of the synthesis of  $B_xN_yC_z$ -nanostructures, their morphology and the element composition are presented. The electronic properties of the  $B_xN_yC_z$ -NTs as a function of the B- and N-doping were studied with the Raman scattering technique and the NIR-vis-UV absorption. It was shown that the electronic

structure of  $B_xN_yC_z$ -NTs depends substantially on the nanotube composition  $x$ ,  $y$ ,  $z$  and can vary from metallic to insulating. B- and N-doping affects not only the electronic transition values but also the DOS function broadening the vHs peaks for both metallic and semiconducting CNTs. Such a broadening makes Raman scattering on  $B_xN_yC_z$ -NTs non-resonant and structureless for high B and N concentrations.  $B_xN_yC_z$ -NTs with  $(x + y) > 0.74$  do not contribute the Raman spectrum with  $E_{\text{exc}} = 2.3$  eV since their band gap values exceed 2.3 eV.

# Chapter 8

## Conclusions

This work focuses on how the electronic properties of carbon nanotubes are affected by tube-tube interaction, by temperature, and by doping with different atoms.

These effects were studied with Resonance Raman scattering (RRS) - a unique technique providing information about both vibrational and electronic properties of CNTs. The one-dimensional structure of carbon nanotubes leads to sharp singularities in the electronic density of states. If the energy of excitation is close or even corresponds to the energy difference between such singularities, the Raman response becomes very strong. Therefore, in Raman spectra of CNTs one detects the peaks predominantly from those tubes whose electronic transition energies are in resonance with the incoming light. The resonance conditions have, on the other hand, a certain width (in general of about 100 meV). By scanning this range with changing excitation energies one can obtain the maximum Raman response, which in turn corresponds to the exact coincidence of the excitation energy with the electronic transition energy. Thus, the RRS technique allows obtaining the electronic transition energies of CNTs simply by analyzing the intensities of the Raman peaks. If some factor, such as tube-tube interaction, temperature, or doping, modifies the electronic structure of CNTs it will be immediately reflected in their resonance Raman spectra.

In this work the tube-tube interaction was investigated by RRS combined with High Resolution Transmission Electron Microscopy (HRTEM). The relative intensities of the Raman peaks from an ensemble of CNTs in a bundle give the information about the changes in the electronic band structure caused by tube-tube interaction. At the same time, the HRTEM images provide information about the size of precisely those nanotube bundles that were investigated by RRS.

With this combined study of the present work it was possible to establish a correlation between the relative Raman intensities of CNTs and the bundle size. This correlation is very useful for the estimation, for instance, changes in the band gap values of semiconducting CNTs depending on the number of tubes in a bundle – and thus, in turn, their light emitting characteristics. And vice versa, one can study the tube-tube interaction by analyzing the Raman intensities of bundles with different characteristics.

A phenomenological model was developed in order to describe tube-tube interaction simply by measuring the intensities of the Raman spectra at fixed excitation energy. Within this model, Raman intensities are calculated for any intermediate degree of tube bundling using the parameters available from the literature for the electronic energy shifts and Raman resonance windows of both single and strongly interacting CNTs.

The model was tested for many ensembles of CNTs having a broad diameter distribution from 0.8 nm to 1.5 nm. Even for the samples containing an inhomogeneous distribution of many tubes, the general tendency was clearly seen: changes of the Raman intensities reflect the shifts of the electronic transition energies. For samples containing only two kinds of “active-in-Raman” nanotubes the

correspondence between the calculated and experimental Raman intensities appeared to be perfect. In this way, the correlation between electron energy shifts and bundle size was estimated within the theoretical uncertainty of about 12%.

This simple model also allows revealing the electronic energy changes induced by temperature. The good agreement between the calculated Raman intensities and the experimental Raman intensities measured at different temperatures confirmed the reliability of the developed method.

In general, the method does have some restrictions. For example, in the calculation of the Raman intensities the model does not take into account the individual matrix elements of electron-phonon interaction, which may vary significantly for nanotubes belonging to different families  $\nu = \text{Mod}[(n-m), 3]$ . In that case more advanced theoretical models would have to be developed.

A large part of this work was devoted to the synthesis of new nano-materials. A number of boron carbo-nitride derivatives such as  $B_xN_yC_z$ -NTs, BN-NTs, BN-nanococoons, etc. have been produced in a substitution reaction between the carbon nanotubes and boric acid in ammonia atmosphere. The experience gained on the methods of synthesis is also presented in this work.

The variation of the temperature regimes and gases (either ammonia or nitrogen) results in different output products. Increasing the synthesis temperature from 1100<sup>0</sup>C to 1300<sup>0</sup>C leads to an increase of the mean (B + N) doping concentrations from 0.1 up to 0.6. Higher temperatures ( $\approx 1500^0$ C) result in complete substitution of carbon atoms by B and N in a hexagonal lattice giving rise to single- and multi-walled BN-NTs, BN-nanococoons and other BN-materials.

It is known from the literature that BN-based nano-objects, particularly BN-NTs, show insulating properties with a large band gap of about 4.5 eV. This makes their interband electronic transitions not accessible with excitations in the visible range (from 1.7 eV to 3 eV). Raman scattering on BN-NTs, therefore loses its resonance character despite the presence of the sharp singularities in the electronic density of states (DOS).

$B_xN_yC_z$ -NTs are intermediate objects between pure CNTs and fully substituted BN-NTs, and their electronic properties are predicted to vary from metallic to insulating depending on the doping concentration of B and N atoms. Doping, however, was theoretically predicted to broaden the sharp singularities in the electronic DOS. Due to the smearing out of the singularities the Raman scattering becomes non-resonant and is no longer specific to singular types of tubes. The same laser photon energy can excite simultaneously many different  $B_xN_yC_z$ -NTs with band gaps less than  $E_{\text{exc}}$ .

In the frame of the present work  $B_xN_yC_z$ -NTs with various element compositions were synthesized and studied with RRS and EDX (Energy Dispersive X-ray Analysis, giving the B and N content). The highest doping concentration of (B + N) for  $B_xN_yC_z$ -NTs contributing to the Raman spectra (with excitation energy 2.3 eV) was experimentally estimated to be  $\approx 0.6$ . All these tubes were semiconducting with electronic transition energies that do not exceed 2.3 eV.

The Raman spectra for  $B_xN_yC_z$ -NTs with (B + N) concentrations from 0.05 up to 0.6 are also presented. For highly doped (B + N > 0.6) nanotubes the Raman peaks becomes unstructured and have much lower intensity.

The electronic properties of  $B_xN_yC_z$ -NTs were investigated with Near-Infrared-visual-Ultraviolet absorption (NIR-vis-UV) and Photoluminescence (PL) spectroscopy. For these studies, aqueous dispersions of  $B_xN_yC_z$ -NTs with addition of a surfactant were prepared. However,  $B_xN_yC_z$ -NTs that had been expected to become individualized inside the surfactant micelles after sonication turned out to be strongly bound by ionic forces within the bundles. As a result, it was not possible to investigate the characteristics of individual tubes.  $B_xN_yC_z$ -NTs synthesized in a substitution reaction from CNT powders are not appropriate materials for producing dispersions from them.

In summary, factors such as tube-tube interaction, temperature, as well as B and N-doping substantially influence the electronic properties of CNTs. This influence is estimated to shift the electronic transition energies  $E_{ii}$  of CNTs as follows:

- strong tube-tube interaction decreases the energies  $E_{ii}$  of both metallic and semiconducting CNTs by 50 meV – 100 meV depending on the type of tube;
- increasing temperature decreases the energies  $E_{ii}$  of both metallic and semiconducting CNTs by 0.13 meV/K – 0.2 meV/K depending on the type of tube;
- B- and N-doping in general increases the energies  $E_{ii}$  of all CNTs depending on the B and N concentration. Both semiconducting and metallic CNTs transform into pure BN-NTs with a maximum band gap value of  $E_g = 4.5$  eV.

This work provides new insights into the modification and characterization of the electronic properties of carbon nanotubes. A simple model was developed that can be used for the characterization of samples with unknown tube distribution as well as for temperature estimates. The experience gained in synthesis and characterization of boron carbo-nitride nanostructures indicates ways for their possible application in the future.



# Appendix A

## A.1 Tight-binding model for graphite

In a free-electron approximation for a crystalline solid the electrons are considered to move freely in a crystal. Their motion, however, is influenced by the periodic potential produced by the atoms of a crystal.

The quasi-momentum of the electron in a crystal describes, thus motion in a periodic potential caused both by atoms periodically sited in the lattice points and their electrons. The points of the equivalent crystallitic potential  $U(\mathbf{r})$  have periodicity of the crystallitic lattice  $\mathbf{a}_n$ :

$$U(\mathbf{r}) = U(\mathbf{r} + \mathbf{a}_n), \quad (\text{A1})$$

The wavefunction  $\psi(\mathbf{r})$  for the electron in a periodic potential  $U(\mathbf{r})$  can be described in a form of the plane waves multiplied with the function, periodic with periodicity of the crystallitic lattice  $\mathbf{a}_n, n = 1, \dots, 3$  (i.e. Bloch functions):

$$\psi(\mathbf{r}) = e^{i\mathbf{k}\mathbf{r}} \cdot \varphi_{\mathbf{k}}(\mathbf{r}), \quad (\text{A2})$$

where  $\varphi_{\mathbf{k}}(\mathbf{r}) = \varphi_{\mathbf{k}}(\mathbf{r} + \mathbf{a}_n)$ , and  $\mathbf{k}$  is the quasi-wave vector of the electron moving in a periodic potential. Bloch functions satisfy the Bloch's theorem for an electron in a crystalline solid:

$$T_{\mathbf{a}_n} \psi(\mathbf{r}) = e^{i\mathbf{k}\mathbf{a}_n} \cdot \psi(\mathbf{r}), \quad (\text{A3})$$

where  $T_{\mathbf{a}_n}$  is the translation operation along the lattice vector  $\mathbf{a}_n$ .

The space periodicity of forces acting on electrons in crystals destroys the simple relation between the energy  $E$  and momentum  $E = \mathbf{p}^2/2m = \hbar^2\mathbf{k}^2/2m$  and gives rise to the energy dispersion  $E = f(\mathbf{p})$  or  $\omega = f(\mathbf{k})$ . The energy spectrum of the electron in a crystal has a quasy-discontinues structure with energy zones overlapping for metals and separated by the band gap of forbidden energy values for semiconductors and insulators.

In order to find out the electronic band structure in solids, one has to solve Schroedinger's equation:

$$-\frac{\hbar^2}{2m} \nabla^2 \psi(\mathbf{r}) + U(\mathbf{r})\psi(\mathbf{r}) = E\psi(\mathbf{r}), \quad (\text{A4})$$

for eigen values  $E$  and eigen functions  $\psi(\mathbf{r})$  satisfying the Bloch's theorem (eq. (A3)). The solution of the Eq. (A4) can be found in a form of the plain waves (Eq. (A2)). The linear combination of the plane waves is commonly used in theory (*ab initio* method or free electron approximation) due to the following reasons:

- (i) possibility of easy analytical integration of the plane wavefunctions;

- (ii) dependence of the numerical accuracy of the method only on the number of the plane waves.

The method of the plane waves has also some disadvantages such as:

- (i) large volume of computation;  
(ii) difficulties in relation between the plane wavefunctions and the atomic orbitals in the solid.

### ***Brillouin zone of the two-dimensional graphite***

It is convenient to consider the electron energies  $E$  in a crystal not in the real space of the crystalline lattice but in the reciprocal space of the quasi-wave vectors  $\mathbf{k}$ . For that purpose the reciprocal lattice should be introduced instead of the unit cell of the crystalline lattice. The relation between the real  $\mathbf{a}$  and the reciprocal  $\mathbf{b}$  lattice vectors is following:

$$\mathbf{b}_1 = 2\pi \frac{\mathbf{a}_2 \times \mathbf{a}_3}{V_0}, \quad \mathbf{b}_2 = 2\pi \frac{\mathbf{a}_1 \times \mathbf{a}_3}{V_0}, \quad \mathbf{b}_3 = 2\pi \frac{\mathbf{a}_1 \times \mathbf{a}_2}{V_0}, \quad (\text{A5})$$

were  $\mathbf{b}_1, \mathbf{b}_2, \mathbf{b}_3$ , and  $\mathbf{a}_1, \mathbf{a}_2, \mathbf{a}_3$  are reciprocal and real lattice vectors, respectively, in a three dimensional space, and  $V_0 = |(\mathbf{a}_1[\mathbf{a}_2 \times \mathbf{a}_3])|$  is the volume of the parallelepiped built on the  $\mathbf{a}$ -vectors.  $\mathbf{k}$ -vectors have periodicity of the reciprocal lattice and within the reciprocal unit cell built on the  $\mathbf{b}$ -vectors take non-equivalent values.

The space of the *non-equivalent* values of quasi-wavevectors  $\mathbf{k}$  (named *wavevectors* in following) is called the Brillouin zone. The first Brillouin zone can be defined by the following conditions:

$$\begin{aligned} -\frac{\pi}{\mathbf{a}_1} < \mathbf{k}_1 \leq \frac{\pi}{\mathbf{a}_1}, \\ -\frac{\pi}{\mathbf{a}_2} < \mathbf{k}_2 \leq \frac{\pi}{\mathbf{a}_2}, \\ -\frac{\pi}{\mathbf{a}_3} < \mathbf{k}_3 \leq \frac{\pi}{\mathbf{a}_3}. \end{aligned} \quad (\text{A6})$$

Construction of the Brillouin zone is defined by the reason of use. At the same time, for any crystalline lattice the three main conditions should be fulfilled:

- (i) the Brillouin zone must contain the point  $\mathbf{k} = 0$ ;  
(ii) the volume of the Brillouin zone must be  $(2\pi)^3/V_0$ , where  $V_0$  is the volume of the real unit cell built on  $\mathbf{a}$  – vectors;  
(iii) two arbitrary vectors  $\mathbf{k}_a$  and  $\mathbf{k}_b$  from the Brillouin zone must satisfy the condition:

$$|\mathbf{k}_a - \mathbf{k}_b| \leq (\mathbf{b}_1 + \mathbf{b}_2 + \mathbf{b}_3), \quad (\text{A7})$$

In Figure A1 (a, b) the unit cell and the corresponding Brillouin zone of two-dimensional graphite sheet (graphene) are presented.

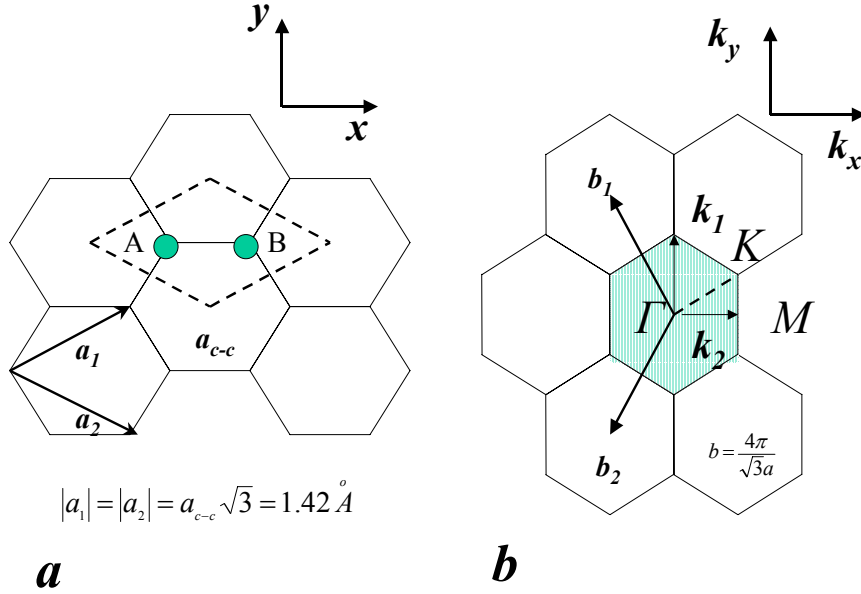


**Figure A1.** The real (a) and the reciprocal (b) lattice of the graphene. The real unit cell (dotted diamond in Fig. A1 (a)) built on the unit vectors  $\mathbf{a}_1$  and  $\mathbf{a}_2$  contains two carbon atoms A and B. The reciprocal lattice is rotated by  $90^\circ$  with respect to the real lattice. The first Brillouin zone for the graphene is represented by the dashed hexagon in Fig. A1 (b); the reciprocal vectors  $\mathbf{b}_1$  and  $\mathbf{b}_2$  and the points of high symmetry  $\Gamma$ ,  $K$ , and  $M$  are also shown.

The unit cell of the graphene is marked as dotted diamond in Fig. A1(a) and contains two carbon atoms, A and B. The unit vectors of the graphene unit cell  $\mathbf{a}_1$ , and  $\mathbf{a}_2$  can be presented as:

$$\mathbf{a}_1 = \{\mathbf{a}_{1x}; \mathbf{a}_{1y}\} = \left\{ \frac{\sqrt{3}a}{2}; \frac{a}{2} \right\}, \quad (\text{A8})$$

$$\mathbf{a}_2 = \{\mathbf{a}_{2x}; \mathbf{a}_{2y}\} = \left\{ \frac{\sqrt{3}a}{2}; -\frac{a}{2} \right\},$$

where  $a = a_{c-c} \sqrt{3} = 1.42 \text{ \AA}$ , and  $a_{c-c}$  is the nearest-neighbor distance between two carbon atoms. By translation of the unit cell along the directions of the unit vectors  $\mathbf{a}_1$ ,  $\mathbf{a}_2$  the whole graphene sheet can be reconstructed. The wavevectors for the first Brillouin zone defined by eq. (A6) can be presented as:

$$\mathbf{k}_1 = \left\{ \frac{\pi}{\mathbf{a}_{1x}}; \frac{\pi}{\mathbf{a}_{1y}} \right\} = \left\{ \frac{2\pi}{\sqrt{3}a}; \frac{2\pi}{a} \right\}, \quad (\text{A9})$$

$$\mathbf{k}_2 = \left\{ \frac{\pi}{\mathbf{a}_{2x}}; \frac{\pi}{\mathbf{a}_{2y}} \right\} = \left\{ \frac{2\pi}{\sqrt{3}a}; -\frac{2\pi}{a} \right\}.$$

Using the expressions (A8) and (A9) one can easily obtain the angle  $\beta = 30^\circ$  between the vectors  $\mathbf{a}$  and  $\mathbf{k}$  from  $\mathbf{a}\mathbf{b} = abc\cos\beta$ . The shaded hexagon in Fig.1 (b) indicates the Brillouin zone of the 2D-graphite with the reciprocal lattice constant  $b = 4\pi/\sqrt{3}a$ . Letters  $\Gamma$  ( $\mathbf{k} = 0$ ),  $M$  ( $\mathbf{k} = \pi/a$ ), and  $K$  ( $\mathbf{k} = 2\pi/\sqrt{3}a$ ) denote the high-symmetry points of the Brillouin zone, which coincide with themselves during the lattice symmetry operations.

The energy dispersion in the first Brillouin zone provides information about the electronic states of the whole crystal, similar to the unit cell of the crystalline lattice, which characterizes the symmetry of the whole crystal. Therefore, the calculation of electronic properties of solids requires deriving the energy dispersion only in the first Brillouin zone.

### ***sp<sup>n</sup> – hybridization in carbon materials, valence electrons in graphite***

Within the TB model only the valence electrons of atoms are usually considered since they define the electronic properties of the solid in the optical range of energies [12]. The core electrons have bonding energies of about  $10 - 10^2$  eV, which is much larger than the interaction with many kinds of the external fields, and is two orders of magnitude larger than a quantum of energy in the optical range ( $\approx 1 - 2$  eV). Therefore, considering the carbon atom, we will take into account only its valence electrons.

Carbon is the sixth element of the Periodic Table and listed at the top of column IV. It means that carbon has six electrons, four of which are the valence electrons. The electrons of carbon occupy  $1s^2 2s^2 2p^2$  atomic orbitals. The  $1s^2$  orbital contains two strongly bound core electrons which are not taken into consideration as mentioned above. In the crystalline solid the valence electrons give rise to the  $2s$ ,  $2p_x$ ,  $2p_y$ , and  $2p_z$  orbitals forming covalent bonds in carbon compounds. The electronic wave functions can mix with each other, because of the small energy difference between  $2s$  and  $2p$  orbitals less than the chemical bonds. Such a mixing of the wavefunctions changes the occupation of the  $2s$  and the three  $2p$  orbitals such as to enhance the binding energy of the carbon atom with its neighbouring atoms. This mixing of  $2s$  and  $2p$  atomic orbitals is called *sp<sup>n</sup> – hybridization*, where  $n = 1, 2, 3$  is the number of the contributing  $2p$  atomic orbitals.

In carbon materials,  $sp$ ,  $sp^2$ , and  $sp^3$  hybridizations may occur. In the one-dimensional chain-like molecule of acetylene ( $\text{HC} \equiv \text{CH}$ ), for example, one can observe  $sp$ -hybridization, a mixture of the  $2s$  and one of the  $2p$  electron orbitals (for example  $2p_x$ ). The hybridized  $sp$ -orbitals ( $\sigma$  bonds) between two carbon atoms extend along the molecule chain. The non-hybridized  $2p_y$  and  $2p_z$  orbitals are perpendicular to the molecular chain and call  $\pi$  bonds.

In the molecule of polyacetylene ( $\text{HC} = \text{CH} -$ )<sub>n</sub> the  $2s$  and two  $2p$  orbitals (for example  $2p_x$  and  $2p_y$ ) are hybridized. The carbon atoms form a two-dimensional zigzag chain with an angle of  $120^\circ$ , where two  $\sigma$  – bonds of each carbon atom lay in the plane of the molecular chain, and the non-hybridized  $\pi$  – orbital is perpendicular to this plane.

The three-dimensional molecules like a molecule of methane ( $\text{CH}_4$ ) have  $sp^3$  – hybridization. The molecule of carbon is bound with four hydrogen atoms which have maximal space separation from each other. In that case the  $2s$  orbital and the three  $2p$  orbitals are mixed with each other, forming four  $\sigma$  bonds. Therefore, in three dimensional molecules based on carbon atom, all four valence electrons occupy the  $\sigma$  bonds. Such a wide variation of the  $sp$ -hybridisations is a property of a carbon atom

only. The other elements from the IV group like Si and Ge show only  $sp^3$  hybridisation.

The sheets in graphene sheet lead to a two-dimensional hexagonal crystal lattice with  $sp^2$ -hybridization. The three valence electrons occupy three  $\sigma$  bonds in the plane of the sheet, and one electron occupies the non-hybridized  $\pi$  – orbital perpendicular to the graphene plane. The  $\pi$ -electrons in graphite materials except for diamond are responsible for the transport, optical properties, and the weak van-der-Waals interaction between carbon nanotubes. The  $\sigma$ -bonds do not, however, play a role in many solid-state properties because they are too far away from the Fermi level.

The Tight-Binding model for  $\pi$ -electrons of the 2D graphite sheet (graphene) combined with the Zone-folding (ZF) approximation gives the band structure of carbon nanotubes. For the nanotubes of larger diameters the results are quite accurate and coincide with the first principles calculation.

## A.2 Tight-binding approximation for carbon nanotubes

The other approach in calculation of the band structure of solids (apart from the free-electron approximation) is the Tight-Binding (TB) model. Here electrons are considered as parts of the atoms and described by atomic orbital functions. These atomic orbitals overlap due to the small atomic distances and strong interaction (tight binding) between neighboring atoms in a crystal lattice. To find the band structure of a crystalline solid one has to solve Schroedinger's equation:

$$H\psi(\mathbf{k}) = E(\mathbf{k})\psi(\mathbf{k}). \quad (\text{A10})$$

$H$  is the Hamiltonian,  $E(\mathbf{k})$  are the eigenenergies of the Hamiltonian  $H$  at wave vector  $\mathbf{k}$ , and  $\psi(\mathbf{k})$  are the eigenfunctions. The eigenfunctions  $\psi(\mathbf{k})$  can be presented as linear combination of the Bloch functions  $\Phi_j(\mathbf{k}, \mathbf{r})$ , based on the  $j$ -th atomic orbital in the unit cell:

$$\psi(\mathbf{k}) = \sum_j C_j \Phi_j(\mathbf{k}, \mathbf{r}). \quad (\text{A11})$$

The tight binding Bloch function  $\Phi_j(\mathbf{k}, \mathbf{r})$  is given by:

$$\Phi_j(\mathbf{k}, \mathbf{r}) = \frac{1}{\sqrt{N}} \sum_{\mathbf{R}} e^{i\mathbf{k}\mathbf{R}} \varphi_j(\mathbf{r} - \mathbf{R}), \quad (j = 1, \dots, N), \quad (\text{A12})$$

where  $\mathbf{R}$  is the position of the atom and  $\varphi_j$  denotes the atomic wavefunction in a state  $j$ . The number of atomic wavefunctions in the unit cell is denoted by  $N$ , i.e. there are  $N$  Bloch functions in the solid for a given  $\mathbf{k}$ . The wavefunctions  $\varphi_j$  in the  $N$  ( $\approx 10^{24}$ ) unit cells of the whole crystal are weighted by the phase factor  $e^{i\mathbf{k}\mathbf{R}}$ , the sum runs over all possible lattice vectors  $\mathbf{R}$  of the whole crystal.

A carbon atom has four valence electrons, three of which belong to the  $sp^2$  – hybridized  $\sigma$ -orbitals in the plane of the graphene sheet, and one  $2p_z$  electron belongs to the unhybridized  $\pi$ -orbital perpendicular to the graphene plane. This  $\pi$ -bond is of the

interest because its dispersions cross the Fermi energy giving rise to the optical and electronic properties of graphite.

The graphene unit cell contains two carbon atoms A and B (Fig. A1, a). Each atom has one valence electron occupying an atomic  $\pi$ -orbital, therefore the wavefunction  $\psi(\mathbf{k})$  for two atoms in Eq. (A11) can be written as a linear combination of two overlapping atomic orbitals:

$$\psi(\mathbf{k}) = \Phi_A(\mathbf{k}, \mathbf{r}) + \lambda \Phi_B(\mathbf{k}, \mathbf{r}), \quad (\text{A13})$$

where functions

$$\Phi_A(\mathbf{k}, \mathbf{r}) = \frac{1}{\sqrt{N}} \sum_{\mathbf{R}} e^{i\mathbf{k}\mathbf{R}} \varphi_A(\mathbf{r} - \mathbf{R}) \quad (\text{A14})$$

and

$$\Phi_B(\mathbf{k}, \mathbf{r}) = \frac{1}{\sqrt{N}} \sum_{\mathbf{R}} e^{i\mathbf{k}\mathbf{R}} \varphi_B(\mathbf{r} - \mathbf{R})$$

are two overlapping atomic orbitals, and  $\varphi_A(\mathbf{r} - \mathbf{R})$ ,  $\varphi_B(\mathbf{r} - \mathbf{R})$  are the  $2p_z$  wavefunctions for isolated atoms. The overlapping of these functions is zero, i.e.

$$\int \varphi_A(\mathbf{r} - \mathbf{R}) \varphi_B(\mathbf{r} - \mathbf{R}) d\tau = 0. \quad (\text{A15})$$

The next step can be the substitution of the  $\psi(\mathbf{k})$  in the Schroedinger's Eq. (A10) by expressions (A13) and (A14). By multiplying the both sides of (A10) with conjugate functions  $\Phi_A^*(\mathbf{k}, \mathbf{r})$  and  $\Phi_B^*(\mathbf{k}, \mathbf{r})$  and integrating over the whole space  $\tau$  the coefficient  $\lambda$  can be finally eliminated from:

$$\begin{aligned} \int \Phi_A^* H \Phi_A d\tau + \lambda \int \Phi_A^* H \Phi_B d\tau &= E \int \Phi_A^* \Phi_A d\tau + \lambda E \int \Phi_A^* \Phi_B d\tau, \\ \int \Phi_B^* H \Phi_A d\tau + \lambda \int \Phi_B^* H \Phi_B d\tau &= E \int \Phi_B^* \Phi_A d\tau + \lambda E \int \Phi_B^* \Phi_B d\tau, \end{aligned} \quad (\text{A16})$$

where parts are defined as:

$$\begin{aligned} \int \Phi_A^* H \Phi_A d\tau &= H_{AA}, \\ \int \Phi_B^* H \Phi_B d\tau &= H_{BB}, \\ \int \Phi_A^* H \Phi_B d\tau &= \int \Phi_B^* H \Phi_A d\tau = H_{AB} = H_{BA}^*, \\ \int \Phi_A^* \Phi_A d\tau &= \int \Phi_B^* \Phi_B d\tau = S, \\ \int \Phi_A^* \Phi_B d\tau &= \int \Phi_A^* \Phi_B d\tau = S_{AB}. \end{aligned} \quad (\text{A17})$$

The system of linear equations for  $\lambda$  will be then:

$$\left\{ \begin{array}{l} H_{AA} + \lambda H_{AB} = ES \\ H_{BA} + \lambda H_{BB} = \lambda ES \end{array} \right\}. \quad (\text{A18})$$

The energy  $E$  can be extracted from (A18) as follows:

$$E = \frac{1}{2S} \left( H_{AA} + H_{BB} \pm \sqrt{(H_{AA} - H_{BB})^2 + 4|H_{AB}|^2} \right). \quad (\text{A19})$$

Here  $E^+$  and  $E^-$  are the energies of the valence and the conduction band, respectively. The overlap integrals are taken to be  $S = 1$ , also from the symmetry reasons  $H_{AA} = H_{BB}$ . Finally, the energy is given by:

$$E = H_{AA} \pm |H_{AB}|. \quad (\text{A20})$$

For the carbon atom A interacting with its first nearest-neighbors (Fig. A2, atoms 11, 12, 13),  $H_{AA}$  becomes constant, reflecting only the properties of the atom A.

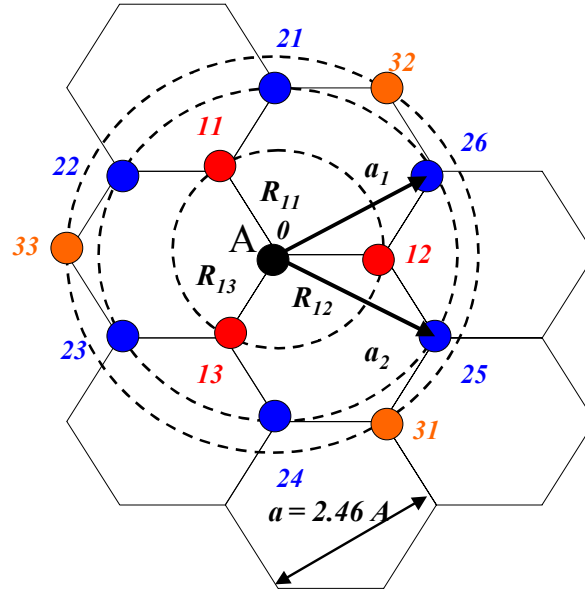


**Figure A2.** Three nearest neighbors of the atom A inside the graphene unit cell (see also Fig. A1). Vectors  $\mathbf{R}_{11}$ ,  $\mathbf{R}_{12}$  and  $\mathbf{R}_{13}$  point on the first nearest-neighbor atoms of the atom A.

The energies  $E$  with respect to the atom A in the first nearest-neighbor approximation will be then:

$$E = \pm |H_{AB}|. \quad (\text{A21})$$

In this approximation the valence and the conduction bands of graphene are symmetric with respect to the Fermi level. The expression (A21) is called the “tight-binding approximation”. It gives a satisfactory precision for the energy dispersions

only at the  $K$ -point ( $\mathbf{k} = 2\pi/\sqrt{3}a$ ) of the Brillouin zone. The matrix element  $H_{AA} = \varepsilon_{2p}$  is constant for the nearest-neighbor interaction. This is the energy of the  $2p_z$  state of an *isolated* atom situated, however, in a periodic potential.

In order to calculate  $H_{AB}$  the Eq. (A17) must be used with the wavefunctions from Eq. (A14), i.e.:

$$H_{AB} = \frac{1}{N} \sum_{\mathbf{R}_A} \sum_{\mathbf{R}_B} e^{ik(\mathbf{R}_A - \mathbf{R}_B)} \int \varphi_A(\mathbf{r} - \mathbf{R}_A) H \varphi_B(\mathbf{r} - \mathbf{R}_B) d\tau. \quad (\text{A22})$$

The sum runs over all three nearest neighbors of a given atom A, the vectors  $\mathbf{R} = \mathbf{R}_{B1i} - \mathbf{R}_A$  point on the first neighboring atoms (Fig. A2):

$$R_{11} = 1/3(2\mathbf{a}_1 - \mathbf{a}_2), \quad R_{12} = 1/3(-\mathbf{a}_1 + 2\mathbf{a}_2), \quad R_{13} = 1/3(-\mathbf{a}_1 - \mathbf{a}_2). \quad (\text{A23})$$

The sum (A22) contains three integrals in a form of  $\int \varphi_A H \varphi_{B1i} d\tau$ . Since the functions  $\varphi_S$  are radially symmetric in the graphene plane the integrals depend only on the distances between atoms A and B which is constant. Therefore,

$$\begin{aligned} H_{AB}(\mathbf{k}) &= \int \varphi_A(\mathbf{r} - \mathbf{R}_A) H \varphi_B(\mathbf{r} - \mathbf{R}_A - \mathbf{R}_{11}) d\tau (e^{ikR_{11}} + e^{ikR_{12}} + e^{ikR_{13}}) = \\ &= \gamma_0 (e^{-\frac{1}{3}ik(a_1+a_2)}) (e^{ika_1} + e^{ika_2} + 1). \end{aligned} \quad (\text{A24})$$

Here,  $\gamma_0$  is the carbon-carbon interaction energy, or the *tight-binding integral*. The value  $S_{AB}$  is the overlap matrix element which is defined by:

$$S_{AB}(\mathbf{k}) = s_0 (e^{-\frac{1}{3}ik(a_1+a_2)}) (e^{ika_1} + e^{ika_2} + 1), \quad (\text{A25})$$

where  $s_0 = \int \varphi_A \varphi_{B1i} d\tau$ .

The intermediate calculations are presented in [12, 13]. The final eigenenergies in the nearest-neighbor approximation can be written as following:

$$E^\pm(\mathbf{k}_x, \mathbf{k}_y) = \frac{\varepsilon_{2p} \pm \gamma_0 \sqrt{f_{12}(\mathbf{k}_x, \mathbf{k}_y)}}{1 \pm s_0 \sqrt{f_{12}(\mathbf{k}_x, \mathbf{k}_y)}}, \quad (\text{A26})$$

where the function  $f(\mathbf{k}_x, \mathbf{k}_y)$  is given by:

$$f(\mathbf{k}_x, \mathbf{k}_y) = 1 + 4\text{Cos} \frac{\sqrt{3}\mathbf{k}_x a}{2} \text{Cos} \frac{\mathbf{k}_y a}{2} + 4\text{Cos}^2 \frac{\mathbf{k}_y a}{2}. \quad (\text{A27})$$

Here  $\mathbf{k}_x$  and  $\mathbf{k}_y$  are the graphite wavevectors (see Fig. A1). The parameters  $\varepsilon_{2p}$ ,  $\gamma_0$ , and  $s_0$  are empirical. At  $K$ -point the  $E = 0$ , and the valence and conduction cross the Fermi energy  $E_F = 0$ , therefore,  $\varepsilon_{2p} = 0$ . The absolute value of  $s_0$  is between zero and one (for normalized wave functions), and the sign is positive. Parameter  $\gamma_0$  must be negative and its value in different literature varies from 2.9 - 3.3 eV [12, 13, 38].

Fig. A3 shows the three-dimensional energy dispersion for graphene obtained with Eqs. (A26) and (A27) through the whole Brillouin zone:  $-2\pi/\sqrt{3}a < k_x \leq 2\pi/\sqrt{3}a$ , and  $-\pi/a < k_y \leq \pi/a$ .

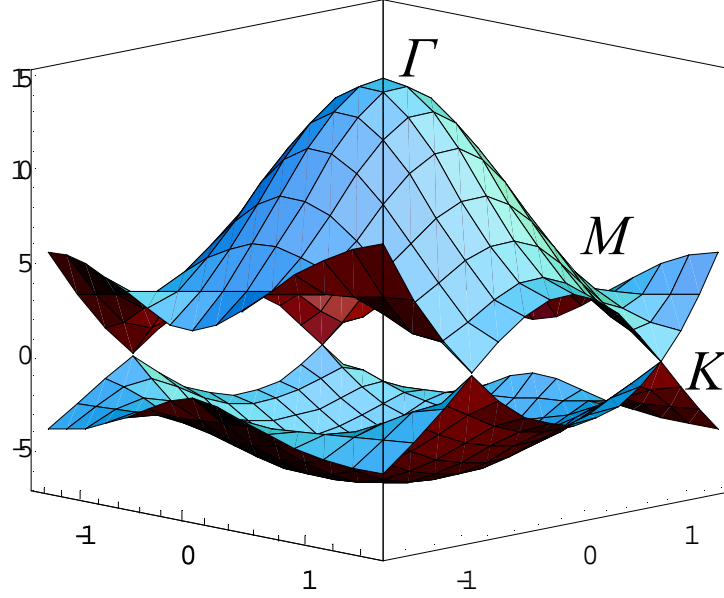


**Figure A3.** 3D energy dispersion for the graphene sheet calculated using Eqs. (A26) and (A27) through the whole Brillouin zone:  $-2\pi/\sqrt{3}a < k_x \leq 2\pi/\sqrt{3}a$ , and  $-\pi/a < k_y \leq \pi/a$ . The points of high symmetry  $\Gamma$ ,  $M$ , and  $K$  are also shown.

Expression (A27) is the famous tight-binding approximation for graphene. In order to describe the electronic band structure of carbon nanotubes, the wavevectors  $\mathbf{k}_\perp$  and  $\mathbf{k}_z$  must be introduced in Eq. (A27) instead of  $k_x$  and  $k_y$ . The orientation of the nanotube wavevectors  $\mathbf{k}_\perp$  and  $\mathbf{k}_z$  with respect to the graphene wavevectors  $k_x$  and  $k_y$  depends on the nanotube chiral angle  $\theta$  (see section 3.1). Transformation of the Cartesian coordinates in the Eq. (A27) gives the following expression for the energy dispersion [107]:

$$E^\pm(\mathbf{k}_z, \mathbf{k}_\perp) = \pm \gamma_0 \left[ 1 + 4 \cos^2 \frac{\sqrt{3}a(\mathbf{k}_z \cos \theta + \mathbf{k}_\perp \sin \theta)}{2} \cos \frac{a(\mathbf{k}_z \sin \theta - \mathbf{k}_\perp \cos \theta)}{2} + \frac{a(\mathbf{k}_z \sin \theta - \mathbf{k}_\perp \cos \theta)}{2} \right]^{1/2} \quad (\text{A28})$$

Here, the carbon nanotube wavevectors take the following values:  $|\mathbf{k}_\perp| = 2\mu/d$ ,  $\mu = -N/2 + 1, \dots, 0, N/2$ , where  $N$  is the number of hexagons in the unit cell and  $\mathbf{k}_z$  is confined within the first Brillouin zone  $[-2\pi/\sqrt{3}a, 2\pi/\sqrt{3}a]$ . The states near the

corner of the Brillouin zone (the  $K$ -point located at  $(2\pi/\sqrt{3}a)(\cos\theta; -\sin\theta)$ ) correspond to the low-energy states of carbon nanotubes responsible for many physical phenomena. The expression (A28) can be expanded then near the  $K$ -point at the corner of the graphite hexagonal Brillouin zone [107, 108]:

$$E^\pm(k_z, k_\perp) = \pm\gamma_0 \left[ \frac{9a^2}{12} [k_\perp^2 + k_z^2] + \frac{9a^3 k_\perp}{24\sqrt{3}} [k_\perp^2 - 3k_z^2] \cos 3\theta + \frac{9a^3 k_z}{24\sqrt{3}} [k_z^2 - 3k_\perp^2] \sin 3\theta - \frac{27a^4}{576} [k_\perp^2 + k_z^2]^2 \right]^{1/2}, \quad (\text{A29})$$

where  $k_\perp = (2/d)(j - i/3)$ , where  $j = 0, \mp 1, \mp 2, \dots$  and  $i$  satisfies  $2n + m = 3I - i$ ,  $I$  - integer. Thus,  $k_\perp = 0; \mp 2/d, \pm 4/d, \dots$  for metallic tubes and  $k_\perp = -2/3d, 4/3d, \dots$  ( $2/3d, -4/3d, \dots$ ) for semiconducting tubes. The edge states with  $k_z = 0$  lead to the 1D vHs in the DOS (see section 3.2). The electronic interband transitions also occur close to the  $K$ -point. Therefore, the transition electronic energies can be obtained within a TB approximation with eq. (A29) at  $k_z = 0$  (see Kataura plot in Fig. 3.9).

The advantages of using a tight-binding function in the form of atomic orbitals can be summarized as follows:

- (i) small number of the basic functions compared to the number of plain waves;
- (ii) possibility to derive easily the formulae for many physical properties.

Among the limitations of the tight-binding approximation are the following:

- (i) the simple formula (A26) for the energy dispersion in the first nearest-neighbor approximation will never correctly reproduce the result of the *ab initio* calculation;
- (ii) no simple procedure to improve the numerical accuracy of the calculation;
- (iii) atomic orbitals do not describe the inter-atomic region.

# Bibliography

- [1] S. Iijima. Helical microtubules of graphitic carbon. *Nature* **354**, 56 (1991).
- [2] M. Radosavljević, J. Lefebvre, and A. T. Johnson. High-field electrical transport and breakdown in bundles of single-wall carbon nanotubes. *Phys. Rev. B* **64**, 241307 (R) (2001).
- [3] S.-B. Lee, K. B. K. Teo, L. A. W. Robinson, A. S. Teh, M. Chhowalla, *et al.* Characteristics of multiwalled carbon nanotube Nanobridge using PMMA suspended dispersion. *Journal of Vacuum Science and Technology B* **20**, 2773 (2002).
- [4] J.-P. Salvetat, G. A. D. Briggs, J.-M. Bonard, R. R. Bacsa, A. J. Kulik, *et al.* Elastic and shear moduli of single-walled carbon nanotube ropes. *Phys. Rev. Lett.* **82**, 944 (1999).
- [5] M. M. J. Treacy, T. W. Ebbesen, and J. M. Gibson. Exceptionally high Young's modulus observed for individual carbon nanotubes. *Nature* **381**, 678 (1996).
- [6] S. M. Bachilo, M. S. Strano, C. Kittrell, R. H. Hauge, R. E. Smalley, and R. B. Weisman. Structure-assigned optical spectra of single-walled carbon nanotubes. *Science* **297**, 2361 (2002).
- [7] S. B. Cronin, R. Barnett, M. Tinkham, S. G. Chou, O. Rabin, M. S. Dresselhaus, *et al.* Electrochemical gating of individual single-wall carbon nanotubes observed by electron transport measurements and resonant Raman spectroscopy. *Appl. Phys. Lett.* **84**, 2052 (2004).
- [8] G. Pirio, P. Legagneux, D. Pribat, K. B. K. Teo, M. Chhowalla, G. A. J. Amaratunga, and W. I. Milne. Fabrication and electrical characteristics of carbon nanotube field emission microcathodes with an integrated gate electrode. *Nanotechnology* **13**, 1 (2002).
- [9] P. Avouris. Molecular electronics with carbon nanotubes. *Acc. Chem. Res.* **35**, 1026 (2002).
- [10] S. Akita, H. Nishijima, Y. Nakayama, F. Tokumasu, and K. Takeyasu. Carbon nanotube tips for a scanning probe microscope: their fabrication and properties. *J. Phys. D: Appl. Phys.* **32** 1044 (1999).
- [11] Zh. Deng, E. Yenilmez, J. Leu, J. E. Hoffman, E. W. J. Straver, *et al.* Metal-coated carbon nanotube tips for magnetic force microscopy. *Appl. Phys. Lett.* **85**, 6263 (2004).
- [12] R. Saito, G. Dresselhaus, M.S. Dresselhaus. *Physical Properties of Carbon Nanotubes*. Imperial College Press (1998).
- [13] S. Reich, C. Thomsen, and J. Maultzsch. *Carbon Nanotubes: Basic Concepts and Physical Properties*. WILEY-VCH Verlag GmbH&Co.K.GaA, Weinheim (2004).
- [14] H. B. Peng, and J. A. Golovchenko. Coulomb blockade in suspended Si<sub>3</sub>N<sub>4</sub>-coated single-walled carbon nanotubes. *Appl. Phys. Lett.* **84**, 5428 (2004).
- [15] R. Krupke, F. Hennrich, H. v. Löhneysen, M. M. Kappes. Separation of metallic from semiconducting single-walled carbon nanotubes. *Science* **301**, 344 (2003).
- [16] M. S., Dresselhaus, G. Dresselhaus, and Ph. Avouris. *Carbon Nanotubes: Synthesis, Structure, Properties, and Applications*. Springer Verlag, Berlin (2001).
- [17] M. J. O'Connell, S. M. Bachilo, C. B. Huffman, V. C. Moore, M. S. Strano, *et al.* Band gap fluorescence from individual single-walled carbon nanotubes. *Science* **297**, 593 (2002).
- [18] C. Fantini, A. Jorio, M. Souza, M. S. Strano, M. S. Dresselhaus, and M. A. Pimenta. Optical transition energies for carbon nanotubes from resonant Raman

- spectroscopy: environment and temperature effects. *Phys. Rev. Lett.* **93**, 147406 (2004).
- [19] R. B. Capaz, C. D. Spataru, P. Tangney, M. L. Cohen, and S.G. Louie. Temperature dependence of the band gap of semiconducting carbon nanotubes. *Phys. Rev. Lett.* **94**, 036801 (2005).
- [20] X. Blase, J-Ch. Charlier, A. De Vita, R. Car. Structural and electronic properties of composite  $B_xC_yN_z$  nanotubes and heterojunctions. *Appl Phys. A* **68**, 293 (1999).
- [21] X. Blase. Properties of composite  $B_xC_yN_z$  nanotubes and related heterojunctions. *Computation Mater. Science* **17**, 107 (2000).
- [22] T. Yoshioka, H. Suzuura, T. Ando. Electronic states of BCN alloy nanotubes in a simple tight-binding model. *Journal of Phys. Society of Japan* (available online).
- [23] J.W. Mintmire and C.T.White. Universal density of states for carbon nanotubes. *Phys. Rev. Lett.* **81**, 2506 (1998).
- [24] N.W. Ashcroft, N.D. Mermin, *Solid State Physics*, Harcourt College Publishers, 1976.
- [25] T.W. Odom, J.L. Huang, P. Kim and C.M. Lieber. Atomic structure and electronic properties of single-walled carbon nanotubes. *Nature* **391**, 62 (1998).
- [26] T.W. Odom, J.L. Huang, P. Kim, M. Ouyang and C.M. Lieber. Scanning tunneling microscopy and spectroscopy studies of single-walled carbon nanotubes. *J. Mater. Res.* **13**, 59 (1998).
- [27] M.A. Pimenta, A. Marucci, S. Empedocles, M.Bawendi, E.B. Hanlon, *et al.* Raman modes of metallic carbon nanotubes. *Phys Rev. B* **58**, 16016 (1998).
- [28] S.D. Brown, P.Corio, A. Marucci, M.S. Dresselhaus, M.A. Pimenta, and K.Kneipp. Anti-Stokes Raman spectra of single-walled carbon nanotubes. *Phys. Rev. B* **61**, 5137 (2000).
- [29] P.M. Rafailov, H. Jantoliak, and C.Thomsen. Electronic transitions in single-walled carbon nanotubes: a resonance Raman study. *Phys. Rev. B* **61**, 16179 (2000).
- [30] A. Jorio, A.G.Souza Filho, G. Dresselhaus, M.S. Dresselhaus, R. Saito, *et al.* Joint density of electronic states for one isolated single-wall carbon nanotube studied by resonant Raman scattering. *Phys. Rev. B* **63**, 245416 (2001).
- [31] A. Jorio, C. Fantini, M.A. Pimenta, R.B. Capaz, Ge.G. Samsonidze, G. Dresselhaus, M.S. Dresselhaus, J.Jiang, N. Kobayashi, A. Grueneis, and R. Saito. Resonance Raman spectroscopy ( $n,m$ )-dependent effects in small-diameter single-wall carbon nanotubes. *Phys. Rev. B* **71**, 075401 (2005).
- [32] J. Jiang, R. Saito, S.G. Chou, Ge.G. Samsonodze, A. Jorio, G. Dresselhaus, M.S. Dresselhaus. Intensity of the resonance Raman excitation spectra of single-wall carbon nanotubes. *Phys. Rev. B* **71**, 205420 (2005).
- [33] J.W. Ding, X.H. Yan, J.X. Cao. Analytical relation of band gaps to both chirality and diameter of single-wall carbon nanotubes. *Phys. Rev. B* **66**, 073401 (2002).
- [34] A. Hagen, T. Hertel. Quantitative analysis of optical spectra from individual single-wall carbon nanotubes. *Nanolett.* **3**, 383 (2003).
- [35] M. Cardona, "Resonance phenomena", in *Light Scattering in Solids II*, edited by M. Cardona and G. Guentherodt (Springer, Berlin, 1982), vol. 50 of *Topics in Applied Physics*.
- [36] R.M. Martin and L.M. Falicov, "Resonant Raman Scattering", in *Light Scattering in Solids I*, edited by M.Cardona (Springer, Berlin Heidelberg New York, 1983), vol. 8 of *Topics in Applied Physics*.
- [37] R.A. Jishi, L.Venkataraman, M.S. Dresselhaus, and G. Dresselhaus. Phonon modes in carbon nanotubules, *Chem. Phys. Lett.* **209**, 77 (1993).

- [38] M.S. Dresselhaus and P.C. Eklund. Phonons in carbon nanotubes. *Advances in Physics* **49**, 705 (2000).
- [39] S. Lebedkin, F. Hennrich, T. Skipa, M. Kappes. Near-infrared photoluminescence of single-walled carbon nanotubes prepared by the laser vaporization method *J. Phys. Chem. B* **107**, 1949 (2003).
- [40] T. Skipa, P. Schweiss, F. Hennrich, S. Lebedkin. Modification of the electronic properties of carbon nanotubes: bundling and B- and N- doping. *AIP Conf. Proceedings: Electronic Properties of Novel Nanostructures* **786**, 198 (2005).
- [41] C. Thomsen and S. Reich. Double-resonant Raman scattering in graphite. *Phys. Rev. Lett.* **85**, 5214 (2000).
- [42] J. Maultzsch, S. Reich, and C. Thomsen. Raman scattering in carbon nanotubes revised. *Phys. Rev. B* **65**, 233402 (2002).
- [43] C. Kane-Maguire and J.A. Koningstein. On the vibroelectric Raman effect. *J. Chem. Phys.* **59**, 1899 (1973).
- [44] E. Richter and K.R. Subbaswamy. Theory of size-dependent resonance raman scattering from carbon nanotubes. *Phys. Rev. Lett.* **79**, 2738 (1997).
- [45] S. Lebedkin, F. Hennrich, T. Skipa, R. Krupke, and M. Kappes. Near-infrared photoluminescence of single-walled carbon nanotubes obtained by the pulse laser vaporization method. *AIP Conf. Proceedings: Molecular Nanostructures* **685**, 148 (2003).
- [46] S. Reich, C. Thomsen, and P. Ordejón. Electronic band structure of isolated and bundled carbon nanotubes. *Phys. Rev. B* **65**, 155411 (2002).
- [47] P. Delaney, H.J. Choi, J. Ihm, S.G. Louie, and M.L. Cohen. Broken symmetry and pseudogaps in ropes of carbon nanotubes. *Nature* **391**, 466 (1998).
- [48] P. Delaney, H.J. Choi, J. Ihm, S.G. Louie, and M.L. Cohen. Broken symmetry and pseudogaps in ropes of carbon nanotubes. *Phys. Rev. B* **60**, 7899 (1999).
- [49] Y.-K. Kwon, S.Saito, and D. Tománek. Effect of intertube coupling on the electronic structure of carbon nanotube ropes. *Phys. Rev. B* **58**, 13314 (1998).
- [50] A. Ugawa, A. G. Rinzler, and D.B. Tanner. Far-infrared gaps in single-wall carbon nanotubes. *Phys. Rev. B* **60**, 11305 (1999).
- [51] A.M. Rao, J. Chen, E. Richter, U. Schlecht, P.C. Eklund, *et al.* Effect of van der Waals interactions on the Raman modes in single walled carbon nanotubes. *Phys. Rev. Lett.* **86**, 3895 (2001).
- [52] M.J. O'Connell, S. Sivaram, and S.K. Doorn. Near-infrared resonance Raman excitation profile studies of single-walled carbon nanotube intertube interactions: A direct comparison of bundled and individually dispersed HiPco nanotubes. *Phys. Rev. B* **69**, 235415 (2004).
- [53] M. Quyang, J.-L. Huang, C.L. Cheung, and C.M. Lieber. Energy gaps in "metallic" single-walled carbon nanotubes. *Science* **292**, 702 (2001).
- [54] T.W. Odom, J.-L. Huang, P. Kim, M. Ouyang, and C.M. Lieber. Structure and electronic properties of carbon nanotubes. *J. Phys. Chem. B* **104**, 2794 (2000).
- [55] P. Nikolaev, M. J. Bronikowski, R. K. Bradley, F. Rohmund, D.T. Colbert, K. A. Smith and R. E. Smalley. Gas-phase catalytic growth of single-walled carbon nanotubes from carbon monoxide. *Chem. Phys. Lett.* **313**, 91, (1999).
- [56] M.J. Bronikowski, P.A. Willis, D.T. Colbert, K.A. Smith, and R.E. Smalley. Gas-phase production of carbon single-walled nanotubes from carbon monoxide via the HiPCO process: A parametric study. *J. Vac. Sci. Technol. A* **19**, 1800 (2001).
- [57] O. Jost, A. Gorbunov, W. Pompe, T. Pichler, M. Friedlein, M. Knupfer, M. Reibold, H.-D. Bauer, L. Dunsch, M.S. Golden, J. Fink. Diameter grouping in bulk

- samples of single-walled carbon nanotubes from optical absorption spectroscopy. *J. Appl. Phys. Lett.* **75**, 2217 (1999).
- [58] T. Guo, P. Nikolaev, A. Thess, D.T. Colbert, R.E. Smalley. Catalytic growth of single-walled nanotubes by laser vaporization. *Chem. Phys. Lett.* **243**, 49 (1995).
- [59] A. G. Rinzler, J. Liu, H. Dai, P. Nikolaev, C.B. Huffman, F. J. Rodriguez-Macias, P. J. Boul, A. H. Lu, D. Heymann, D.T. Colbert, R.S. Lee, J.E. Fisher, A. M. Rao, P.C. Eklund, R. E. Smalley. Large scale purification of single-wall carbon nanotubes: process, product, and characterization. *Appl. Phys. A* **67**, 29 (1998).
- [60] S. Lebedkin, P. Schweiss, B. Renker, S. Malik, F. Hennrich, M. Neumaier, C. Stoermer, M.M. Kappes. Single-wall Carbon Nanotubes with Diameters Approaching 6 nm Obtained by Laser Vaporization. *Carbon*, **40**, 417 (2002).
- [61] F. Hennrich, S. Lebedkin, S. Malik, J. Tracy, M. Barczewski, H. Rösner, M.M. Kappes. Preparation, characterization and applications of free-standing single wall carbon nanotube thin films. *Phys. Chem. Chem. Phys.* **4**, 2273 (2002).
- [62] M.S. Strano, S. K. Doorn, E. H. Haroz, C. Kittrell, R.H. Hauge, and R.E. Smalley. Assignment of (n, m) Raman and optical features of metallic single-walled carbon nanotubes. *Nano Letters* **3**, 1091 (2003).
- [63] E.S. Zouboulis and M. Grimsditch. Raman scattering in diamond up to 1900 K. *Phys. Rev. B* **43**, 12490 (1991).
- [64] H. Herchen and M.A. Cappelli. First-order Raman spectrum of diamond at high temperatures. *Phys. Rev. B* **43**, 11740 (1991).
- [65] PingHeng Tan, YuanMing Deng, Qian Zhao, and WenChao Cheng. The intrinsic temperature effect of the Raman spectra of graphite. *Appl. Phys. Lett.* **74**, 1818 (1999).
- [66] P. Lespade, R. Al-Jishi, M.S. Dresselhaus. Model for Raman scattering from incompletely graphitizes carbons. *Carbon* **20**, 427 (1982).
- [67] PingHeng Tan, YuanMing Deng, and Qian Zhao. Temperature-dependent Raman spectra and anomalous Raman phenomenon of highly oriented pyrolytic graphite. *Phys. Rev. B* **58** 5435 (1998).
- [68] Yu. Maniwa, R. Fujiwara, H. Kira, H. Tou, H. Kataura *et al.* Thermal expansion of single-walled carbon nanotube (SWNT) bundles: X-ray diffraction studies. *Phys. Rev. B* **64**, 241402 (2001).
- [69] Yu. Maniwa, R. Fujiwara, H. Kira, H. Tou, E. Nishibori. Multiwalled carbon nanotubes grown in hydrogen atmosphere: an X-ray diffraction study. *Phys. Rev. B* **64**, 073105 (2001).
- [70] N.R. Raravikar, P. Keblinski, A.M. Rao, M. S. Dresselhaus, L.S. Schadler, and P.M. Ajayan. Temperature dependence of radial breathing mode Raman frequency of single-walled carbon nanotubes. *Phys. Rev. B* **66**, 235424-1 (2002).
- [71] S.N. Bokova, V.I. Konov, E.D. Obratsova, A.V. Osadchii, A.S. Pozharov, S.V. Terekhov. Laser-induced effects in Raman spectra of single-wall carbon nanotubes. *Quantum Electronics* **33** (7), 645-650 (2003).
- [72] S.D. Brown, P. Corio, A. Marucci, and M.S. Dresselhaus. Anti-Stokes Raman spectra of single-walled carbon nanotubes. *Phys. Rev. B* **61**, 5137 (2000).
- [73] O. Madelung. *Semiconductors: Group IV Elements and III-V Compounds*. Springer-Verlag, Berlin (1991).
- [74] M. Cardona, T.A. Meyer, and M.L.W. Thewalt. Temperature dependence of the energy gap of semiconductors in the low-temperature limit. *Phys. Rev. Lett.* **92**, 196403 (2004).
- [75] L. Viña, S. Logothetidis, and M. Cardona. Temperature dependence of the dielectric function of germanium. *Phys. Rev. B* **30**, 1979, (1984).

- [76] N. Srivastava and K. Banerjee. A comparative scaling analysis of metallic and carbon nanotube interconnections for nanometer scale VLSI technologies. *Proceed. of the 21<sup>st</sup> International VLSI Multilevel Interconnect Conference (VMIC)*, 393 (2004).
- [77] R. Tenne, and A.K. Zettl. Nanotubes from inorganic materials. In *Carbon Nanotubes*, edited by M.S. Dresselhaus, G. Dresselhaus, Ph. Avouris. *Topics Appl. Phys.* **80**, 81-112, Springer-Verlag Berlin Heidelberg (2001).
- [78] X. Blase, A. Rubio, S.G. Louie, M.L. Cohen. Quasiparticle band structure of bulk hexagonal boron nitride and related systems. *Phys. Rev. B* **51**, 6868 (1995).
- [79] Y. Miyamoto, A. Rubio, S.G. Louie, M.L. Cohen. Electronic properties of tubule forms of hexagonal BC<sub>3</sub>. *Phys. Rev. B* **50**, 18360 (1994).
- [80] M. Terrones, N. Grobert, H. Terrones. Synthesis routes to nanoscale B<sub>x</sub>C<sub>y</sub>N<sub>z</sub> architectures. *Carbon* **40**, 1665 (2002).
- [81] Y. Miyamoto, M.L. Cohen, S. G. Louie. Theoretical investigation of graphitic carbon nitride and possible tubule forms. *Solid State Commun.* **102**, 605 (1997).
- [82] R. Kurt, C. Klinke, J-M. Bonard, K. Kern, A. Karimi. Tailoring the diameter of decorated C-N nanotubes by temperature variations using HF-CVD. *Carbon* **39**, 2163 (2001).
- [83] D. Golberg, Y. Bando, L. Bourgeois, K. Kurashima, T. Sato. Large-scale synthesis and HRTEM analysis of single-walled B- and N-doped carbon nanotube bundles. *Carbon* **38**, 2017 (2000).
- [84] J. Yu, J. Ahn, S.F. Yoon, Q. Zhang, Rusli, *et al.* Semiconducting boron carbonitride nanostructures: Nanotubes and nanofibers. *Appl. Phys. Lett.* **77**, 1949 (2000).
- [85] Ph. Redlich, J. Loeffler, P.M. Ajayan, J. Bill, F. Aldinger, M. Rühle. B-C-N nanotubes and boron doping of carbon nanotubes. *Chem. Phys. Lett.* **260**, 465 (1996).
- [86] M. Terrones, A.M. Benito, C. Manteca-Diego, W.K. Hsu, O.I. Osman, J. P. Hare *et al.* Pyrolytically grown B<sub>x</sub>C<sub>y</sub>N<sub>z</sub> nanomaterials: nanofibres and nanotubes. *Chem. Phys. Lett.* **257**, 576 (1996).
- [87] W-Q. Han, J. Cumings, X. Huang, K. Bradley, A. Zettl. Synthesis of aligned B<sub>x</sub>C<sub>y</sub>N<sub>z</sub> nanotubes by a substitution-reaction route. *Chem. Phys. Lett.* **346**, 368 (2001).
- [88] E. Borowiak-Palen, T. Pichler, G.G. Fuentes, A. Graff, R.J. Kalenczuk, M. Knupfer, J. Fink. Efficient production of B-substituted single-wall carbon nanotubes. *Chem. Phys. Lett.* **378**, 516 (2003).
- [89] R. Arenal de la Concha, L. Wirtz, J-Y. Mevellec, S. Lefrant, A. Loiseau, A. Rubio. Infrared and Raman spectroscopy of single-walled BN-nanotubes. (2003) (available online).
- [90] C.F. Chen, C.L. Tsai, C.L. Lin. The characterization of boron-doped carbon nanotube arrays. *Diamond and Related Materials* **12**, 1500 (2003).
- [91] W.K. Hsu, S. Firth, P. Redlich, M. Terrones, H. Terrones, Y.Q. Zhu, *et al.* Boron-doping effects in carbon nanotubes. *J. Mater. Chem.* **10**, 1425 (2000).
- [92] C.Y. Zhi, J.D. Guo, X.D. Bai, E.G. Wang. Adjustable boron carbonitride nanotubes. *J. Appl. Phys.* **91**, 5325 (2002).
- [93] J. Yu, X.D. Bai, J. Ahn, S.F. Yoon, E.G. Wang. Highly oriented rich boron B-C-N nanotubes by bias-assisted hot filament chemical vapor deposition. *Chem. Phys. Lett.* **323**, 529 (2000).
- [94] C.Y. Zhi, X.D. Bai, E.G. Wang. Raman characterization of boron carbonitride nanotubes. *Appl. Phys. Lett.* **80**, 3590 (2002).
- [95] J. Maultzsch, S. Reich, C. Thomsen, S. Webster, R. Czerw, *et al.* Raman characterization of boron-doped multiwalled carbon nanotubes. *Appl. Phys. Lett.* **81**, 2647(2002).

- [96] U. Dettlaff-Weglikowska, J-M. Benoit, P-W. Chiu, R. Graupner, S. Lebedkin, S. Roth. Chemical functionalization of single walled carbon nanotubes. *Current Appl. Phys.* **2**, 497 (2002).
- [97] D. Golberg, Y. Bando, K. Kurashima, T. Sato. MoO<sub>3</sub>-promoted synthesis of multi-walled BN nanotubes from C nanotube templates. *Chem. Phys. Lett.* **323**, 185 (2000).
- [98] D. Golberg, Y. Bando, W. Han, K. Kurashima, T. Sato. Single-walled B-doped carbon, B/N-doped carbon and BN nanotubes synthesized from single-walled carbon nanotubes through a substitution reaction. *Chem. Phys. Lett.* **308**, 337 (1999).
- [99] F. Tuinstra, and J.L. Koenig. Raman spectrum of graphite. *J. Chem. Phys.* **53**, 1126 (1970).
- [100] M. Hirscher, M. Becher, M. Haluska, U. Dettlaff-Weglikowska, A. Quintel, *et al.* Hydrogen storage in sonicated carbon materials. *Appl. Phys. A: Mater. Sci. Process.* **72**, 129 (2001).
- [101] L. Zhang, H. Li, K.-T. Yue, S.-L. Zhang, X. Wu, *et al.* Effects of intense laser irradiation on Raman intensity features of carbon nanotubes. *Phys. Rev. B*, **65**, 073401 (2002).
- [102] R. G. Lacerda, A. S. Teh, M.H. Yang, K.B.K. Teo, N. L. Rupesinghe, *et al.* Growth of high-quality single-wall carbon nanotubes without amorphous carbon formation. *Appl. Phys. Lett.* **84**, 269 (2004).
- [103] J. Maultzsch. Vibrational properties of carbon nanotubes and graphite. *Ph.D. Thesis*, Berlin (2004) (available online).
- [104] C.Y. Zhi, X.D. Bai, and E.G. Wang. Resonance Raman scattering of boron carbonitride nanotubes. *Appl. Phys. Lett.* **84**, 1549 (2004).
- [105] C.Y. Zhi, X.D. Bai, and E.G. Wang. Boron Carbonitride Nanotubes. *J. Nanoscience and Nanotechnology* **4**, 35 (2004).
- [106] C. Fantini, A. Jorio, M. Souza, L.O. Ladeira, A.G. Souza Filho. One-dimensional character of combination modes in the resonance Raman scattering of carbon nanotubes. *Phys. Rev. Lett.* **93**, 087401 (2004).
- [107] M.F. Lin. Optical spectra of single-wall carbon nanotube bundles. *Phys. Rev. B* **62**, 13153 (2000).
- [108] J.W. Ding, X.H. Yan, and J.X. Cao. Analytical relation of band gaps to both chirality and diameter of single-wall carbon nanotubes. *Phys. Rev. B* **66**, 073401 (2002).
- [109] Bart Van Zeghbroeck. Principles of Semiconductor Devices. *Colorado University* (2004) (<http://ece-www.colorado.edu/~bart/book/>); and D. A. B. Miller, Semiconductor Optoelectronics Devices. *Stanford University*, (2000).
- [110] Program for nonlinear fitting of analytical functions (free download: <http://www.unipress.waw.pl/fityk/>).